

DEVELOPMENT AND IMPLEMENTATION OF AN UNDERWATER  
SYSTEM FOR INTERFACE WAVE MEASUREMENTS

---

A Thesis Presented to the Faculty of the Graduate School  
University of Missouri – Columbia

---

In Partial Fulfillment  
Of the Requirements for the Degree

Masters of Science  
Civil & Environmental Engineering

---

By  
MATTHEW M. HOLLRAH

Dr. Brent Rosenblad, Thesis Supervisor

DECEMBER 2005

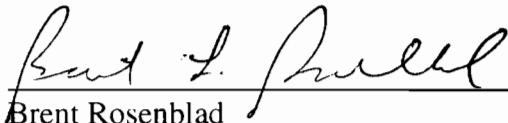
The undersigned, appointed by the Dean of the Graduate School, have examined the thesis entitled

**DEVELOPMENT AND IMPLEMENTATION OF AN UNDERWATER  
SYSTEM FOR INTERFACE WAVE MEASUREMENTS**

Presented by Matthew M Hollrah

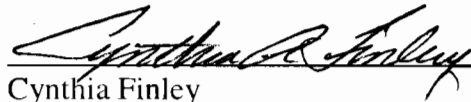
A candidate for the degree of Master of Science in Civil Engineering

and hereby certify that in their opinion it is worthy of acceptance.



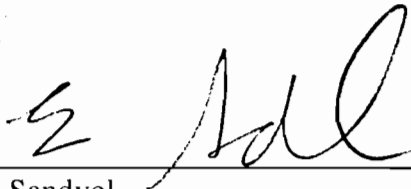
Brent Rosenblad

Department of Civil and Environmental Engineering



Cynthia Finley

Department of Civil and Environmental Engineering



Eric Sandvol

Department of Geological Sciences

## **ACKNOWLEDGEMENTS**

I would like to take this opportunity to thank my thesis advisor, Dr. Brent Rosenblad for his guidance throughout my masters program. I would also like to thank Dr. John Bowders and Dr. Erik Loehr for their guidance through my undergraduate career as well as their dedication to quality research and instruction at the University of Missouri – Columbia. I would also like to thank my fellow graduate students, especially Andy Boeckmann, John Deeken, and Katy Chandler for their thoughtful criticism, thoughtless use of their time, and constructive interference. Finally, I would like to thank Dr. Cynthia Finley and Dr. Eric Sandvol for their time in sitting on this committee. This work has been supported through a research grant from the University of Missouri Research Board.

# Development and Implementation of an Underwater System for Interface Wave Measurements

Matt Hollrah

Dr. Brent Rosenblad, Thesis Supervisor

## ABSTRACT

Measuring shear wave velocity profiles has become integral to geotechnical site investigation both on land and offshore. Obtaining accurate near-surface profiles in soft marine sediments can be expensive and time consuming using conventional intrusive methods. This work includes the development and field testing of an underwater source capable of generating surface wave energy for the determination of shear wave velocity profiles with resolution in the top foot to depths up to 20 feet.

A portable and remotely fired underwater impact source was developed. Dispersion curves generated using conventional surface wave methods and instrumentation for shallow testing on land were compared to those obtained using the source. Additionally, underwater measurements using both contacting and non-contacting receivers were performed. Underwater measurements showed that Scholte waves could be generated wavelength range of interest. Non-contacting interface wave measurements were compared to contacting measurements and show promising results with a need for further investigation.

## List of Tables

### Table

3.1 Part numbers associated with major source components.....	39
3.2 Components and weights of reaction mass.....	57
3.3 Final weights of all components .....	68
3.4 Estimated surface area, contact pressure, and undrained strength required not fail for several different embedment depths .....	69
3.5 Lengths and weights of frame sections.....	77

## List of Figures

### Figure

2.1 Generalized variation in shear modulus with shearing strain (from Rosenblad, 2000) .....	7
2.2 Relationship between the monotonic loading curve in shear and shear moduli of a geotechnical material (from Rosenblad, 2000) .....	8
2.3 Typical crosshole testing arrangement (from ASTM D4428, 1991) .....	10
2.4 Typical test arrangement and idealized observation scheme for crosshole tomographic seismic survey (from Kearey et al. 2002).....	11
2.5 Typical arrangement for downhole testing (a) and (b) seismic cone penetration testing (SCPT) (from Rosenblad, 2000) .....	12
2.6 Typical testing arrangement for suspension logging (from Nigbor and Imai, 1994).....	14
2.7 Refraction test showing ray paths and intercept times for a three-layered system (from Sharma, 1997).....	15
2.8 Normalized vertical and horizontal particle motions for a Rayleigh-type surface wave (from Richart et al., 1970) .....	17
2.9 Wave generated from a symmetric circular footing on a homogeneous elastic half- space (from Woods, 1968).....	18
2.10 Rayleigh wave velocity as a function of Poisson's Ratio (from Bedford and Drumheller, 1994) .....	19
2.11 Relationship between Poisson's ratio and velocities of wave propagation for compression (P), shear (S), and Rayleigh (R) waves (from Richart, 1962) .....	20
2.12 Typical SASW testing arrangement showing forward and reverse impacts.....	22
2.13 Receiver arrangement showing common mid-point array for SASW testing .....	23
2.14 Wrapped phase plot generated from a receiver spacing of 25 feet.....	25
2.15 Dispersion curve corresponding to the phase plot shown in Figure 2.14 .....	26
2.16 Composite dispersion curve generated from six receiver spacings .....	26

2.17 Shear wave velocity profile determined from the dispersion curve shown in Figure 2.16.....	28
3.1 Preliminary "mock-up" testing frame .....	36
3.2 Bench testing circuit used in preliminary testing.....	37
3.3 Exploded view of the source.....	38
3.4 Shop drawing of solenoid ( <i>from</i> Trombetta Inc.) .....	40
3.5 Construction drawings of the impact mass .....	42
3.6 Isometric view of impact mass .....	43
3.7 Construction drawings of the sleeve .....	45
3.8 Construction Drawings of the mounting plate.....	46
3.9 Construction drawings of the guide rods .....	48
3.10 Spring force per spring as a function of length for the return springs .....	49
3.11 Construction drawings of cell wall .....	51
3.12 Construction drawing of top cap.....	53
3.13 Isometric view of the inside and outside of the top cap.....	53
3.14 Construction drawing of bottom cap.....	55
3.15 Isometric view of the inside and outside of the bottom cap .....	56
3.16 Exploded isometric view of reaction mass components.....	58
3.17 Construction drawings of reaction mass plate .....	58
3.18 Circuit diagram for source power and control .....	61
3.19 Photograph of assembled surface component circuit.....	62
3.20 Surface component junction box mounted to the underside of battery box lid .....	63
3.21 Finished battery box.....	63

3.22 Exploded isometric view of power circuit .....	65
3.23 Photograph of finished power circuit .....	65
3.24 Construction drawings for the power circuit board .....	66
3.25 Photograph of cord ends and sockets.....	67
3.26 Geospace LP 4.5 Hz geophone and marsh case assembly .....	72
3.27 Assembled geophone ready for field use .....	72
3.28 Intermediate step in geophone podding .....	74
3.29 Finished de-molded potted geophone .....	74
3.30 Time record recorded from potted geophone and spiked geophone from same impact .....	75
3.31 Geophone mounted in frame with hardware.....	78
3.32 Field data acquisition system using the Signal Calc Card .....	80
4.1 Photograph of Geotechnical Research Facility at Midway.....	82
4.2 Comparison between recorded motion from the instrumented hammer and source showing pre-impact motion.....	84
4.3 Comparison of time records showing pre-impact motion before and after assembly hole relocation. ....	85
4.4 Comparison of time records showing second hit before and after spring buffer installation. ....	86
4.5 Spring and foam core assembly installed on top cap.....	87
4.6 Normalized time records collected at 30 receiver locations from an impact of the hammer source .....	90
4.7 Normalized time records collected at 30 receiver locations from an impact of the solenoid source .....	91
4.8 Time record comparison for solenoid and hammer sources at 5 ft from the source location. ....	92

4.9 Time record comparison for solenoid and hammer sources at 10 ft from the source location.....	92
4.10 Time record comparison for solenoid and hammer sources at 20 ft from the source location.....	93
4.11 Time record comparison for solenoid and hammer sources at 30 ft from the source location.....	93
4.12 Power spectra comparison for solenoid source and hammer source for 5 ft spacing.....	95
4.13 Power spectra comparison for solenoid source and hammer source for 10 ft spacing.....	95
4.14 Power spectra comparison for solenoid source and hammer source for 20 ft spacing.....	96
4.15 Power spectra comparison for solenoid source and hammer source for 30 ft spacing.....	96
4.16 Comparison of phase plots generated from different sources at five receiver pair locations of (a)4ft-8ft, (b)8ft-16ft, (c)16ft-32ft, and (d)25ft-50ft.....	98
4.17 Comparison of experimental dispersion curves for the (a) solenoid source and (b) sledge hammer.....	100
4.18 Profile from drilling performed at the Geotechnical Research Facility at Midway on April 20, 2005.....	101
4.19 Comparison of frequency-wave number contour plots generated from multi-channel analysis of surface waves for the (a) instrumented hammer and (b) solenoid source.....	103
4.20 Modes Identified from f-k plots shown in Figure 4.19.....	104
5.1 Photograph of pond at Bradford Farms Research Facility.....	106
5.2 Offset time records collected with the solenoid source and underwater geophones.....	108
5.3 Wrapped phase plots measured from SASW testing performed with the solenoid source and geophones.....	110

5.4 Dispersion curve generated from underwater SASW testing with the solenoid source and geophones .....	111
5.5 Frequency-wave number plot for underwater data collected with the source and geophones .....	112
5.6 Dispersion modes calculated from the f-k plot shown in Figure 5.5 .....	112
5.7 Offset time records collected with the solenoid source and suspended hydrophones.....	114
5.8 Time record comparison fro geophone and suspended hydrophone using the solenoid source at a 30 foot spacing .....	115
5.9 Frequency response comparison between surface wave measurements collected with the geophones and hydorphones.....	116
5.10 Dispersion curve comparing the geophone and hydrophone at a 12 ft spacing.....	117
5.11 Example of cosine taper window applied to the hydrophone time records .....	118
5.12 Frequency-wave number map for underwater data collected with the solenoid source and non-contacting hydrophone receivers.....	119
5.13 Comparison of dispersion modes calculated from data measured with geophone receivers and data measured with non-contacting hydrophone receivers .....	119

## Table of Contents

ACKNOWLEDGEMENTS .....	ii
ABSTRACT .....	iii
LIST OF TABLES .....	iv
LIST OF FIGURES .....	v
TABLE OF CONTENTS .....	x
<b>CHAPTER 1. INTRODUCTION</b>	
1.1 Overview .....	1
1.2 Objective .....	2
1.3 Scope of Project.....	2
1.4 Thesis Organization.....	3
<b>CHAPTER 2. CONVENTIONAL METHODS FOR SHEAR WAVE VELOCITY MEASUREMENT</b>	
2.1 Introduction.....	4
2.2 Conventional Methods for Measuring Vs.....	5
2.2.1 Body Wave Propagation .....	5
2.2.1.1 Body Wave Propagation in Elastic Materials.....	5
2.2.1.2 Body Wave Propagation in Soil.....	6
2.2.2 Crosshole Testing .....	9
2.2.3 Downhole Testing .....	11
2.2.4 Suspension Logging.....	13
2.2.5 Refraction Survey.....	14
2.3 Surface Wave Testing.....	16
2.3.1 Rayleigh Wave Dispersion.....	16
2.3.2 Spectral-Analysis-of-Surface-Waves (SASW) .....	21
2.3.2.1 Data Collection.....	21
2.3.2.2 SASW Data Processing.....	23
2.3.2.3 SASW Forward Modeling.....	27
2.3.3 Multi-Channel Surface Waves Method .....	28
2.4 Interface Wave Testing Underwater .....	29
2.4.1 Underwater Interface Wave Propagation .....	29
2.4.2 SASW Data Collection Underwater.....	30

**CHAPTER 3. UNDERWATER SYSTEM DEVELOPMENT**

**3.1 Introduction.....32**

**3.2 System Description and Requirements .....32**

**3.3 Source Development .....33**

**3.3.1 Characteristics of Impact Sources .....33**

**3.3.2 Design Considerations.....34**

**3.3.3 Source Concept.....35**

**3.3.4 Mechanical Design.....37**

        3.3.4.1 *Solenoid* ..... 39

        3.3.4.2 *Impact Mass*..... 40

        3.3.4.3 *Other Internal Components* ..... 43

        3.3.4.4 *Containment Cell*..... 50

        3.3.4.5 *Reaction Mass*..... 56

**3.3.5 Power System Design ..... 60**

        3.3.5.1 *Surface Components* ..... 61

        3.3.5.2 *Seafloor Components*..... 63

        3.3.5.3 *Cabling and Connections* ..... 66

**3.3.6 Geotechnical Design Issues ..... 67**

        3.3.6.1 *Bearing Pressure* ..... 67

        3.3.6.2 *Effect of Footing Size on Wavelengths Generated*..... 70

**3.4 Receiving Instrumentation .....70**

**3.4.1 Geophones.....70**

**3.4.2 Hydrophones.....76**

**3.4.3 Deployment Frame.....76**

**3.5 Data Acquisition.....78**

**3.5.1 Data Physics.....79**

**3.5.2 Hewlett Packard System .....80**

<b>CHAPTER 4. ON-LAND TESTING</b>	
<b>4.1 Introduction</b> .....	<b>81</b>
<b>4.2 On-Land Testing Procedure</b> .....	<b>81</b>
4.2.1 Location.....	81
4.2.1 Instrumentation Used .....	82
4.2.3 Field Testing Procedure.....	82
<b>4.3 Preliminary Testing of Source On-Land</b> .....	<b>83</b>
4.3.1 Results from Preliminary Testing.....	83
<b>4.4 Data Comparison</b> .....	<b>88</b>
4.4.1 Time Record Comparison.....	88
4.4.2 Frequency Spectra.....	94
<b>4.5 Comparison of Processed Data</b> .....	<b>97</b>
4.5.1 SASW Processing .....	97
4.5.2 Multi-Channel Processing .....	102
<b>4.6 Summary</b> .....	<b>104</b>
<b>CHAPTER 5. UNDERWATER TESTING</b>	
<b>5.1 Introduction</b> .....	<b>105</b>
<b>5.2 Underwater Testing Procedure</b> .....	<b>105</b>
5.2.1 Location.....	105
5.2.2 Instrumentation Used .....	106
5.2.3 Field Testing Procedure.....	106
<b>5.3 Underwater Testing with Contacting Receivers</b> .....	<b>107</b>
5.3.1 Time Record Comparison.....	107
5.3.2 SASW Processed Data .....	109
5.3.3 Multi-channel Processed Data.....	111
<b>5.4 Underwater Testing with Non-Contacting Receivers</b> .....	<b>113</b>
5.4.1 Time Record Comparison.....	113
5.4.2 SASW Processed Data .....	115
5.4.3 Multi-channel Processed Data.....	117
<b>5.5 Summary</b> .....	<b>120</b>
<b>CHAPTER 6. SUMMARY, CONCLUSIONS, RECOMMENDATIONS</b> .....	<b>121</b>
<b>APPENDIX A. TROUBLESHOOTING AND USER’S MANUAL</b> .....	<b>124</b>
<b>REFERENCES</b> .....	<b>137</b>

## CHAPTER 1. INTRODUCTION

### 1.1 Overview

The measurements of shear wave velocity ( $V_s$ ) profiles has become an important component of geotechnical site investigations for many dynamic as well as conventional static applications. Shear wave velocity profiles obtained from a variety of field measurements can provide valuable soil stiffness information for use in applications such as earthquake site response analysis, soil liquefaction evaluation, waste material characterization, and ground improvement evaluations. The cost associated with measuring shear wave velocity profiles from intrusive methods, such as crosshole and downhole tests, can be very high. This is especially true if profiles are required over a large area. In recent years, non-intrusive surface wave methods have been developed and applied to generate  $V_s$  profiles more efficiently and at reduced cost.

Generating  $V_s$  profiles at underwater sites can also be very expensive and problematic using traditional intrusive methods. Soft, near-surface marine sediments in particular are difficult to evaluate using traditional testing methods. It has been shown that underwater interface wave (termed Scholte waves) measurements can be used effectively to determine  $V_s$  profiles for underwater geotechnical applications. (Luke et al., 1994, Rosenblad, 2000) Many underwater applications require information in the near surface (top 1 to 20 feet) of sediments. Development of an easily deployed, non-intrusive system for shallow sediment characterization could aid in such applications.

## **1.2 Objective**

The objectives of this research are to design, construct, and evaluate a prototype system for shallow  $V_s$  profiling of underwater geotechnical sites using interface waves. The proposed system consists of a source and multiple receivers capable of being remotely deployed underwater for collecting interface wave information in near-surface marine sediments. The goal is to develop a system that will serve as a practical field tool for shallow  $V_s$  profiling, as well as a development platform and research tool for further enhancements of data collection and processing methods of underwater interface wave data.

## **1.3 Scope of Project**

The scope of this project is to design, construct, and evaluate an underwater system for measuring shallow interface wave profiles at underwater sites. The system should be capable of measuring  $V_s$  profiles in the top 15 to 20 feet of underwater sediments. In addition, the system is required to be hand-deployable, remotely-activated, and capable of use in submerged conditions. The system should produce comparable results to on-land tests using standard testing procedures. In addition, the system will be used underwater to evaluate the potential of using non-contacting transducers for data collection. Future research will be conducted utilizing this equipment for improving data collection and processing methods at underwater sites. The testing system will consist of a hand deployed mounting frame, a source capable of exciting energy with the necessary frequency content for shallow marine sediment investigations, and receivers capable of recording marine sediment motions. Data

will be processed using common methodologies used on for land processing (SASW: Spectral Analysis of Surface Waves, and multi-channel waveform transformation methods).

## **1.4 Thesis Organization**

This thesis is organized into 6 chapters. Chapter 2 covers background information on in-situ stress wave velocity measurements and common surface wave testing methodologies used for on-land applications. It also briefly discusses differences associated with using interface waves for underwater testing. Chapter 3 details the system construction including the receivers, source, frame, and data acquisition used for all aspects of field testing. Chapter 4 discusses data obtained from terrestrial field testing and compares the underwater system to traditional surface wave testing methodologies. Chapter 5 presents data obtained from underwater testing of the system using both contacting and non-contacting receivers to measure interface waves. Lastly, Chapter 6 contains conclusions drawn from the data obtained with the testing system.

## CHAPTER 2. CONVENTIONAL METHODS FOR SHEAR WAVE VELOCITY MEASUREMENT

### 2.1 Introduction

Most traditional geotechnical problems are analyzed as limit equilibrium problems that require soil strength parameters. This class of problems involves calculating the capacity of soil under a certain set of loading conditions and designing such that a failure condition is not reached. Examples of this type of analysis include slope stability calculations and bearing capacity calculations.

Many other geotechnical problems require deformation-based analyses. In these cases a limit equilibrium failure condition may never be reached, instead excessive deformation may constitute failure. Dynamic problems such as earthquake site response and foundation vibrations are examples of deformation-based analyses. In addition, a variety of static problems involving soil-structure interaction require deformation parameters. The shear modulus,  $G$ , is related to the shear wave velocity of the material using:

$$G = \rho V_s^2 \quad (2.1)$$

where  $G$  is the shear modulus of the material,  $\rho$  is the bulk density of the material, and  $V_s$  is the shear wave velocity. Therefore, field measurements of  $V_s$ , along with estimates of soil density, provide a means to calculate the small-strain shear modulus. In addition, shear wave velocity is primarily influenced by the void ratio,  $e$ , of the soil and the mean

effective confining pressure in the soil. Because of these relationships,  $V_s$  measurements can provide a useful indication of changes in fundamental soil properties.

In this chapter several conventional methods for determining  $V_s$  profiles will be discussed. Also, surface wave theory and state of practice testing methods using surface waves for geotechnical site characterization will be discussed. Lastly, interface wave propagation underwater will be covered.

## **2.2 Conventional Methods for Measuring $V_s$**

Several geophysical methods are commonly used today to evaluate  $V_s$  profiles at geotechnical sites. While some of the conventional testing methods are non-intrusive, most require on-site drilling. These methods are similar in that they all propagate and receive body (compression and shear) waves to measure the velocity of the material in its existing location. A brief overview of body waves in elastic materials and soils is presented, followed by a description of commonly applied methods.

### **2.2.1 Body Wave Propagation**

#### ***2.2.1.1 Body Wave Propagation in Elastic Materials***

Body waves are stress waves that propagate in any elastic medium. There are two types of body waves that can propagate in a solid, compression or primary waves (P) and shear or secondary waves (S). In a compression wave, the particle motion is in the same direction as the wave propagation and has a faster arrival time than the shear wave. The particle motion associated with the compression wave is known as irrotational motion. Because the compression wave causes a volume change of the material at the wave front,

it is also referred to as a dilational wave. The compression wave velocity is related to the physical properties of a homogeneous, isotropic, elastic material by:

$$V_p = \sqrt{\frac{\lambda + 2G}{\rho}} = \sqrt{\frac{E(1-\nu)}{\rho(1+\nu)(1-2\nu)}} \quad (2.2)$$

where  $V_p$  is the wave velocity of the compression wave (P),  $E$  is Young's Modulus,  $G$  is the shear modulus,  $\lambda$  is Lambe's constant,  $\nu$  is Poisson's ratio, and  $\rho$  is the mass density.

The second type of body wave, the shear wave (S), has particle motion transverse to the direction of wave propagation. In this case, the motion is equivolumetrical, meaning there is no volume change in the material due to the wave propagation. This is also known as a distortional wave. The wave velocity of a shear wave is also related to the material properties by:

$$V_s = \sqrt{\frac{G}{\rho}} \quad (2.3)$$

Wave velocities for the body waves can be related by combining Equations 2.2 and 2.3. The ratio of the compression wave velocity to the shear wave velocity is a function of Poisson's ratio as shown in Equation 2.4.

$$\frac{V_p}{V_s} = \sqrt{\frac{2(1-\nu)}{1-2\nu}} \quad (2.4)$$

### ***2.2.1.2 Body Wave Propagation in Soil***

Body waves are used in soil and rock applications to determine the small-strain stiffness properties of the in-situ material, as shown is Equation 2.3. In-situ soils have a fairly narrow band of possible unit weights, making it possible to reasonably estimate the small strain stiffness by assuming a total unit weight of the material. Soil body wave

testing is typically done in the elastic, small strain, regime of less than 0.001% strain. The small strain modulus, often termed  $G_{max}$ , of the material is at its maximum value and linear in this small strain range, as shown in Figure 2.1. The stress-strain behavior of soil at strains beyond the elastic regime is non-linear, with the shear modulus decreasing with increasing strain, as shown in Figure 2.2.

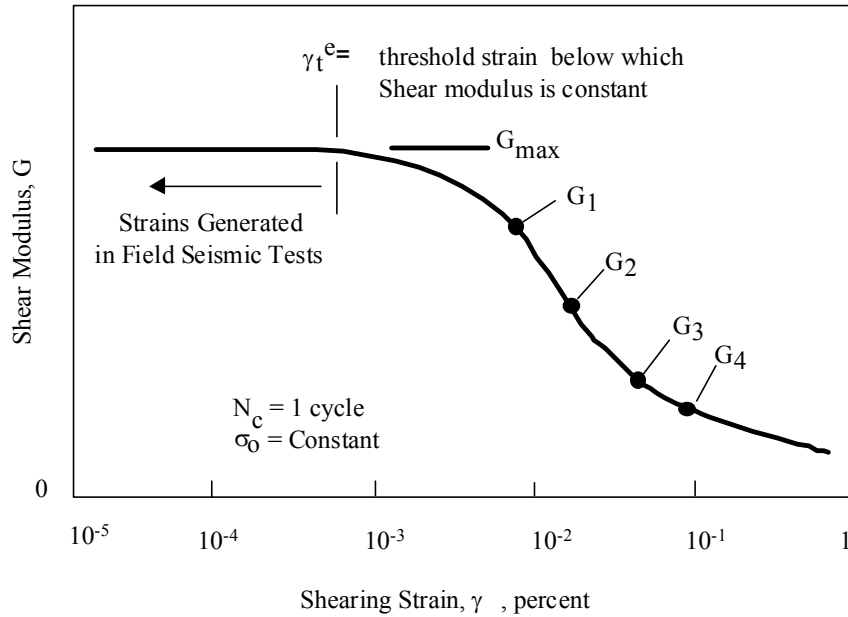


**Figure 2.1** Generalized variation in shear modulus with shearing strain (*from Rosenblad, 2000*).

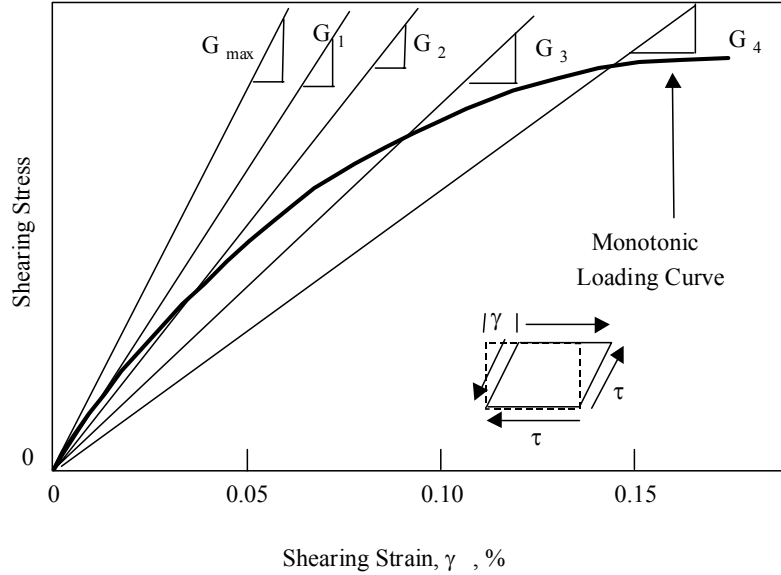


**Figure 2.2 Relationship between the monotonic loading curve in shear and shear moduli of a geotechnical material (from Rosenblad, 2000).**

Several parameters have been found to influence the small strain stiffness of a soil. These parameters include: void ratio, effective mean principle stress, overconsolidation ratio, soil type, soil plasticity, excitation frequency, and time of confinement (Stokoe et al., 1999). The in situ void ratio and the mean effective confining stress have the most influence of the terms mentioned. An empirical relationship developed to predict the maximum shear modulus for soils from basic soil parameters is shown in Equation 2.5 (Hardin, 1978).

$$G_{\max} = \frac{A}{F(e)} OCR^k P_a^{(1-n)} \sigma_o'^n \quad (2.5)$$

Where:

$A$  = dimensionless stiffness coefficient,

$\sigma_o'$  = mean effective stress,

$F(e)$  = void ratio function,

$OCR$  = overconsolidation ratio,

$k$  = exponent dependent on plasticity index,

$P_a$  = atmospheric pressure (100 kPa), and

$n$  = exponent related to isotropic stress state.

### **2.2.2 Crosshole Testing**

Crosshole tests are performed in an array of two or more cased boreholes. Borehole spacings are recommended to be 3 meters (10 ft) but can be as much as 4.5 meters (15 ft) (ASTM, 1991). Velocity transducers (geophones) are typically used as the receivers for soil applications. Crosshole testing uses an active impact source coupled with the casing in one of the holes. The receivers are coupled, typically at the same depth as the source, in another cased hole. Typically, receivers are mounted in three orthogonal directions to detect the compression (P) wave, the vertically polarized shear (SV) wave, and the horizontally polarized shear (SH) wave. The arrival time of the compression and shear wave measured between the boreholes can be used to calculate shear or compression wave phase velocity of the soil. Information about in-situ material anisotropy can also be determined from the horizontally and vertically polarized shear wave arrivals (Stokoe et al, 1991). The basic testing arrangement is shown in Figure 2.3.

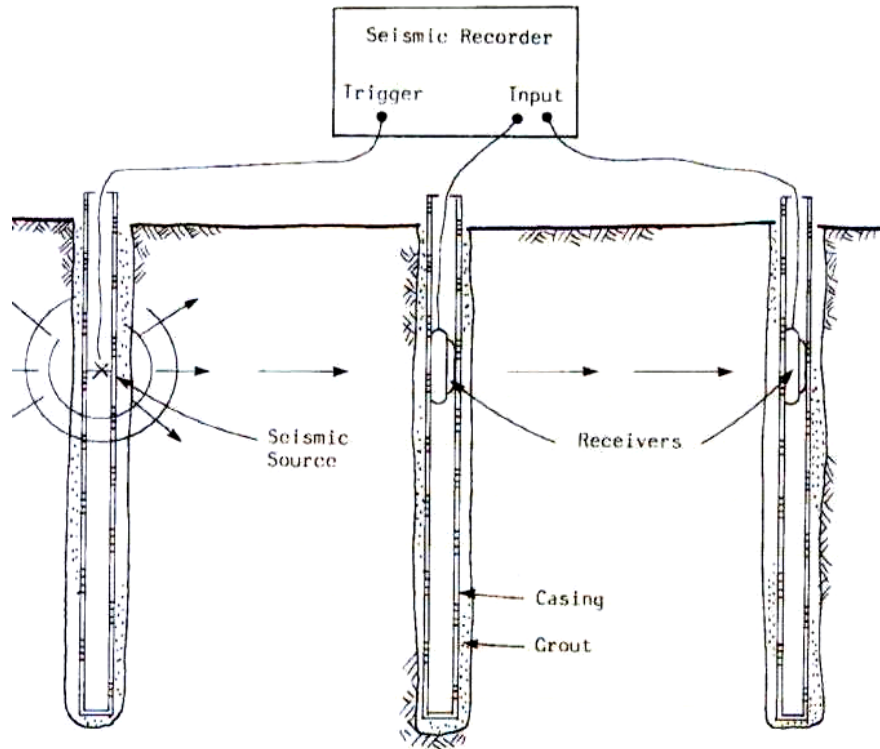


**Figure 2.3** Typical crosshole testing arrangement (*from ASTM D4428, 1991*).

Crosshole testing is a widely accepted means of  $V_s$  profiling. It is the only geophysical  $V_s$  profiling technique with an ASTM standard at this time. Crosshole tests provide good resolution at any depth by using short propagation distances. Crosshole testing is expensive to perform due to the number of holes and casing requirement for all holes and the need to determine hole inclination with depth to accurately calculate velocity.

Recently crosshole tomography (CST) has been gaining interest for geotechnical applications. This method of crosshole testing achieves a more detailed 2-dimensional interpretation of anomalies in the material between the boreholes. The tests are performed by measuring multiple source receiver paths as shown in Figure 2.4. A tomographic

inversion procedure is performed to detect anomalous velocity regions in the test material (Kearey et al., 2002).

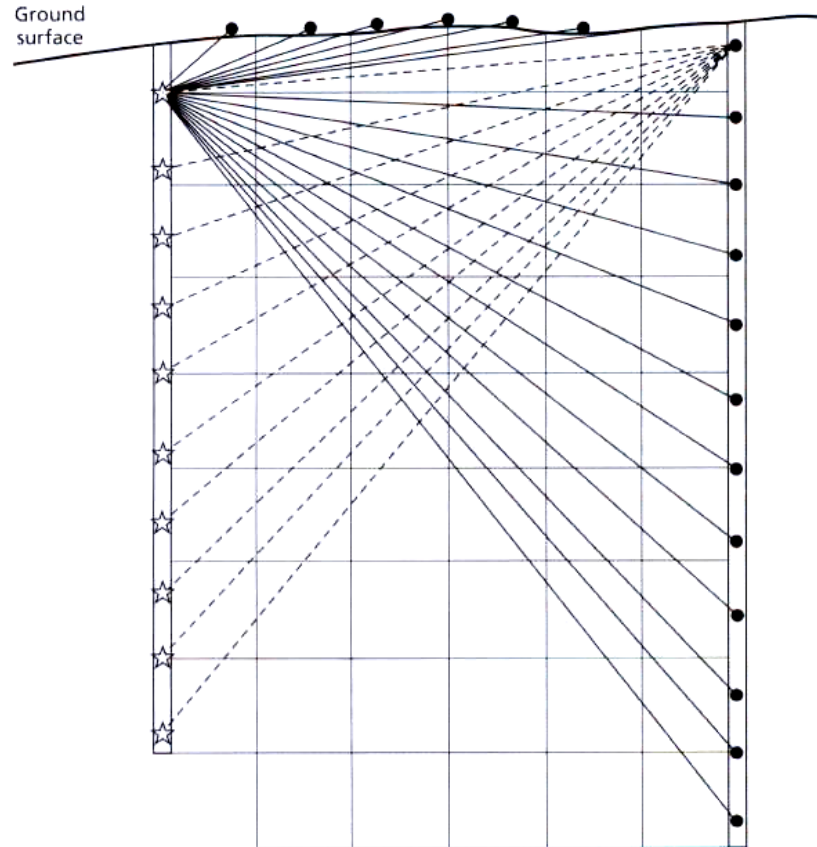


**Figure 2.4** Typical test arrangement and idealized observation scheme for crosshole tomographic seismic survey (*from Kearey et al., 2002*).

### 2.2.3 Downhole Testing

Downhole testing is performed using one cased borehole. A receiver is lowered into this borehole and coupled with the casing at the depth of interest to measure interval or pseudo-static arrivals of the compression and shear waves. This procedure is repeated at several depths to profile the site. Straight ray paths are typically assumed for data processing. Impact sources at the surface generate compression waves and horizontally

polarized shear (SH) waves. Typically these sources are coupled to the ground with a large normal force. Figure 2.5a shows a typical downhole testing arrangement.

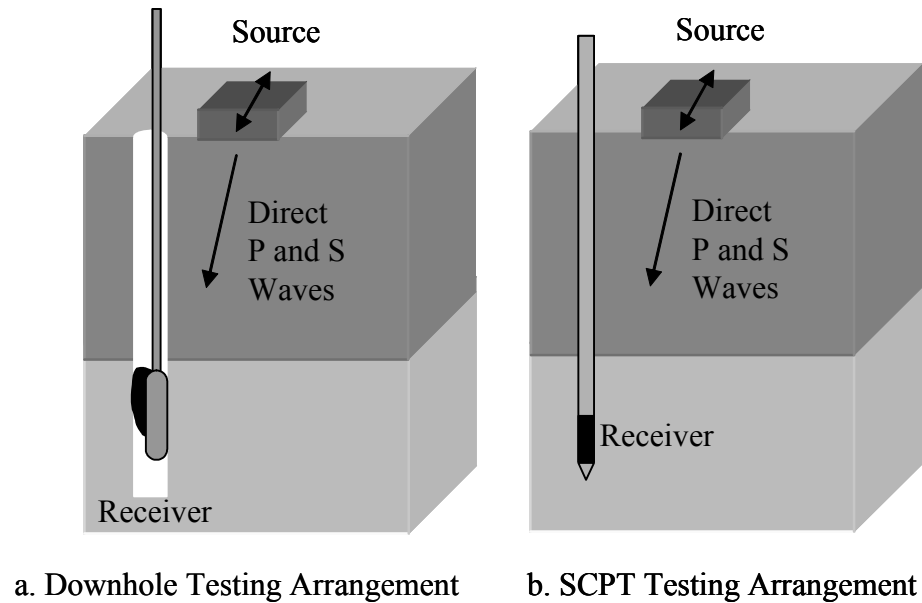


**Figure 2.5** Typical arrangement for downhole testing (a) and (b) seismic cone penetration testing (SCPT) (from Rosenblad, 2000).

Downhole testing is a less expensive alternative to crosshole tests. Because travel times increase with depth in a downhole test there are fewer issues with non-perpendicular boreholes. Depth of effective downhole testing is often limited by source coupling at the surface. At a site with high impedance contrasts between strata, the straight ray path assumption can lead to inaccurate estimation of the shear wave velocity.

The seismic cone penetrometer test (SCPT) is a more cost effective way to gather downhole data. A test similar to that of the downhole test is performed on a site by pushing an instrumented cone outfitted with seismic receivers into the ground, as shown in Figure 2.5b. This allows downhole data to be collected without the need to drill a

borehole test. In addition, traditional cone penetrometer data is collected (Campanella et al., 1984). The SCPT is limited by the inability to penetrate stiffer layers..

#### **2.2.4 Suspension Logging**

Suspension logging is another method for measuring  $V_s$  and  $V_p$  which requires only a single borehole (Kitsunezaki, 1980). Unlike the downhole test, the source is carried on the instrument string. The instrument string is suspended by a wire and consists of two receivers separated by a damping material and a horizontally polarized source separated from the receivers at some known distance. Suspension logging requires a slurry or water filled hole to couple the energy between the receivers. In suspension logging material near the hole is primarily sampled, therefore, soil disturbance around the borehole can affect the measurement quality. A typical testing arrangement for suspension logging is shown in Figure 2.6.

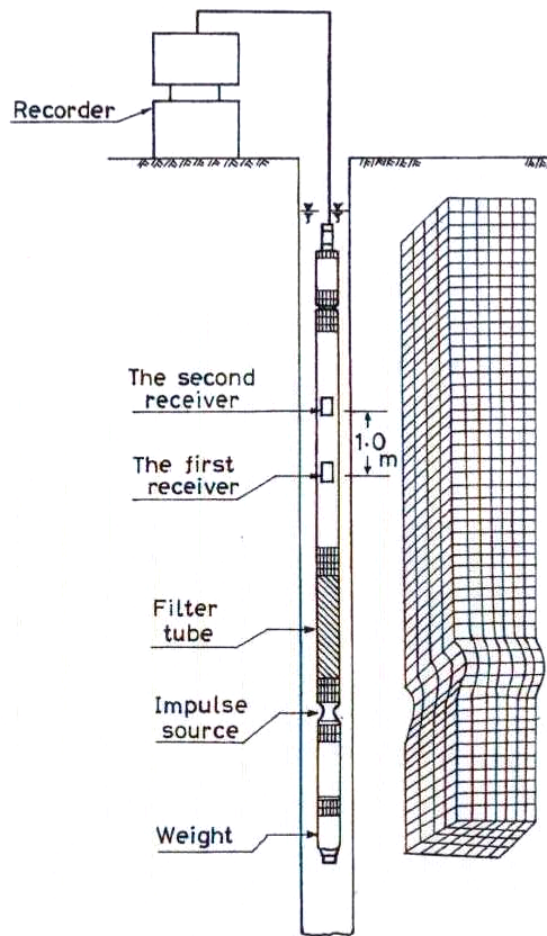


**Figure 2.6** Typical testing arrangement for suspension logging (from Nigbor and Imai, 1994).

Suspension logging can go to great depths using the slurry or fluid filled hole. The wire deployment method reduces the weight of the testing apparatus at depth. Maintaining a fluid filled borehole can be problematic if rock fissures or other highly permeable layers are encountered at the site.

### **2.2.5 Refraction Survey**

Refraction surveys are performed using a vertically or horizontally polarized source and an array of geophones (Richart et al, 1970, Sharma, 1997). The velocity and

depth of subsurface layers are determined from the slope and intercepts of a plot of arrival time versus receiver location. At receiver locations near the source, the first arrival is the direct wave. If a higher velocity layer is encountered by the body waves at depth, a critically refracted wave will travel along the interface between the layers and generate a head wave in the upper layer. At larger offsets from the source, the refracted wave will arrive before the direct wave resulting in a change in slope of the arrival time versus receiver offset plot, as shown in Figure 2.7.

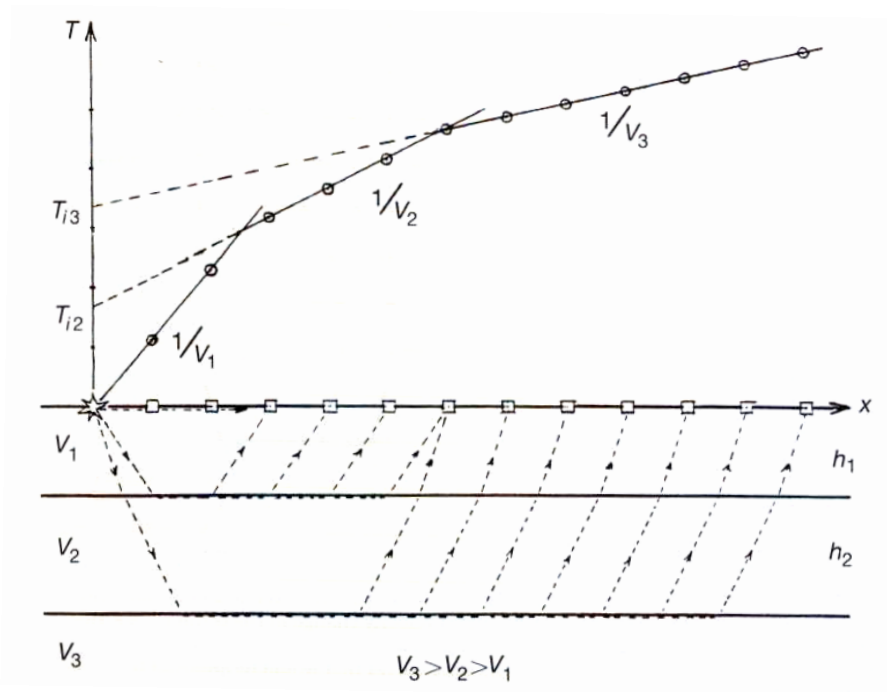


**Figure 2.7** Refraction test showing ray paths and intercept times for a three-layered system (from Sharma, 1997).

For most geotechnical engineering applications, shear wave velocity profiles are of primary interest. Although refraction surveys can be performed with sources generating horizontally polarized shear waves, detection of wave arrivals is more problematic due to the compression wave arriving first. In addition, refraction surveys

can not be used when inversions (stiff-over-soft) conditions exist. This is a common situation in near surface geotechnical work which limits the applicability of refraction surveys in geotechnical practice.

## **2.3 Surface Wave Testing**

In the past 20 years, methods based on surface wave propagation have been developed to non-intrusively measure  $V_S$  profiles at geotechnical sites. A brief overview of surface wave propagation in elastic materials is presented followed by a description of the two most common surface wave methodologies used for geotechnical applications.

### **2.3.1 Rayleigh Wave Dispersion**

A disturbance on the surface of an elastic half-space will produce both body wave propagation into the half-space as well as surface wave propagation along the solid/air interface. This surface wave, which results from the interaction of SV and P waves with the stress-free interface, is termed a Rayleigh wave. There are several attributes of Rayleigh waves that are substantially different than body waves.

Rayleigh wave particle motions at a single frequency decrease with depth such that most of the particle motions occur at depths less than approximately one wavelength below the surface. Therefore, changing the frequency of the input energy changes the effective depth of sampling below the surface. Lower frequency energy, for example, penetrates and samples deeper below the surface than higher frequency energy. Particle motion associated with a Rayleigh-type surface wave is a retrograde elliptical motion at the surface, containing both vertical and horizontal motions. The normalized wave

amplitudes of the vertical and horizontal particle motions with respect to Poisson's ratio can be seen in Figure 2.8.

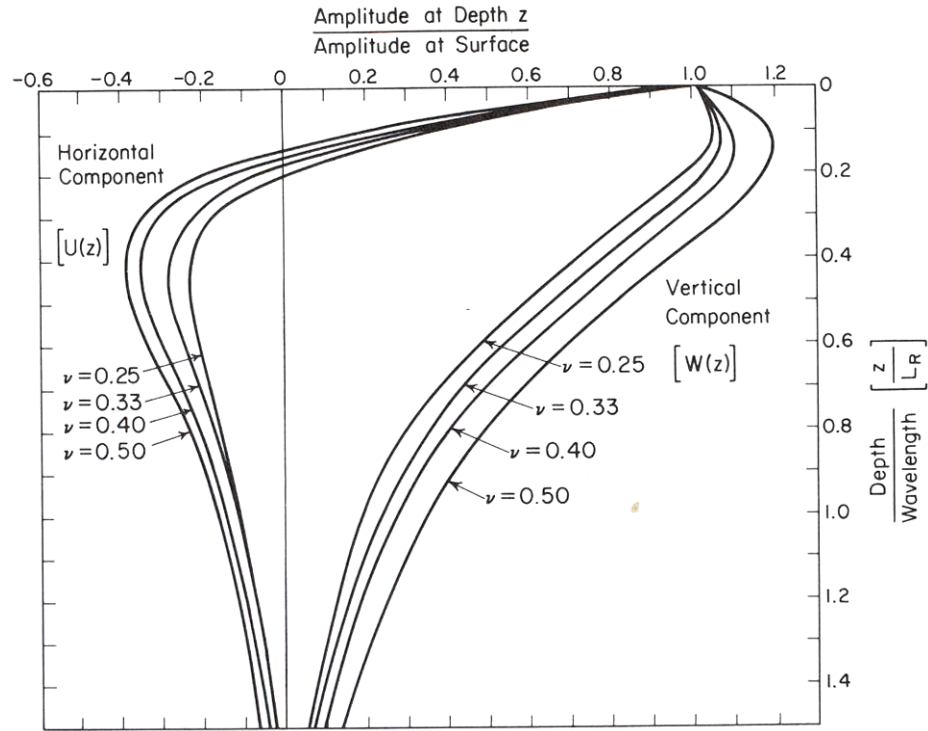


**Figure 2.8** Normalized vertical and horizontal particle motions for a Rayleigh-type surface wave (from Richart et al., 1970).

The percentage of energy from an impact converted to Rayleigh-type surface waves is 67%, compared to 26% for a shear waves, and 7% in a compression waves (Miller et al., 1955). In addition, surface wave amplitudes decrease in proportion to  $\frac{1}{\sqrt{r}}$ , where  $r$  is the radius from the energy source, compared to  $\frac{1}{r^2}$  for body waves. Due to the higher energy and lower geometric damping, surface wave motions are generally the dominate motion measured at the surface away from the source.

The energy in Rayleigh-type surface waves propagates cylindrically from a circular source as shown in Figure 2.9 (Richart et al., 1970). The figure compares the

hemispherical propagation of a shear or compression wave in the same half space with the cylindrically propagating Rayleigh wave.

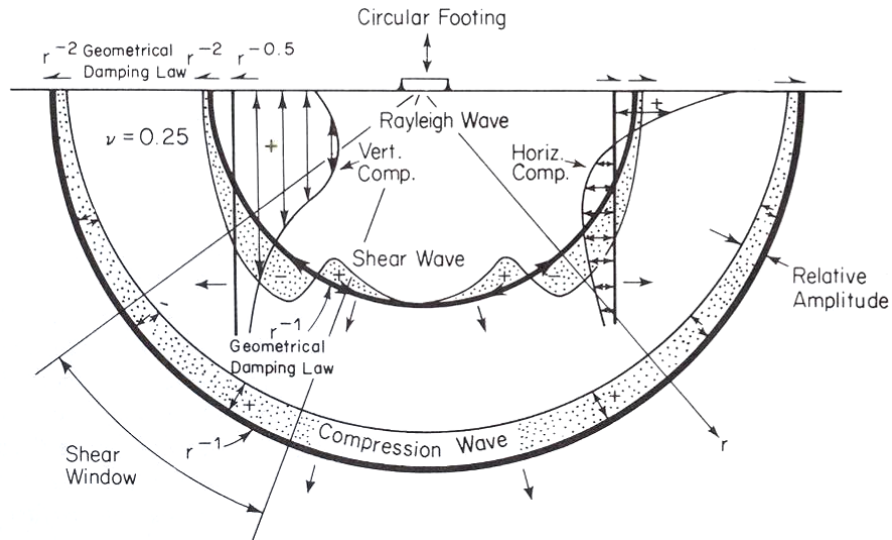


**Figure 2.9** Wave generated from a symmetric circular footing on a homogeneous elastic half-space (from Woods, 1968).

Lastly, the relationship between  $V_S$  and Rayleigh wave velocity ( $V_R$ ) in a uniform halfspace is solely a function of Poisson's ratio (Achenbach, 1973). This relationship is:

$$V_R = \frac{0.86 + 1.14\nu}{1 + \nu} V_S \quad (2.6)$$

where  $V_R$  is the Rayleigh wave velocity,  $V_S$  is the shear wave velocity, and  $\nu$  is Poisson's ratio of the material. As per Equation 2.6, the Rayleigh wave velocity is always less than the shear wave velocity. In a homogeneous halfspace the ratio of the Rayleigh wave velocity to the shear wave velocity can be plotted as a function of Poisson's ratio. This ratio can range from 0.88 to 0.96 for Poisson's ratios of 0 to 0.5, respectively, as shown in Figure 2.10.

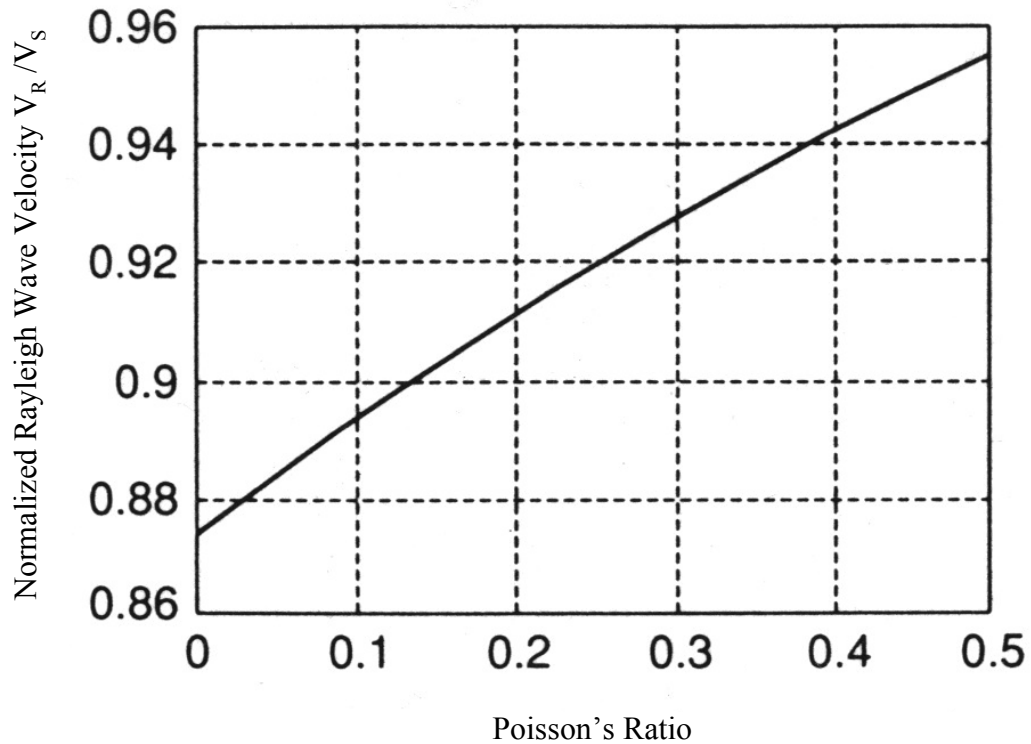


**Figure 2.10** Rayleigh wave velocity as a function of Poisson's Ratio (*from Bedford and Drumheller, 1994*).

Surface wave measurements are made in the small strain range (typically less than 0.001% strain) where the soil behavior is essentially elastic. Therefore the relationship between the compression wave ( $V_P$ ) and Rayleigh wave velocity can be calculated by using the elastic relationship for body waves discussed previously and shown again in Equation 2.7.

$$\frac{V_P}{V_S} = \sqrt{\frac{2(1+\nu)}{1-2\nu}} \quad (2.7)$$

By substituting for the shear wave velocity from Equation 2.6 into Equation 2.7 the relationship between Rayleigh and compression wave velocities can be determined. This

relationship can be found in Equation 2.8. The relationship of the different wave velocities as a function of Poisson's ratio is shown in Figure 2.11 for a continuous semi-infinite elastic medium. The values of material density ( $\rho$ ) and small strain stiffness ( $G$ ) are constant for a uniform layer.

$$\frac{V_R}{V_P} \left( \frac{1 + \nu}{0.86 + 1.14\nu} \right) = \sqrt{\frac{1 - 2\nu}{2(1 - \nu)}} \quad (2.8)$$

Therefore, for a uniform, elastic halfspace, surface wave velocities are independent of frequency.

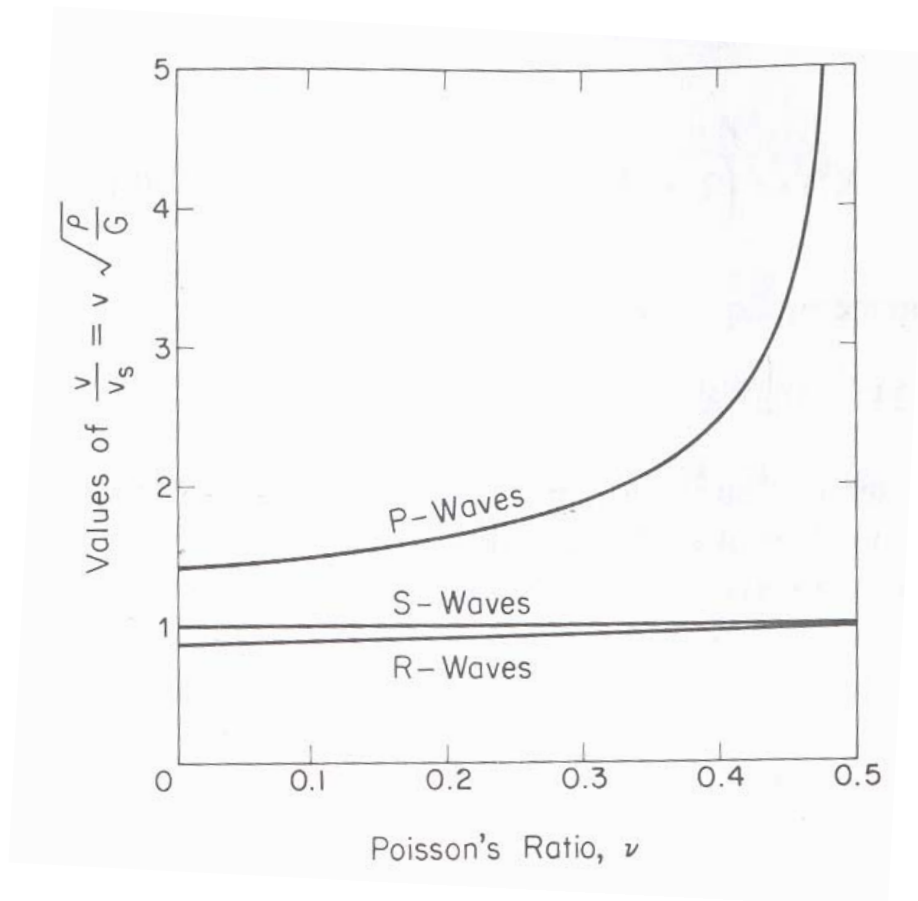


**Figure 2.11** Relationship between Poisson's ratio and velocities of wave propagation for compression (P), shear (S), and Rayleigh (R) waves (from Richart, 1962).

### **2.3.2 Spectral-Analysis-of-Surface-Waves (SASW)**

The SASW method is a common testing methodology used in geotechnical applications for surface wave testing on land (Stokoe et al. 1994). The three general steps in SASW testing are data collection, data processing, and forward modeling or inversion. These steps are described below.

#### ***2.3.2.1 Data Collection***

The standard SASW testing arrangement is shown in Figure 2.12. The test arrangement includes two or more vertical motion transducers, a vertically oriented excitation source, and a data acquisition system. Receivers are typically arranged using a common midpoint array as shown in Figure 2.13. The measurement process begins with closely spaced receivers and a high frequency source. The receiver spacing is then increased (typically doubled) and the measurement repeated with lower frequency energy. For each receiver spacing the source is maintained at a distance equal to the receiver spacing from the first receiver to allow the surface wave to be established and to minimize any near-field effects (Sanchez-Salinerio, 1987).

Sources used for surface wave excitation range in physical size from a small geology hammer to large Vibroseis trucks. For SASW testing, the source is vertically polarized and may be excited from transient, continuous, or random wave sources. Continuous steady-state waveform sources use a swept-sine method of energy generation where the source is excited at a single frequency for a short period of time before being changed to the next frequency. This method is often utilized for deep profiling where long-wavelength, low-frequency energy is required and input energy can be used to

generate a single frequency. In many cases, a random noise source such as large bulldozers are effective low-frequency sources. The source used for a particular receiver spacing at a particular location depends on the energy input required as well as the frequency content of interest. Typical sources include, but are not limited to, hammers, drop weights, explosives, construction machinery, and Vibroseis trucks. Recently a low-frequency source has been developed as part of the Network for Earthquake Engineering Simulation program (Stokoe et al, 2004).

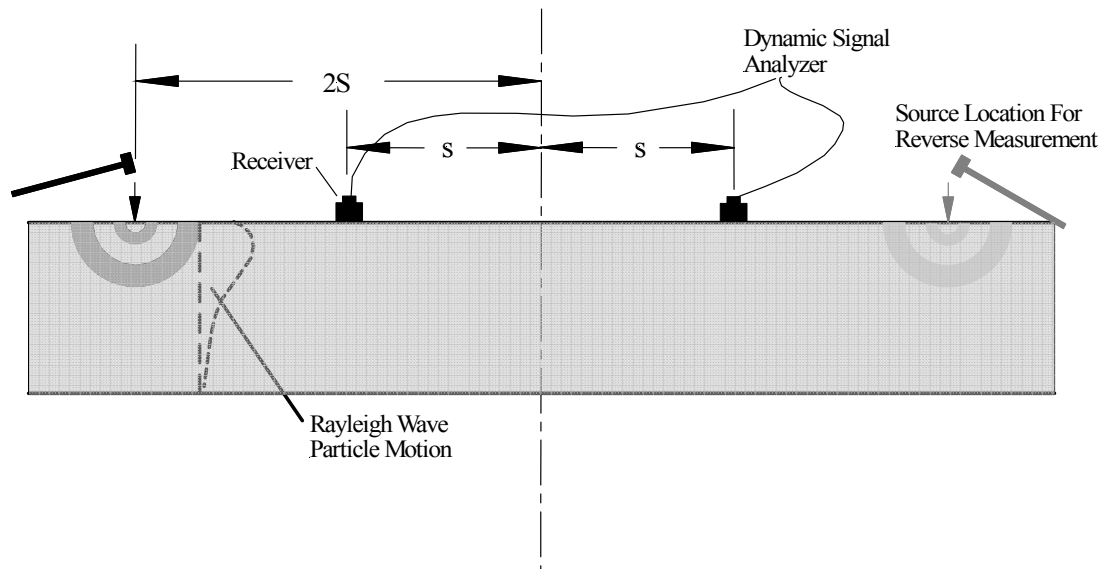


**Figure 2.12** Typical SASW testing arrangement showing forward and reverse impacts.

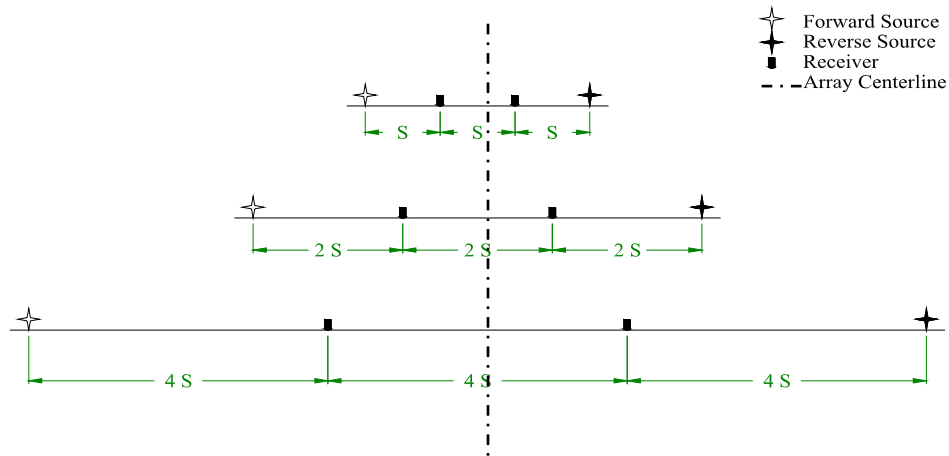


**Figure 2.13 Receiver arrangement showing common mid-point array for SASW testing.**

Typically, geophones are used as the vertical velocity transducers in surface wave testing. Surface wave measurements on soils are typically performed in the frequency range of tens to hundreds of Hertz. Geophones are selected such that their natural frequency is lower than the lowest frequency of interest. For deep profiling, 1-Hz seismometers are required.

### **2.3.2.2 SASW Data Processing**

The typical SASW experimental test arrangement discussed, shown in Figures 2.12 and 2.13, is used to collect time records at each geophone in the array. The source used for SASW testing is typically an active source. In the case of an impact source or drop weight, the source must be sized so that the frequency content of interest is generated, and the energy is above the noise level at the receiver locations of interest. Typically several sources are used at a single location to generate a broad range of frequencies.

Data collection can be performed with geophones or accelerometers depending on the frequency range of interest. In the case of rock and pavement testing accelerometers

are used with very high natural frequencies, while geophones with much lower natural frequencies are typically used for soil applications.

Time records are collected at each receiver spacing using a dynamic signal analyzer or a computer-based data acquisition interface. The frequency span (and therefore time window of the record) is changed for each receiver spacing to allow for the best resolution available over the range of frequencies of interest. Typically the range of frequencies of interest for each receiver spacing are those associated with wavelengths of  $1/3d$  to  $2d$ , where  $d$  is the receiver spacing. Often times the test can be performed in a reverse manner, as indicated in Figures 2.12 and 2.13, to cancel out phase shifts caused differences in receiver-to-ground coupling. Another practice used to improve data quality is the averaging of multiple impacts at the same receiver spacing in the frequency domain. Averaging allows background noise inherent to the site to be reduced to a manageable level.

Time records recorded are typically triggered on the first receiver (the receiver closest to the source). From the measured time records a wrapped phase plot is calculated from the cross power spectrum or frequency response. An example wrapped phase plot is shown in Figure 2.14.

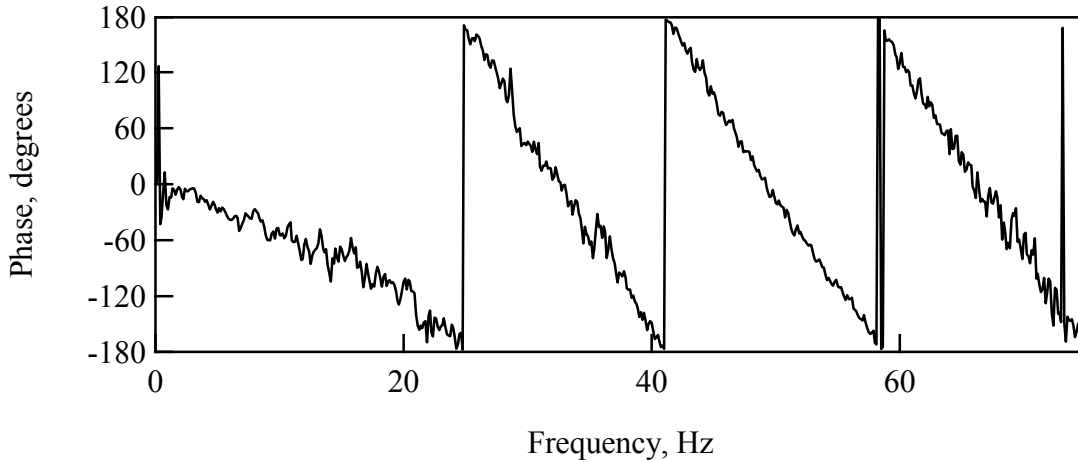


**Figure 2.14** Wrapped phase plot generated from a receiver spacing of 25 feet.

The wrapped phase plot is “unwrapped” and the phase information is used to calculate the “apparent” phase velocity using Equation 2.9. The term apparent phase velocity is used because the velocity does not necessarily correspond to a single mode, but instead is the velocity due to the superposition of body and surface wave modes,

$$V_R = f \cdot \left( \frac{360^\circ}{\Phi_{21}} \right) d \quad (2.9)$$

where  $V_R$  is the phase velocity of the Rayleigh wave,  $f$  is the frequency,  $d$  is the receiver spacing, and  $\Phi_{21}$  is the phase shift. Figure 2.15 shows the dispersion curve generated from a single receiver pair spaced 25 ft apart. This procedure is repeated for each receiver pair and a composite dispersion curve for the site generated from all receiver pairs is developed as shown in Figure 2.16.

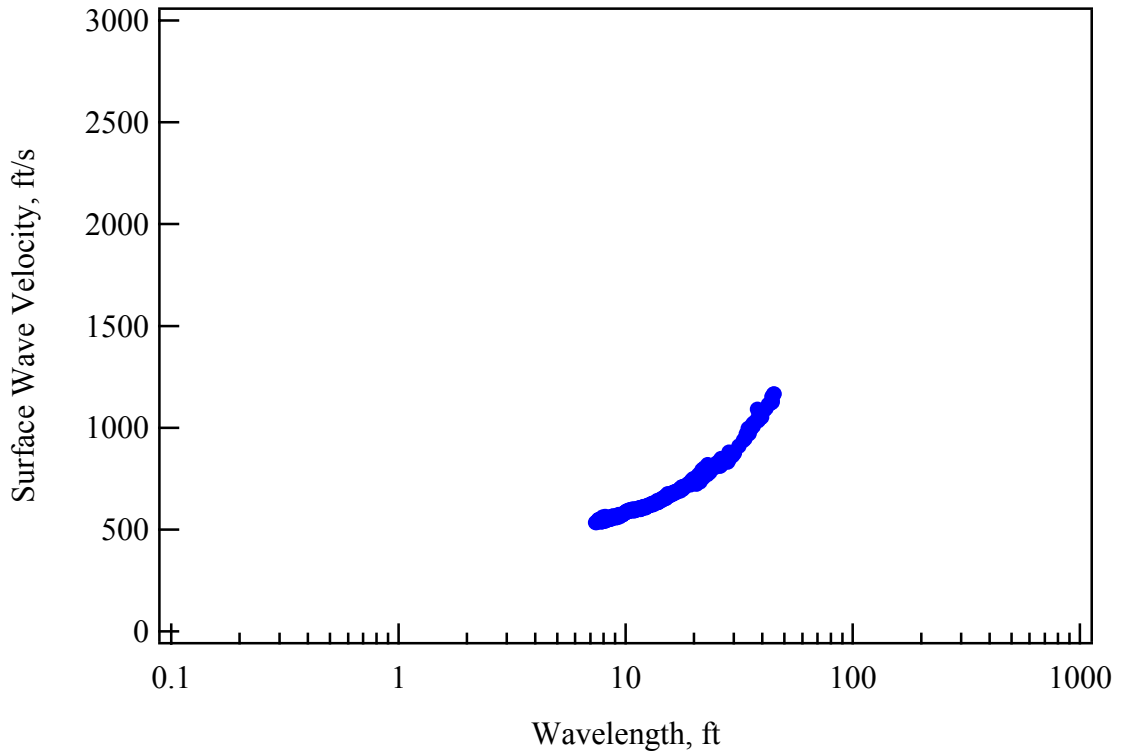


**Figure 2.15** Dispersion curve corresponding to the phase plot shown in Figure 2.14.

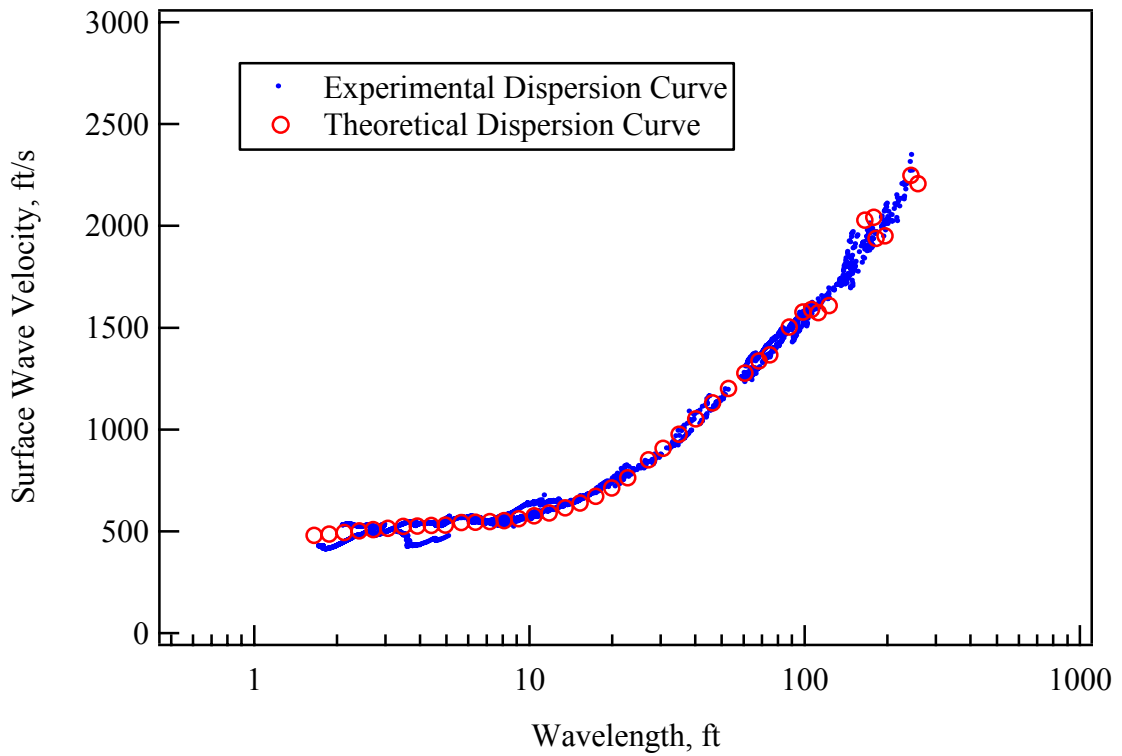


**Figure 2.16.** Composite dispersion curve generated from six receiver spacings.

### ***2.3.2.3 SASW Forward Modeling***

Interpretation of the measured composite dispersion curve involves a forward modeling or inversion procedure to obtain a theoretical dispersion curve fitting the measured curve. Figure 2.16 shows an example of the fit between the theoretical dispersion and a measured field curve. The shear wave velocity profile used to generate this fit is shown in Figure 2.17. The forward model typically used in SASW testing is based on the solution of surface displacements due to a transient disk load applied at the surface of the soil. The dynamic stiffness matrix approach that relates applied forces to displacements at the interfaces between layers is implemented in this solution (Kausel and Roesset, 1981; Kausel and Peek, 1982). This solution includes contributions from surface wave modes as well as body wave modes. A variety of different inversion techniques have been implemented to automate the solution of the shear wave velocity profile from a measured experimental dispersion curve.

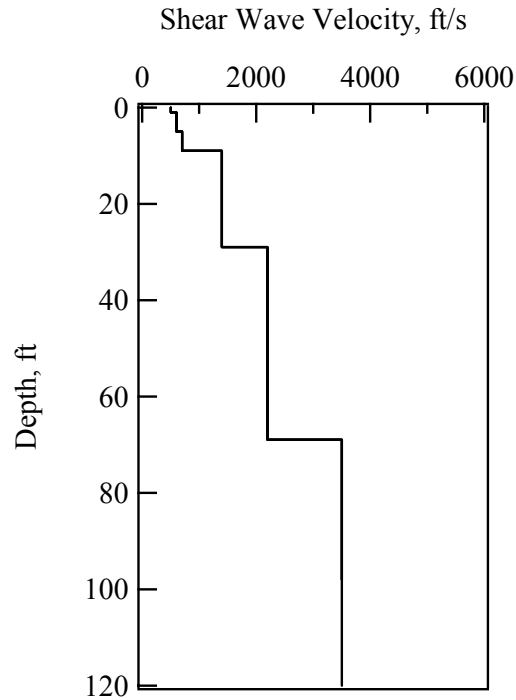


**Figure 2.17** Shear wave velocity profile determined from the dispersion curve shown in Figure 2.16.

### 2.3.3 Multi-Channel Surface Waves Methods

Multi-channel surface wave data collection and interpretation methods are also commonly used in geotechnical engineering applications. One example is the commonly used Multi-Channel-Analysis-of Surface-Waves (MASW) method (Park et al., 1999). In multi-channel approaches, time records are collected using 12 or more receivers at closely spaced intervals along the surface. Surface wave energy is excited in much the same manner as with SASW testing. The recorded time-space data is transformed into a different domain using a wavefield transformation method, such as the two-dimensional Fourier transform or the slant stack method (McMechan and Yedlin, 1981). The objective of this transformation is to separate the different surface wave propagation modes. The current state of the practice is to use the fundamental surface wave mode in

the forward modeling or inversion process. The theoretical solution is typically based on the transfer matrix method (Thomson, 1950; Haskell, 1953) to calculate the fundamental surface wave mode.

## **2.4 Interface Wave Testing Underwater**

Previously the surface wave associated with a boundary interface of an elastic semi rigid medium halfspace was discussed. In the terrestrial case, the interface consists of the medium in which the wave propagates and air. The Rayleigh wave model assumes a homogeneous, isotropic, elastic halfspace with a stress-free boundary condition. The Rayleigh wave model is not appropriate when considering surface waves traveling along a solid/water interface. Interface waves traveling on a solid/water interface are often referred to as Scholte waves.

### **2.4.1 Underwater Interface Wave Propagation**

Scholte wave propagation is more complex than Rayleigh wave propagation. As previously discussed, the ratio of Rayleigh wave velocity to shear wave velocity in a homogeneous halfspace is a function only of Poisson's ratio. In contrast, the ratio of Scholte wave velocity to shear wave velocity in a homogeneous halfspace changes due to additional factors. Several studies of the theoretical behavior of the Scholte wave have been performed for both a homogeneous and layered halfspace. (Sedighi Manesh, 1991; Lee, 1996) These studies have shown that there are several variables affecting Scholte wave propagation.

Theoretical analyses of Scholte wave propagation reveal that water depth, relative stiffness, and Poisson's ratio have a significant effect. As the wavelength of the Scholte

wave exceeds approximately 10 times the thickness of the water column the Scholte wave velocity approaches that of the Rayleigh wave. As the ratio of the wavelength to the thickness of the water column approaches zero the interface wave behaves more like a theoretical Scholte wave in a deep water condition. (Sedighi Manesh, 1991)

Relative stiffness of the marine sediments can have a significant effect on Scholte wave velocity. The only variable affecting Rayleigh wave velocity is the Poisson's ratio of the material. Therefore at a constant Poisson's ratio, the ratio of the Rayleigh wave and shear wave velocities is constant. The ratio of the Scholte wave and shear wave velocities at a constant Poisson's ratio is not constant but decreases with increasing stiffness of the medium of propagation (Sedighi Manesh, 1991).

Poisson's ratio does not affect the normalized Rayleigh wave velocity significantly over a range of possible Poisson's ratios for soil. The maximum possible change is approximately 6% from a Poisson's ratio of 0 to 0.5. In the case of the Scholte wave, Poisson's ratio has slightly more pronounced effect on the normalized interface wave velocity of approximately 8% over the same range.

In addition to the Scholte wave, underwater sources generate an Airy wave. This wave develops as a result of wave generation energy being coupled with the water and travels at the air/water interface. Airy wave velocities are much slower than the Scholte interface wave velocity.

#### **2.4.2 SASW Data Collection Underwater**

Collecting surface wave measurements underwater in soft marine sediments can be significantly more complex than similar tests performed on land. In the underwater

case the use of various sources generating a broad range of frequencies is problematic. Typically, for underwater surface wave testing impulsive sources such as air guns or explosives have been used (Park et al., 2000; Kaufmann et al., 2005; Rosenblad, 2000). One disadvantage of these sources is the large amount of energy that is radiated into the water column and the subsequent interference with the measurement of the underwater surface wave. This is especially a problem at receiver locations close to the source. For this reason, many studies using explosive sources have not provided good resolution of shear wave velocities ( $V_s$ ) in the near-surface sediments.

Additionally, deploying and coupling receivers is more difficult in the underwater environment. Typically, vertically gimballed geophones are utilized to assure vertical orientation. In addition, it is not practical to maintain a common midpoint array for SASW testing underwater as is done on land. Therefore, the receivers are typically deployed with a linear array and a stationary source location.

## **CHAPTER 3. UNDERWATER SYSTEM DEVELOPMENT**

### **3.1 Introduction**

The objective of this project is to develop an underwater system capable of measuring the shear wave velocity profile in the top 15 feet at underwater geotechnical sites. This platform will be used as a ground truth for future non-contacting underwater surface wave studies. A major component of this system is a remotely operated underwater source capable of generating sufficient surface wave energy.

This chapter documents equipment used and developed for collecting surface wave measurements underwater. The chapter discusses data acquisition equipment, instrumentation, and source development and construction. Construction and modification of several peripheral components is also discussed.

### **3.2 System Description and Requirements**

The underwater system consists of a source, receivers, deployment frame, and data acquisition system. Requirements for the source are that it is hand-deployable, remotely-operated, and capable of exciting wave energy to profile approximately 15 feet or more below the soil-water interface. Past experience on land has demonstrated the effectiveness of a 12-pound sledge hammer dropped from a height as low as 6-in. for profiling to depths of 15 feet at most sites. The source was, therefore, designed to produce a similar excitation in terms of amplitude and frequency content.

The requirements for the receiving instrumentation are that they are capable of recording small signals over the frequency range of interest (~10 to 300 Hz). The instrumentation must also be adapted to mount to a rigid frame intended to hold the

source and receiver array in a fixed location relative to the source. The frame must be rigid enough to hold the source and all instrumentation during deployment and extraction. The data acquisition system must be capable of recording small signals with acceptable amplitude and frequency resolution. The system components acquired or developed to meet these criteria are described below.

### **3.3 Source Development**

#### **3.3.1 Characteristics of Impact Sources**

An impact on an elastic half-space is a broad-band source of surface wave energy. An impact of infinitely small duration will produce an infinitely wide frequency band signal. As the duration of the impact increases, the band-width decreases with a reduction in higher-frequency energy. Past studies have analyzed and described the primary factors affecting the signal characteristics generated from an impact source (Roesset, 1994). The dimensions, mass, and drop height of the impact source are the primary factors affecting signal amplitude and frequency content. The surface wave amplitude will be primarily influenced by the velocity of the mass at the time of impact. For a free-fall source, therefore, the drop height is the factor controlling the velocity at impact. Increases in the drop height will result in larger signal amplitudes recorded at the ground surface.

The frequency content of the signal is inversely related to the impact duration. The mass of the impact source is the primary factor influencing the impact duration. A larger mass will produce longer impact duration and, hence, enhanced low-frequency

energy. High-frequency energy is generated from a short impact duration associated with a smaller mass.

In typical on-land surface wave studies a broad range of sources are used to resolve shear wave velocity values in the top few feet down to depths of several hundred feet (Stokoe et al., 1994). On land, it has been found that a single sledge hammer source, with a weight of 12 to 20 lbs, provides sufficient broad-band energy to generate shear wave velocity profiles in the depth range of 1 to 20 ft. At quiet sites, small drop heights of approximately 0.5 ft have been shown to generate sufficient energy to sample in this depth range. The underwater source developed for this system is designed to provide a similar performance to a typical sledge hammer with a low impact velocity.

### **3.3.2 Design Considerations**

Excitation of energy from an impact source on land is easily accomplished through an unassisted weight drop through the air or an accelerated mass impact such as swinging a sledge hammer. At underwater sites, simple impact excitation is complicated by several factors. First, as previously mentioned the mass used for the impact must be sized appropriately to generate the requisite frequency content. However, due to viscous losses, a free drop through the water will not produce a large impact velocity. Therefore, a pressure resistant and water-proof containment cell that will move with the impact is required. Secondly, if the mass is to be accelerated with an external force to achieve a larger impact velocity, it must be both powered and triggered remotely. Another important consideration is the need for a reaction against the applied force. Additionally, the source will remain in contact with the ground before and after the impact presenting

the potential for pre- and post-impact disturbances affecting the frequency content of the propagating wave. The generation of a “clean” impact from an underwater source is, therefore, more difficult than from a sledge hammer impact on land. Other issues of concern include the potential for bearing capacity failure in soft soil and the contrasting need for a small source footprint to generate short wavelength energy. These issues are discussed in the following sections as they related to the design of the source.

### **3.3.3 Source Concept**

Conceptually, the source consists of an impact mass accelerated by a remotely-fired solenoid in a watertight and pressure resistant containment cell. The solenoid-accelerated mass impacts the base of the containment cell. The movement of the containment cell against the soil generates the surface wave energy. The entire device is held in contact with the soil with a spring-coupled reaction mass. This conceptual plan was first implemented in preliminary “mock-up” testing and later in the final design.

Alternatives considered during conceptual design were pneumatic or hydraulic assisted drop weights, and explosive sources. These concepts were not pursued because of increased complexity, the need for supplementary support equipment, and environmental reasons. Additionally, noise in the water column generated from an explosive source was a concern for collecting short-range measurements.

Bench testing and preliminary field testing were performed to evaluate the conceptual design. The preliminary field testing was done to confirm conceptual ideas as well as determine the effect of changing several of the design parameters. Figure 3.1 shows the preliminary testing frame.

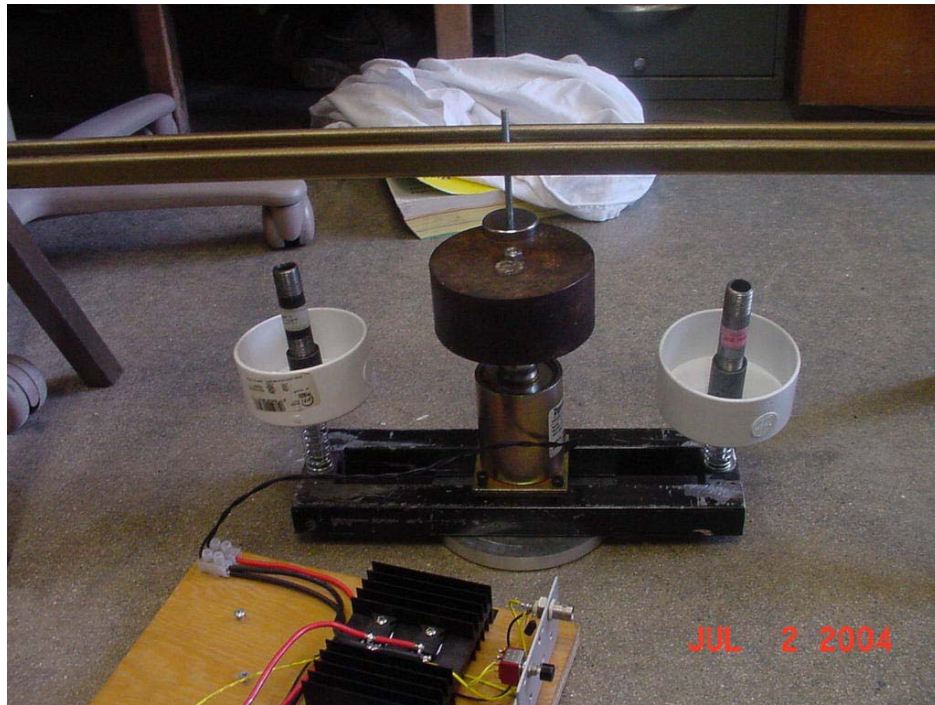


**Figure 3.1 Preliminary "mock-up" testing frame.**

The preliminary testing device consisted of a metal frame to which various sizes of metal contact plates could be attached. The solenoid could be directly attached to the metal plates. Two bolts were welded to the frame to act as guides for the simulated reaction mass. Short sections of pipe were later added to the PVC cups and filled with lead shot to evaluate the effect of different reaction masses. The solenoid plunger could be attached to several moving masses to evaluate impact generated by different masses. The plunger was held in the loaded position by a small frame and a magnet. The magnet was installed on a threaded rod to allow different stroke lengths to be evaluated. The mass of the frame could also be altered to simulate the mass of the containment cell and evaluate material options.

Preliminary tests were performed using the bench testing circuit shown in Figure 3.2. This circuit was used to evaluate the mechanical aspects of the source as well as

electronic improvements or alterations. Capacitor selection was a critical aspect of the electronic design and therefore several different capacitor banks were tested to determine the effectiveness and make a final selection.

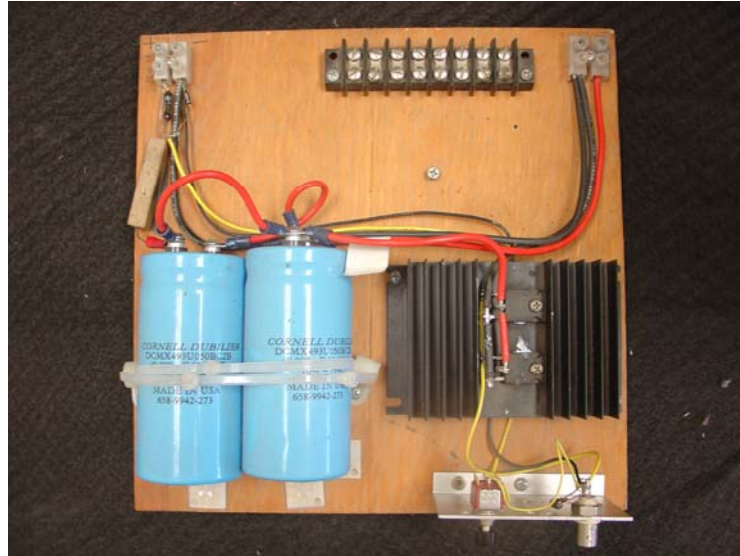


**Figure 3.2** Bench testing circuit used in preliminary testing.

Preliminary tests showed that the conceptual design was feasible and gave insight to the direction of the design of individual components. The specific mechanical and electrical design described below was carried out based on the preliminary testing.

### **3.3.4 Mechanical Design**

Mechanical design of the source was controlled by the factors discussed in Section 3.3.2. These factors as well as space constraints dominated the design of the impact source. Figure 3.3 shows an exploded view of the source including the containment cell. Part names are provided for each major component and are listed in Table 3.1. These part names and numbers will be used from this point forward with reference to a specific component. For detailed assembly, operation, and troubleshooting a user's manual for the impact source is provided in Appendix A.

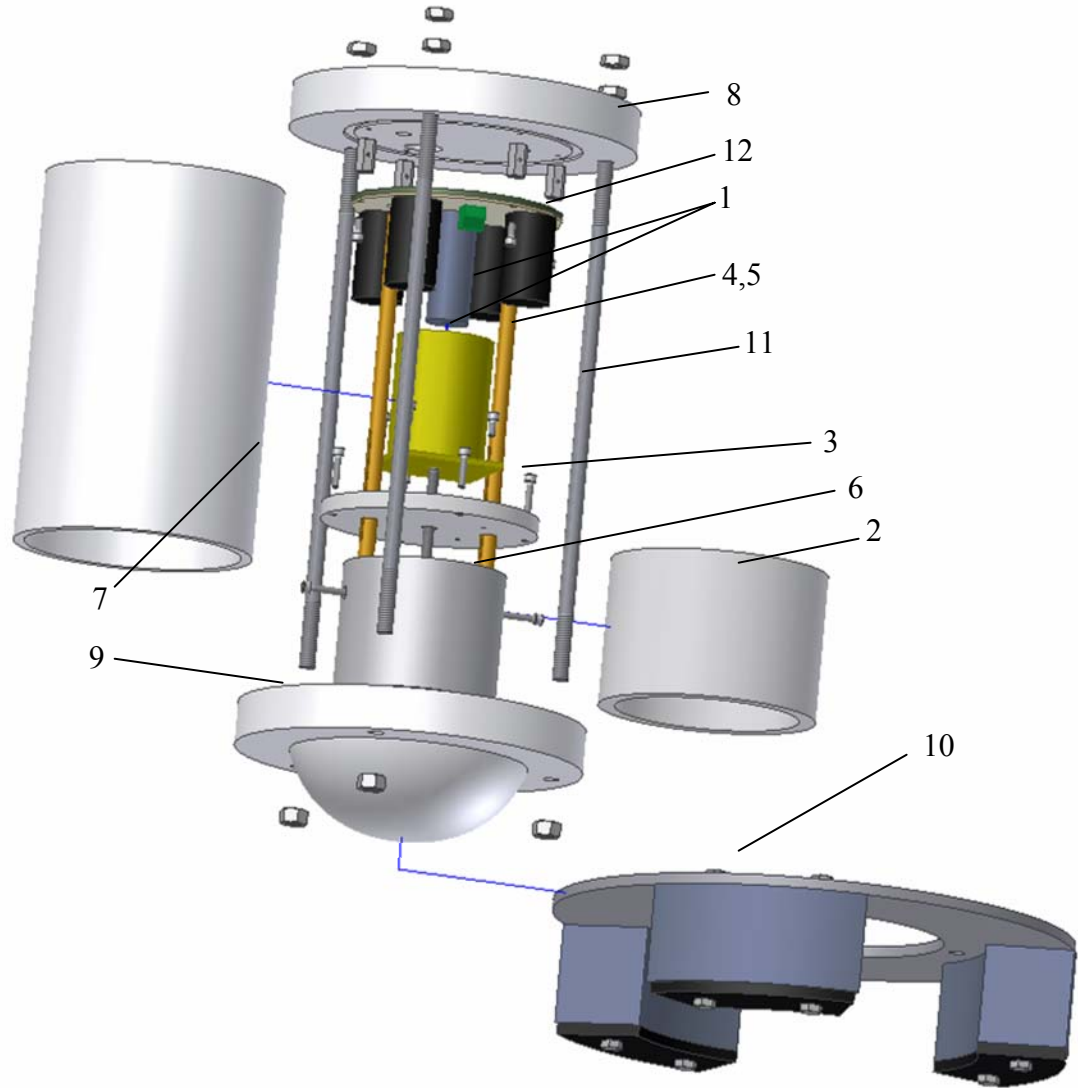


**Figure 3.3** Exploded view of the source.

**Table 3.1 Part numbers associated with major source components**

Part Number	Name
1	Solenoid (and Plunger)
2	Sleeve
3	Mounting Plate
4	Guide Rod
5	Return Spring
6	Moving Mass
7	Cell Wall
8	Top Cap
9	Bottom Cap
10	Reaction Mass
11	Clamp Rods

**3.3.4.1 Solenoid**

The role of the solenoid in the source design is to accelerate the impact mass to a higher velocity at the point of impact than could be achieved through free-fall alone. As the impact velocity (and hence kinetic energy) increases, the amplitude of surface waves recorded at the ground surface away from the source will also increase. The two factors influencing the impact velocity for a constant impact mass are the solenoid force and stroke length. Therefore, a commercially available solenoid was selected with the maximum force and stroke length within the power and space limitations of the source design.

The solenoid used is a Trombetta model Q514 pull type solenoid. Manufacturer's specifications list the solenoid as having up to a 1-1/2-in. in stroke and up to 50 pounds of pull down force. The model used is rated for 24 volt operation with a duty cycle of 20%. The plunger is a 2.9-in. long highly magnetic iron core with a 1/4-in. 20 UNC (Unified Course Thread) threaded hole used to connect the plunger to the moving object. The solenoid works by energizing a coil of wrapped wire to create an electric field in the core.

The field is concentrated in the core by the steel case and pulls the plunger toward the center of the magnetic field. The velocity of the plunger at impact is decreased as the stroke length is decreased. Maximizing the velocity of the mass at impact was a dominating design factor for this application and, therefore, the stroke length was maintained as long as possible. A shop drawing of the solenoid from Trombetta is shown in Figure 3.4.

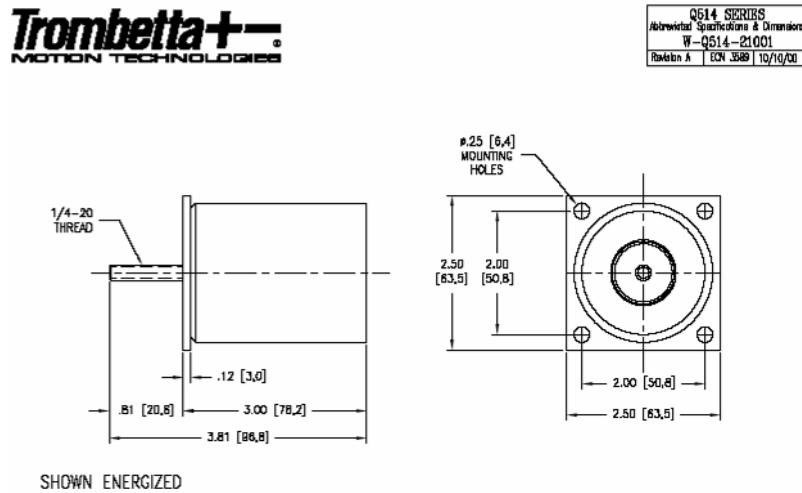


**Figure 3.4** Shop drawing of solenoid (from Trombetta Inc.)

### 3.3.4.2 Impact Mass

The duration of the impact between the source and soil will depend primarily on the stiffness of the soil and on the mass of the impact source. For a given soil site, a larger mass will produce a longer impact duration and hence generate relatively more low-frequency energy. The design objective was to use a single impact source to generate surface wave energy to resolve the shear wave velocity profile from 1 ft. to a depth of about 15 ft. or greater. In order to do this, the source must generate surface wave energy with wavelengths from approximately 2 to 30 feet in a variety of soil conditions. Based on the preliminary field testing and experiences from prior testing on

land, an impact mass with a weight of 10 pounds was chosen for the source. The dimensions of the impact mass were governed by the overall size of the containment cell and the stroke length of the solenoid.

To construct the mass a 3.75-in. diameter section of round steel stock was purchased from a local steel supplier. The section was cut to 3.00-in. in length and faced on both ends. Several holes were required in the moving mass. Holes for the guide rods were bored to match the assembly holes in the top cap, bottom cap, and mounting plate. The original holes in the moving mass were drilled as a free fit on 3/8-in., at 0.397 in. The holes were then reamed out on both ends of the piece to accept 3/8-in. inside diameter, 1/2-in. outside diameter oil impregnated bronze shaft bushings. The bushings were then pressed into the holes and reamed over the guide rod diameter by 0.005 in. The oil impregnated bushings used were 1/2-in. in length, decreasing the contact area between the mass and the guide rods and adding lubrication to the system.

Holes for the spring catch screws were drilled perpendicular to the guide rod holes 3/4-in. from the top of the impact mass. The catch screw holes were tapped to accept a 1-in. #8-32 UNC screw. To maintain clearance with the inside of the sleeve the catch screw holes were also countersunk to allow the head of the #8 socket head cap screw to be flush with the outside face of the impact mass.

The connection between the impact mass and the solenoid plunger was made with a stainless steel bolt threaded on both ends. One end is threaded with 1/4-in.-20 UNC to insert into the plunger, while the other is 1/4-in. 28 UNF (Unified Fine Thread) insert into the impact mass. The corresponding hole in the impact mass is centered and drilled

approximately 1-1/2-in. deep. Construction drawings of the impact mass are shown in Figure 3.5. Figure 3.6, showing an isometric view of the impact mass, is included for clarity.

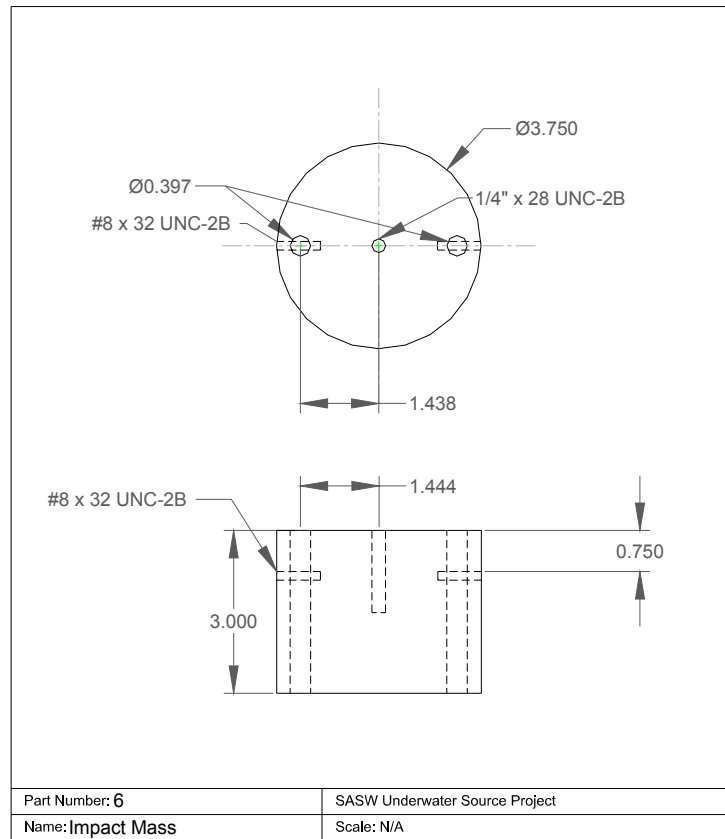


**Figure 3.5 Construction drawings of the impact mass.**

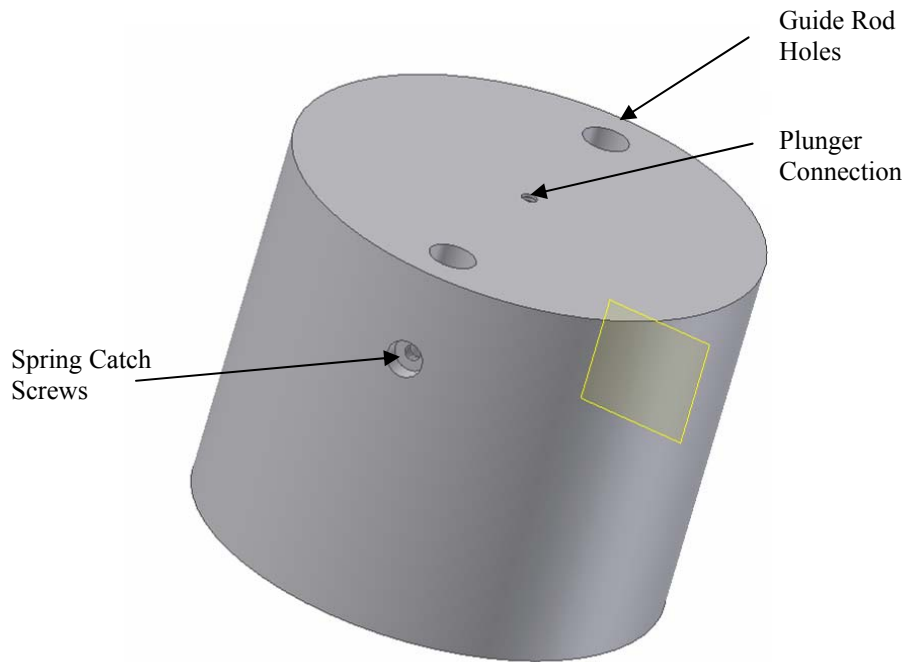


**Figure 3.6** Isometric view of impact mass.

### ***3.3.4.3 Other Internal Components***

Additional internal components were required in the design of the source. These components include: 2) sleeve, 3) mounting plate, 4) guide rods, and 5) return springs. The weight of these components was minimized to minimize inertial losses during the impact. Each of these components had several additional design considerations. The sleeve and mounting plate were required to hold the solenoid up and provide a space for the impact mass to travel. It was critical that these components are rigid and remain stationary during the impact to avoid energy losses in the system.

The guide rods serve the following three purposes: (1) act as a guide for the moving mass, (2) provide a housing for the return springs, and (3) restrain the inner components of the source from moving upward during energizing. The guide rods needed to be of sufficient diameter to house the return springs while fitting in to the

limited area. It was also important to have a thick enough wall on the rods to make slotting the rods for the spring connecting screw feasible.

Because the solenoid used is a single actuating unit, a return mechanism is required. Mechanisms including electric motors and additional solenoids were considered but springs were chosen as the return mechanism for simplicity and space limitations. Ideally the spring constant should be as low as possible to limit the amount of energy stored in the springs over the stroke of the solenoid. Since the springs were required to lift the impact-mass to the loaded position, long springs with low constants were chosen. The containment height was the limiting factor in the length of the return springs.

The sleeve was constructed of aluminum pipe with an outside diameter of 5-in. and a wall thickness of 3/8-in. The total length of the sleeve was 3.375 in. and 4 holes were tapped in the top to accept 3/4-in. #8-32 UNC screws from the mounting plate. The sleeve rests on the bottom cap and the mounting plate rests on top of it, therefore both ends of the sleeve were faced to ensure that they were smooth and perpendicular to the length of the cell. The finished weight of the sleeve is 1.75 pounds (0.79 kg). Construction drawings of the sleeve can be found in Figure 3.7.

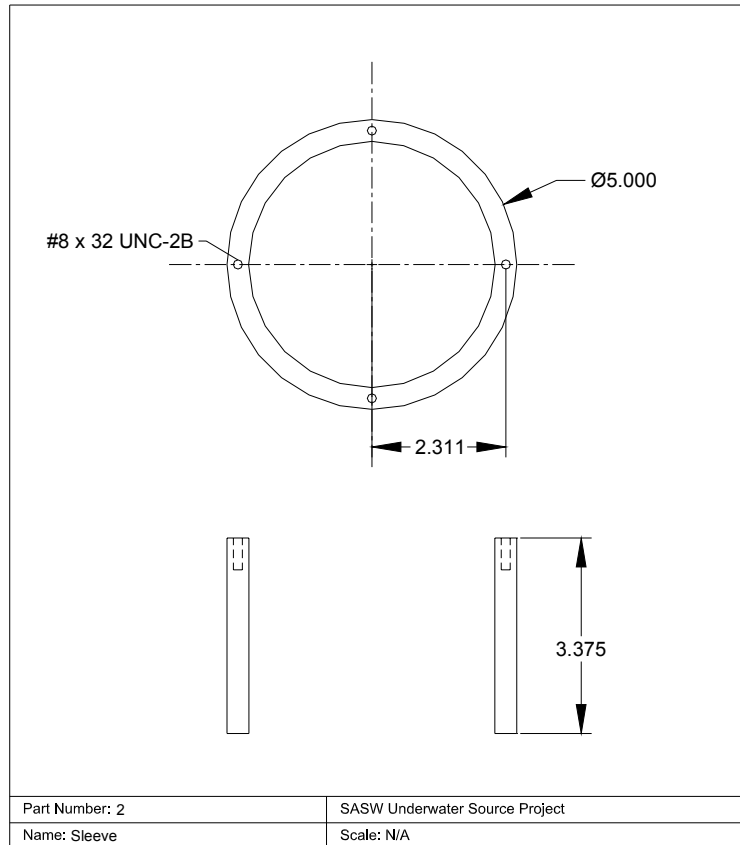


**Figure 3.7 Construction drawings of the sleeve.**

The mounting plate was constructed from a piece of aluminum bar stock. The 6-in. diameter stock was turned down in a lathe to 4.9-in. in diameter. It was then cut and faced on both sides to 5/16-in. thick. The plate required 4 holes matching those on the sleeve discussed earlier in this section. These holes were drilled as a free fit on a #8 machine screw, at 0.177-in. It also required holes to accept mounting screws from the solenoid base. These holes can be seen in Figure 3.8 as drilled and tapped holes for #8-32 UNC. The solenoid is fastened to the mounting plate using 1/2-in. #8-32 UNC screws. The plate also required holes to accept the brass guide rods. The guide rod holes were drilled to align with the corresponding assembly holes in the top and bottom caps. These holes were drilled for a close fit on 3/8-in. rods, at 0.38-in. The finished weight of

the mounting plate was 0.66 pounds. Construction drawings of the mounting plate are shown in Figure 3.8. .

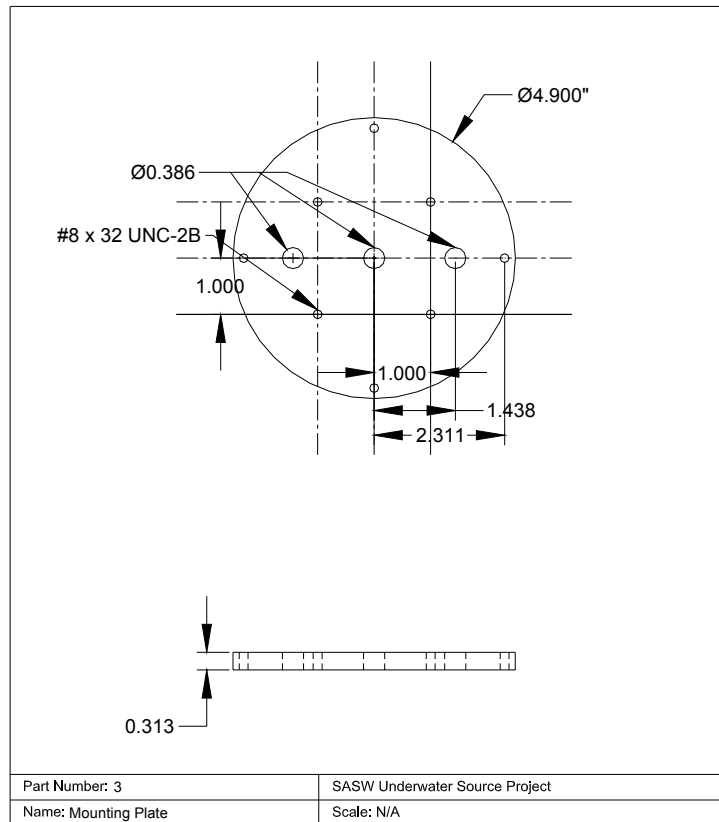


**Figure 3.8 Construction Drawings of the mounting plate.**

The two guide rods were constructed out of 3/8-in. outside diameter thin-wall brass tubing. The wall thickness of the tubing selected is 0.032-in. and the inside diameter is 0.311-in. The guide rods act as a vertical guide for the moving mass and are installed in the assembly holes in the top and bottom caps. During assembly the guide rods are passed through the mounting plate and the impact mass. They are connected to the impact mass by the return springs and inserted in the assembly holes in the top and bottom caps. To function as a housing for the return springs, the guide rods have been

modified to hold the spring at the top, and let the mass travel over the solenoid stroke. The 1/8-in. diameter hole at the top of the rod accepts a 1/8-in. diameter roll pin which retains the spring on one end. The slot located at the other end of the rod is sized to clear a #8 machine screw. Length and location of the slot were determined by the location of the spring catch screw in the impact mass and the amount of travel of the solenoid. The slot is oversized lengthwise to eliminate the possibility of the spring catch screw contacting the end of the slot on either end of its travel. Restraint of the inner source components is achieved by using shaft clamps positioned to create a rigid compression member between the top cap and the mounting plate. The shaft clamps are installed so that the distance between the mounting plate and the top of the guide rod is 5-in. With the shaft clamps installed properly the inner components of the source are restrained from upward movement when the solenoid is energized.

The guide rods perform several roles in the proper function of the source. When the source is in use, the assembly holes in the top and bottom caps keep the rods parallel with one another and aligned at all times. The moving mass is then free to slide on the rods over its entire range of travel. The finished weight of each guide rod, as shown in Figure 3.9, is 0.1 pounds.

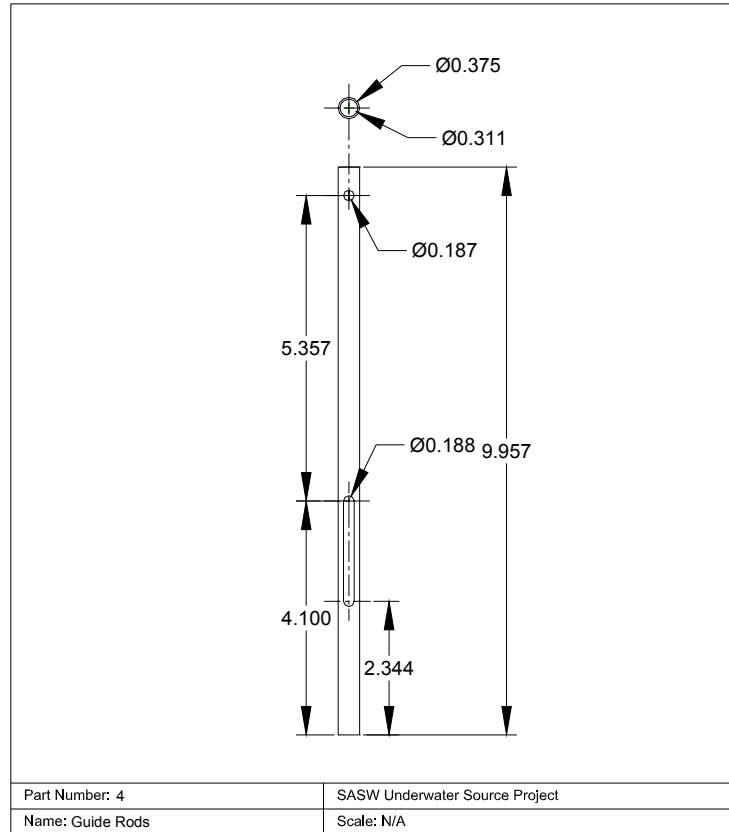


**Figure 3.9 Construction drawings of the guide rods.**

In the final design the return springs had to be able to hold approximately 5.5 pounds at an initial stretched length of approximately 5-in. The springs used were ordered from McMaster Carr, and are type 302 stainless steel wire. The outside diameter is 0.300-in., initial un-stretched length of 3-in., and a wire diameter of 0.037-in. The initial tension on the springs used is specified to be 0.806 pounds. At a stretched length of 5 inches the springs are generating 5.34 pounds of force each, which maintains the impact mass at the top of the solenoid stroke. The additional force dissipated in both springs over the stroke of the solenoid is 6.08 pounds. The dashed lines shown on Figure

3.10 are the spring lengths of interest in the return spring system and the force in the springs at those points.

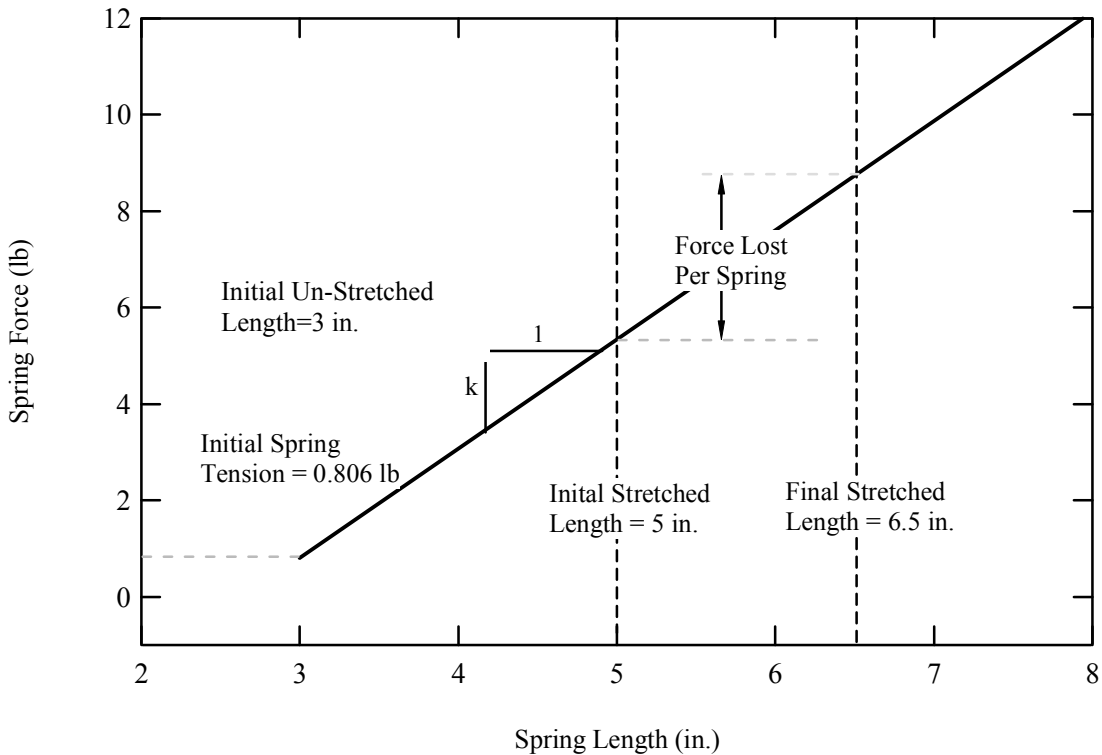


**Figure 3.10** Spring force per spring as a function of length for the return springs.

The return springs are installed first in the guide rods with roll pins. Once the springs are in the guide rods, the rods can be inserted through the mounting plate and the moving mass. A thin wire can then be used to stretch the spring through the guide rod until the end loop is in line with the spring catch screw hole in the moving mass. Once the end loop is in line the spring catch screw, the screw can be inserted through the guide rod, fixing the bottom spring loop to the moving mass.

#### ***3.3.4.4 Containment Cell***

Cell weight was a concern throughout the source design. Since the containment cell moves along with the impact mass, inertial loss associated with the mass of the containment cell was a primary design consideration. Weight was minimized where possible by using plastic components. Considerations when choosing a material for each component were the ease of machining, water absorption rate, availability, and cost. In addition, the materials also had to be reasonably pressure and temperature resistant.

The cell wall is constructed of 5-in. inside diameter schedule 40 PVC (polyvinyl chloride) pipe. The wall thickness is 0.25-in. and the final weight is 2.0 pounds. The cell wall was cut and faced to 8.5-in. long. The facing is critical for this component as both faces are used to seal against o-rings in the top and bottom caps. This method of o-ring sealing allows the cell wall to be easily reproduced in the case that the cell is leaking due to a scratch in the faced end. Construction drawings of the cell wall are shown in Figure 3.11.

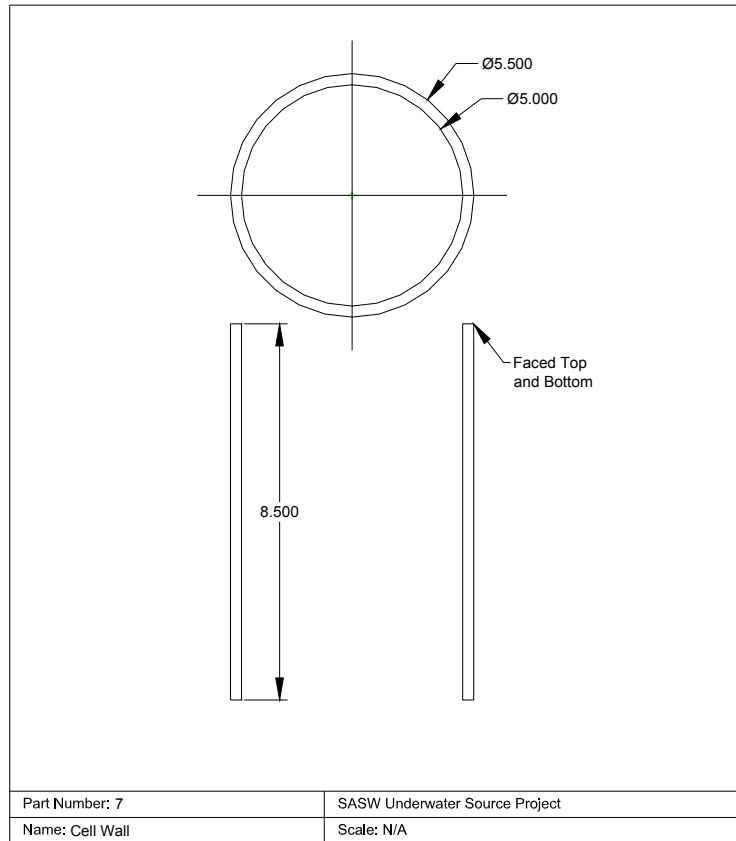


**Figure 3.11 Construction drawings of cell wall.**

Delrin® (registered trademark of DuPont) was selected for the top and bottom caps. With a specific gravity of 88.6 pounds per cubic foot it is very similar to PVC. Delrin® is relatively easy to machine, has a very low absorption rate, and high strength. An 8-in. diameter 4-in. thick cylinder was purchased from McMaster Carr for use as the top and bottom caps. Delrin® was not used for the cell wall because it was not available in the section required and machining of that section from solid stock was cost prohibitive.

The top cap is a 1-in. thick, 8-in. diameter cylinder which was cut and faced on both sides. A seating groove was cut in the top cap to receive the cell wall. In the center of the seating groove an o-ring groove was cut to accept a 1/8-in. rubber o-ring. The o-

ring groove is then centered on the thickness of the cell wall when the source is fully assembled. The top cap also contains assembly holes to receive the guide rods discussed in Section 3.3.4.3. The assembly holes were drilled with 3/16-in. deep straight sides. The holes were aligned, as shown in Figure 3.12, with respect to the clamp rod holes. The clamp rod holes were drilled as a tight fit on the 3/8-in. diameter clamp rods, at 0.386-in.

The “downhole” components of the electrical system (discussed in Section 3.3.5) are mounted to the inside of the top cap. This is accomplished using the 4 holes, shown in Figure 3.12, drilled and tapped for #8-32 UNC. Another feature of the top cap is the plug mounting hole. To accomplish plug mounting, a 7/8-in. diameter hole was drilled and reamed in the location seen in Figures 3.12 and 3.13. A 1/16-in. diameter o-ring groove was installed in the hole 3/8-in. down from the top of the cap. The o-ring groove was fitted with a rubber o-ring to create a water-tight seal at the plug hole. The plug is held in place by 3/8-in. #4-40 UFC stainless steel socket head cap screws drilled and tapped into the top side of the top cap.

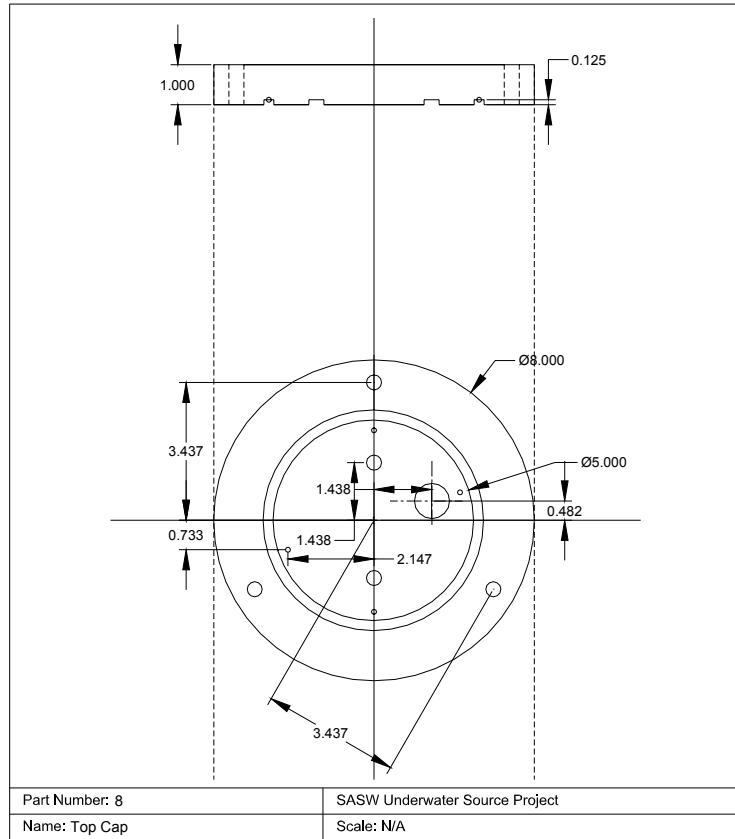


**Figure 3.12 Construction drawing of top cap.**

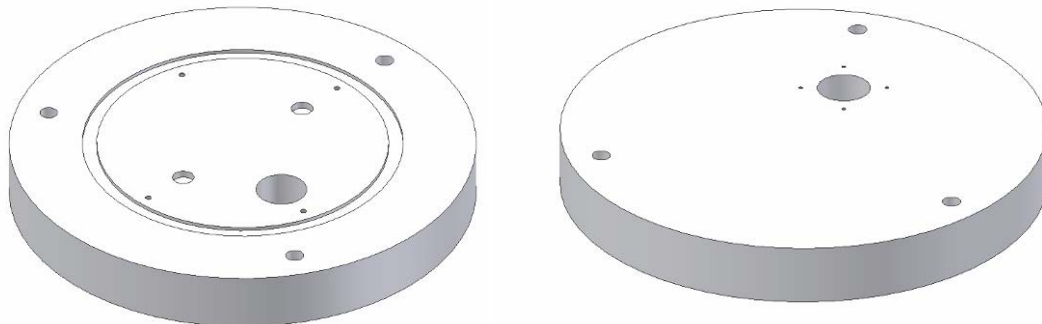


**Figure 3.13 Isometric view of the inside and outside of the top cap.**

The bottom cap is also constructed of Delrin® for reasons previously discussed. The bottom cap is 2.82-in. tall, and has a profile as shown in Figure 3.13. The bottom profile was intended to minimize contact area depending on surface conditions. Since

short wavelength surface waves will not be generated from a large footprint area, it was important to keep the contact area as low as possible while still remaining functional. Due to the rounded shape, the contact pressure decreases as the source subsides into the surface of the underwater sediments. In very low shear strength materials, the subsidence may continue until the flange section of the base cap contacts the surface. If the embedment depth is less than 1.82-in., the contact surface area can be estimated as the surface area of a partially embedded sphere, as:

$$A = \pi * h * d \quad (3.1)$$

where  $A$  is the contact area,  $h$  is the embedment depth, and  $d$  is the diameter of the sphere. If the embedment depth is greater than the distance from the bottom of the flange to the bottom of the cap the contact area can be calculated by the sum of the spherical contact and the contact area of the bottom flange, as:

$$A = \pi * h * d_s + \frac{\pi}{4} (d_F^2 - d_s^2) \quad (3.2)$$

where  $A$  is the contact area,  $h$  is the depth of embedment,  $d_s$  is the diameter of the sphere, and  $d_F$  is the outside diameter of the flange. In this case, the flange has a fixed outside diameter of 8 in. and, therefore, a maximum estimated contact area of 58.6 in<sup>2</sup>.

Material was removed from the center of the bottom cap on the inside of the cell for two reasons. The first was to lower the weight of the containment by removing unnecessary material. The second was to lower the center of gravity of the cell by creating a void space for the moving mass to enter at the bottom of the solenoid stroke. The additional travel allowed the total height of the cell to be reduced.

The bottom cap also contains assembly holes to receive the guide rods discussed in Section 3.3.4.3. The assembly holes were drilled with 3/16 in. deep straight sides. The holes were aligned to match the top cap and the moving mass, as shown in Figure 3.14 and Figure 3.15.

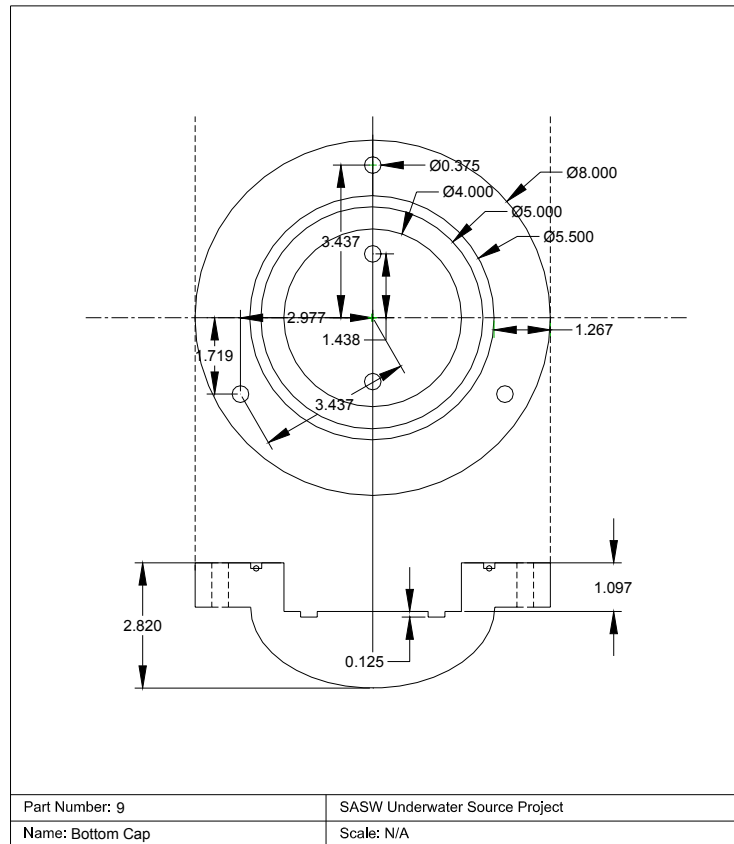


**Figure 3.14 Construction drawing of bottom cap.**



**Figure 3.15** Isometric view of the inside and outside of the bottom cap.

Three clamp rods are spaced symmetrically around the top cap and the flange of the bottom cap. The rods are used to clamp the cell together as well as guides for the hold-down reaction mass. Clamp rods were fabricated from 3/8-in. stainless steel bar stock cut to 12-in. in length. Ends of the bar stock were threaded at 3/8-in.-16 UNC. A nylon insert lock nut is used on the bottom of the clamp rods and pair of jam nuts is used on the top to allow tension to be maintained under field conditions.

#### ***3.3.4.5 Reaction Mass***

A hold-down force is required to maintain ground contact because the energized solenoid force acts on both the impact mass and containment cell. A loss in ground contact will occur if no external force is applied to the containment cell. The hold-down force design is achieved by suspending the reaction mass on compression springs. Because additional weight rigidly attached to the containment cell would create large inertial losses, the spring suspension was used to isolate the motion of the containment cell from that of the hold-down mass. The spring-mass system was, therefore, designed to have a resonant frequency below the frequency of interest.

The reaction mass consists of several pieces. The plate is a circular piece of 1/4-in. steel plate with a 12-in. outside diameter and a 6-in. inside diameter. Holes drilled in the plate were spaced to match the clamp rod holes on the top and bottom cap. These holes were drilled as free fitting for the 3/8-in. diameter clamp rods, at 0.397 inches. Additionally, holes were symmetrically placed to allow for the attachment of lead weights. The weights were attached using 3-in. long 1/4-in. 20 UNC stainless steel bolts with a nylon insert lock nuts. Steel plates matching the shape of the weights were fabricated to act as washers on the underside of the lead weights.

The lead weights were shaped in a mold fabricated from 1/4-in. steel plate. The mold was lined with aluminum foil and molten lead was poured into the mold. The aluminum foil was used to ease the extraction of the cooled lead pieces from the mold. To maintain symmetry in the reaction mass the weights were calibrated so all three weights with their steel washer plate weighed very close to the same. Table 3.2 shows the weight of each component of the reaction mass. The reaction mass is assembled as shown in the exploded isometric view shown in Figure 3.16. Hole locations can be found in the construction drawings of the plate in Figure 3.17.

**Table 3.2 Components and weights of reaction mass.**

Component	Weight (lb.)
Mass 1	6.39
Mass 2	6.38
Mass 3	6.32
Ring	4.52
Hardware	0.3
Total	23.91

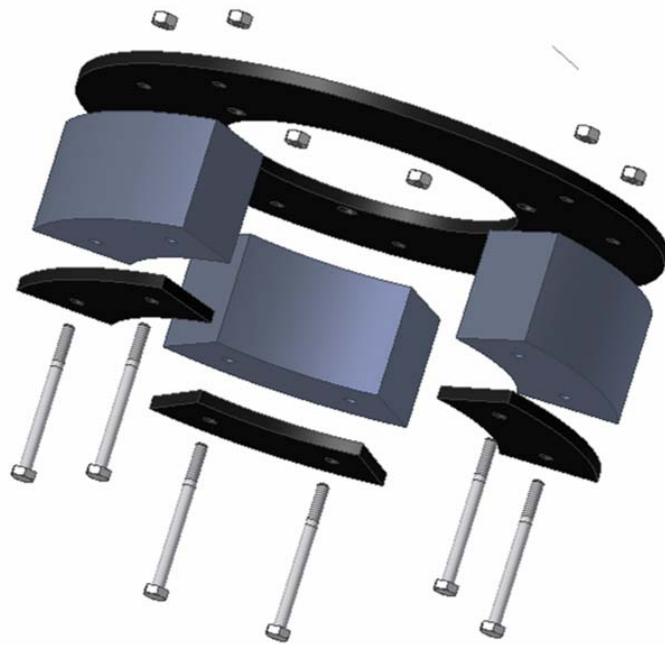


**Figure 3.16** Exploded isometric view of reaction mass components.

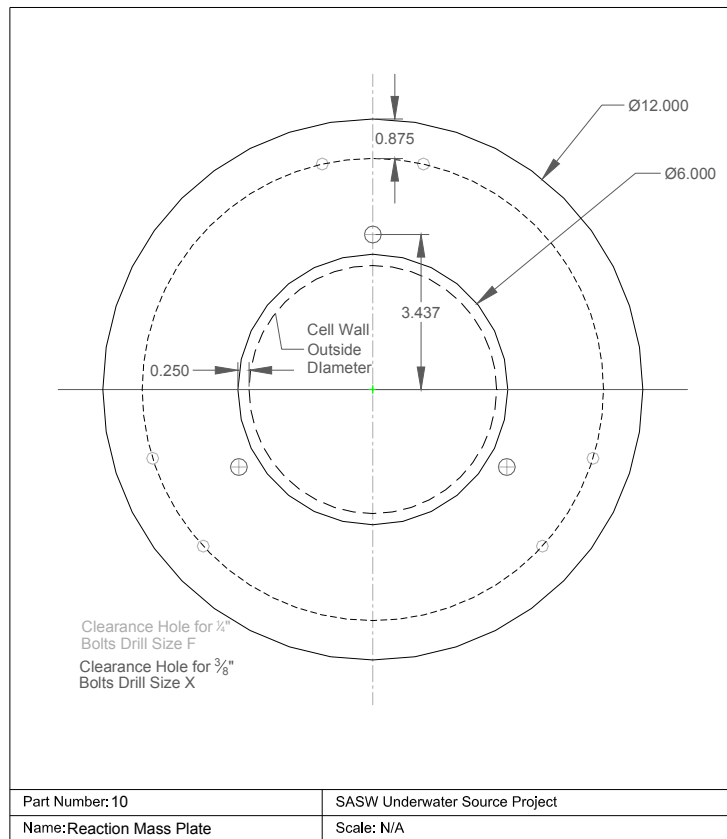


**Figure 3.17** Construction drawings of reaction mass plate.

The reaction mass is suspended from the containment cell with three compression springs. One spring rides on each of the clamp rods and fits between the reaction mass and the flange on the bottom cap. The springs used to suspend the reaction mass are zinc plated, 5-in. long, compression springs. Using the outside diameter, 5/8-in., and the wire diameter, 0.05-in., the spring constant can be estimated to be 2.65 pounds per inch per spring. The 3 suspension springs in parallel have a combined spring constant of about 8 pounds per inch. The 5-in. springs compress to approximately 2 inches when suspending the 24-lb reaction mass.

The resonant frequency of the reaction mass system was designed to be as low as possible since the containment cell will move independently from the reaction mass at frequencies above the resonant frequency of the reaction mass system. The reaction mass system will absorb energy generated by the impact that is at or near the resonant frequency, which is an undesirable condition. For the profile depth of interest in this study, the lowest frequencies of interest will be above 7 Hz. Therefore the reaction mass system should be designed with a resonant frequency well below 7 Hz. The resonant angular frequency of the spring-mass system can be calculated using :

$$\omega = \sqrt{\frac{k}{m}} \quad (3.3)$$

where  $\omega$  is the natural angular frequency of an idealized spring mass system with spring constant,  $k$ , and mass,  $m$ . The mass of the reaction mass is the weight divided by  $g$  (32.2 ft/sec<sup>2</sup>) or 0.74 slugs. The spring constant used is the parallel combined constant of 7.95

pounds per inch. The natural circular frequency of the system is estimated to be 3.27 radians per second.

$$f = \frac{\omega}{2\pi} \tag{3.4}$$

Using the natural circular frequency, the resonant frequency of the system can be calculated using Equation 3.4. In this case the resonant frequency is approximately 0.5 Hz, which is well below the frequencies of interest.

### **3.3.5 Power System Design**

The goal of the power system design was to develop a circuit that would allow for remote powering and triggering of the solenoid. Due to the potential for very long cable lengths in deep water, it was decided to charge a bank of capacitors located in the source with low-amperage current instead of directly firing the solenoid with high-amperage current. The circuit used is based on a circuit designed originally by Frank Wise at the University of Texas at Austin. It consists of two main components, surface control components and power supply components, as shown in the circuit diagram in Figure 3.18.

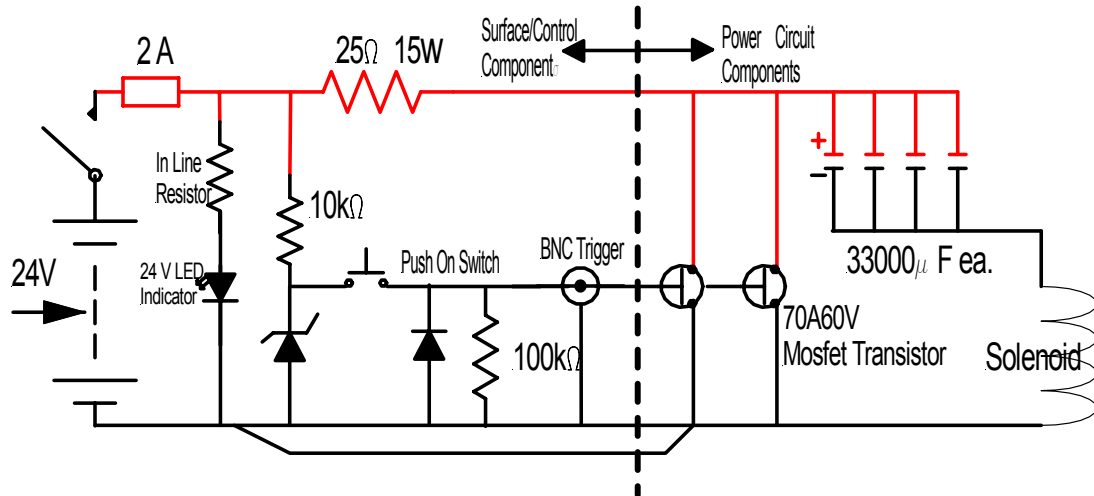


**Figure 3.18** Circuit diagram for source power and control.

### 3.3.5.1 Surface Components

The surface components consist of the triggering circuit, front side of the charging circuit, and switching and safety equipment. Power to all components is switched at the battery. All power is then routed through a 2-amp fuse and a daylight visible LED (light emitting diode) which indicates power is on and the fuse is intact. At this point the circuit splits into the remaining two components, the charging circuit and triggering circuit. The charging circuit consists of a 25-ohm resistor which decreases the current charging the capacitors to approximately 1 ampere. The capacitor charge time is influenced by the magnitude of this resistor and can be adjusted by changing the resistor. Using the 25-ohm resistor the capacitor charge time is approximately 20 seconds.

The trigger circuit uses either manual or computer-controlled triggering. This is accomplished by a 10-kilo ohm resistor and a 10-volt zener diode acting as a voltage regulator for the trigger circuit. The manual switch is a push-on type switch rated for 2 amperes. The computer controlled triggering is accomplished with a BNC (barrel nut

connector), the 100-kilo ohm resistor, and the 10-volt diode. The combination of the resistor and diode allow a computer or function generator to be used to provide a trigger signal while eliminating the possibility of reversing the voltage and damaging the computer. The finished surface component circuit mounted on perforated circuit board is shown in Figure 3.19.

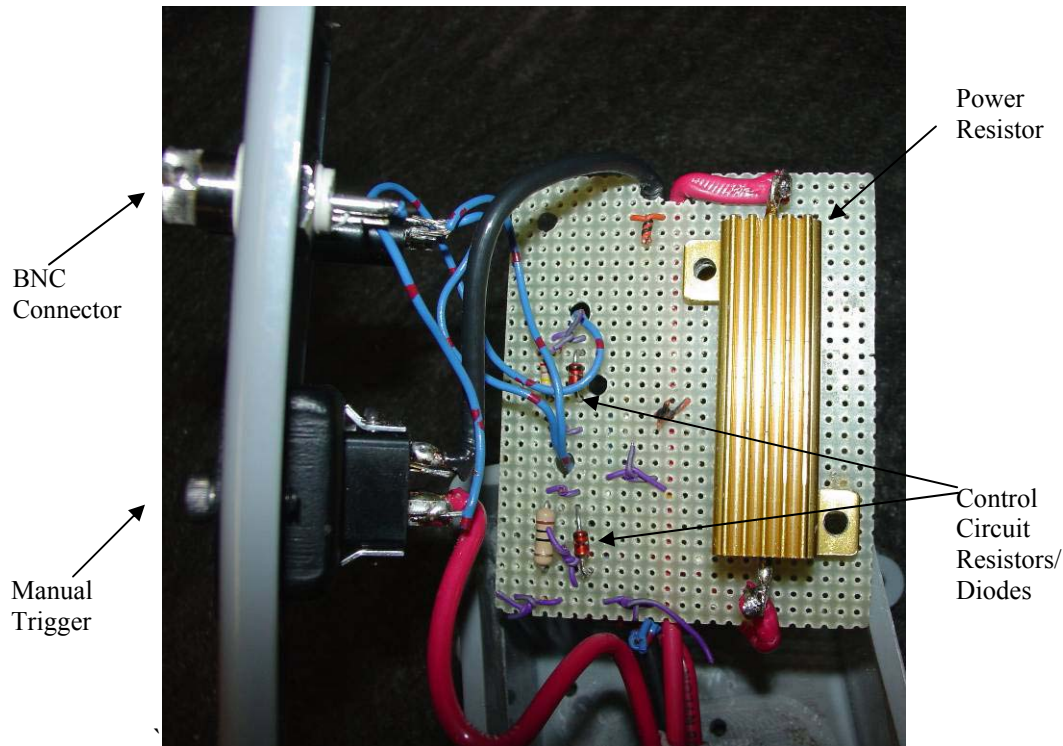


**Figure 3.19** Photograph of assembled surface component circuit.

The surface components of the electrical system have been mounted in an exterior grade PVC junction box. To create a portable power supply, the junction box is mounted inside of a PVC battery box and covered with a lid. Figure 3.20 shows the mounted junction box as well as the wiring for the switch, fuse, and indicator lamp. Figure 3.21 shows the finished battery box.



**Figure 3.20** Surface component junction box mounted to the underside of battery box lid.



**Figure 3.21** Finished battery box.

### **3.3.5.2 Seafloor Components**

The velocity of the solenoid plunger and mass at impact will influence the amplitude of the surface wave motions, as discussed in section 3.3.1. A capacitor bank mounted close to the solenoid is used to rapidly energize the solenoid. The capacitors are

discharged using MOSFET (Metal Oxide Silicon Field Effect Transistor) transistors as remote switches. The transistors close when a minimum voltage is sourced to them from the triggering circuit. Two transistors were used in parallel in this circuit for redundancy.

Capacitors selected for use in the capacitor bank are four, 24-volt Panasonic TS-UP aluminum electrolytic 33,000- $\mu$  farad capacitors. The capacitors are wired in parallel producing an equivalent capacitance 0.132 farads and are charged from the surface with a 24-volt, 1 ampere signal. The Panasonic capacitors were selected because they are relatively compact, with a cylindrical case 30 mm in diameter by 50 mm long (1.18 inches by 1.97 inches respectively), and they possess a low ESR (Equivalent Series Resistance) of 0.02 ohms. Capacitors with low ESR are capable of fast rise times for both charging and discharging.

The seafloor components were assembled on a perforated circuit board as shown in Figure 3.22 and 3.23. The circuit board is reinforced with a ring of solid fiberglass circuit board material. The power circuit assembly is mounted to the inside of the top cap using  $\frac{1}{2}$ -in. #8-32 UFC coupling nuts as standoffs. The space requirements for the capacitors and the layout of the power circuit assembly can be seen the construction drawings in Figure 3.24.

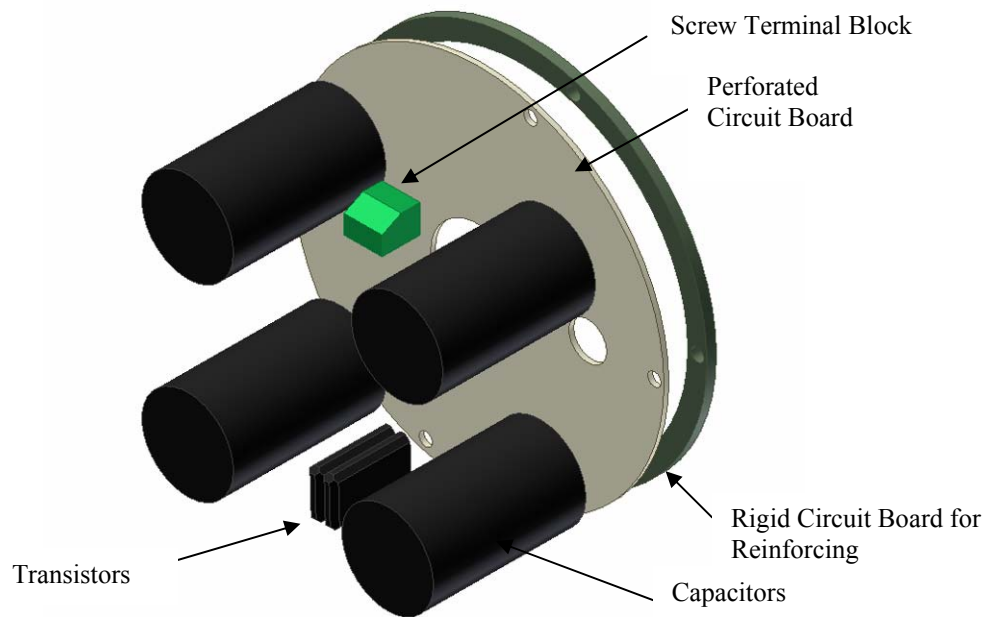


**Figure 3.22** Exploded isometric view of power circuit.

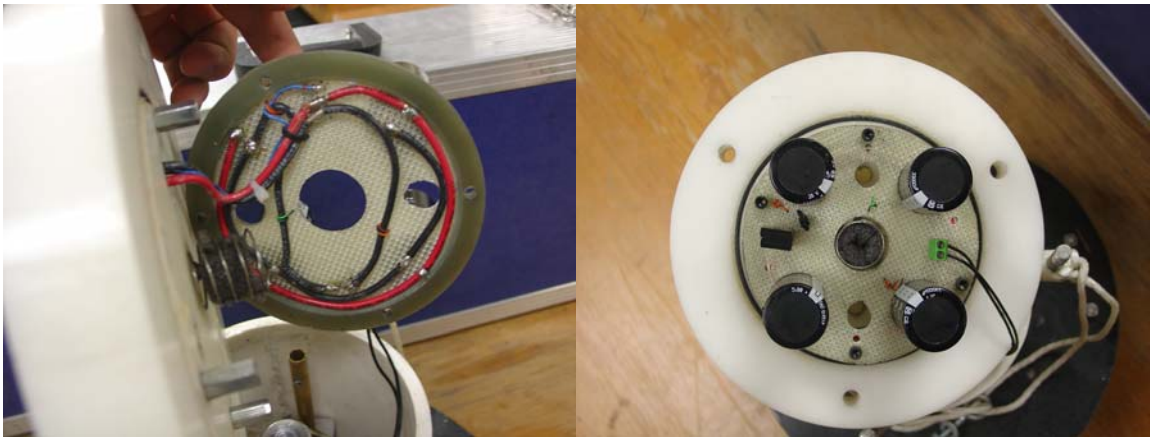


**Figure 3.23** Photograph of finished power circuit.

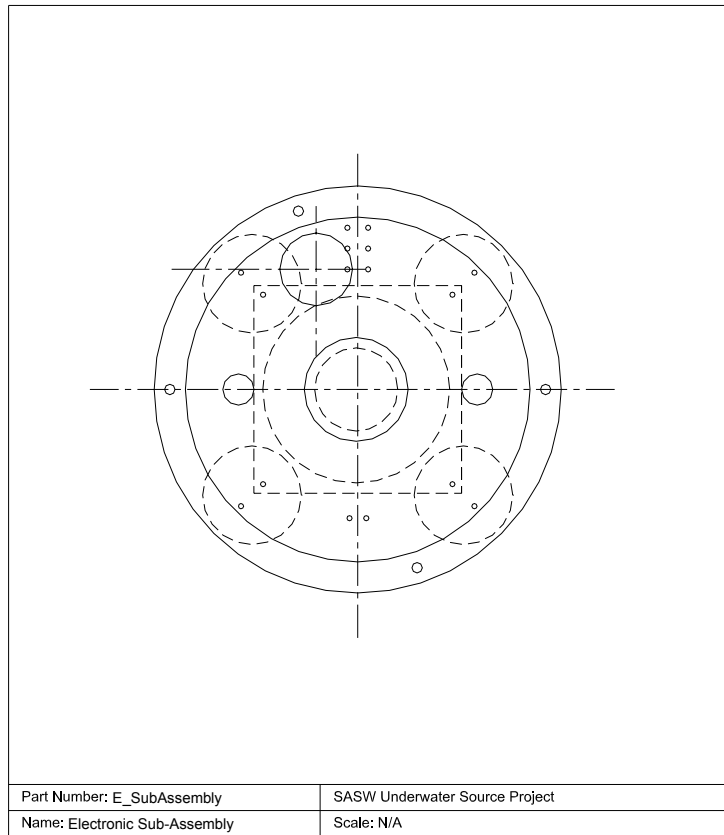


**Figure 3.24 Construction drawings for the power circuit board.**

### ***3.3.5.3 Cabling and Connections***

The surface components and power circuit are connected via a 3-conductor cable. The cable is a rubber jacketed type SJOW (*UL*) extension cord which will remain flexible over a wide range of temperatures. The surface components are connected using a 4-conductor Cinch® connection with a P304CCT plug and a S304AB panel mount socket mounted in the battery box. The connection at the source is made with an Amphonal® MS3102E-16 panel mount receptacle and a MS3106E-16S straight plug both with a 3-pin arrangement. The connection at the source was ordered from the environmental series, meaning the pins are solder on connections permanently mounted in the plug housing on both sides. The pins are molded into the plug housing and, therefore, the source will

remain water-tight even if the plug or cord jacket is compromised. The plug was mounted in the top cap to be water-tight as discussed in Section 3.3.4.4. A photograph of the plug ends and sockets is shown in Figure 3.25.



**Figure 3.25** Photograph of the cord ends and sockets.

### **3.3.6 Geotechnical Design Issues**

#### ***3.3.6.1 Bearing Pressure***

The bearing pressure of the cell is a function of the cell footprint and the weight of the cell. The bearing pressure changes with embedment as discussed in Section 3.3.4.4 due to the shape of the bottom cap. Final measured dry weights of the components are shown in Table 3.3.

**Table 3.3 Final weights of all components.**

Part Number	Name	Weight (lb.)
1	Solenoid (and Plunger)	1.93 (0.62)
2	Sleeve	1.75
3	Mounting Plate	0.66
4	Guide Rod	0.10
5	Return Spring	0.00
6	Moving Mass	9.68
7	Cell Wall	2.00
8	Top Cap	3.58
9	Bottom Cap	4.16
10	Reaction Mass	23.91
11	Clamp Rods	0.66

The measured weight of the entire cell is 49.5 pounds, which includes all fasteners used in the assembly. The submerged weight of the assembled cell was found to be 35.5 pounds.

Equation 3.5 describes how the contact pressure is calculated from the submerged weight and the embedment depth.

$$q = \frac{W_{sub}}{\pi * h * d} \quad (3.5)$$

The term  $q$  is used to describe contact pressure,  $W_{sub}$  is the submerged weight of the cell,  $h$  is the depth of embedment assuming a spherical contact area, and  $d$  is the diameter of the sphere. By rearranging the bearing capacity equation, as shown in Equation 3.6, the undrained shear strength of a material required to fail in bearing capacity can be calculated.

$$C_u = \frac{q}{N_c} \quad (3.6)$$

Where  $C_u$  is the undrained strength,  $q$  is the contact pressure, and  $N_c$  is assumed to be Vesic's bearing capacity factor for a  $\phi'=0$  material of 5.1. The other terms of the bearing capacity equation have been dropped because the source is sitting on the surface. Table 3.4 summarizes the calculations described above for several embedment depths assuming a perfectly spherical 5.5-in. diameter contact surface until 1.82-in. of embedment. At 1.82-in. of embedment, the contact area is estimated to be 58.0 square inches as discussed in Section 3.3.4.4. The submerged weight was used to calculate values reported in Table 3.4. The low required undrained strengths indicate the source will cause a bearing failure for only the softest normally consolidated soils.

**Table 3.4 Estimated surface area, contact pressure, and undrained strength required not fail for several different embedment depths.**

Embedment Depth (in.)	Contact Surface Area, $A$ (in <sup>2</sup> )	Contact Pressure, $q$ (psf)	Required Undrained Strength, $C_u$ (psf)
0.50	8.6	591.7	116.0
1.00	17.3	295.9	58.0
1.50	25.9	197.2	38.7
1.82	58.0	88.2	17.3

Similar calculations can be performed for the case of sandy conditions. The ultimate bearing capacity can be calculated from:

$$q_{ult} = \frac{1}{2} \gamma B N_\gamma \quad (3.7)$$

where  $\gamma$  is unit weight,  $B$  is the width (or diameter) of the footing and  $N_\gamma$  is the bearing capacity factor. For the case of a friction angle of 30 degrees the bearing capacity factor is 22.4. At an embedment depth of 1.82 inches, the diameter of the base is 8 in.

Assuming a submerged unit weight of 40 psf, the ultimate bearing capacity can be calculated to be approximately 300 psf which is greater than the contact pressure.

### ***3.3.6.2 Effect of Footing Size on Wavelengths Generated***

A second issue concerns the generation of short wavelengths that are needed to resolve near-surface (top 1 to 2 feet)  $V_s$  profiles. As the wavelength approaches the size of the impact plate, the ability to generate surface waves is compromised due to destructive interference.

The source footprint was, therefore, a concern for both bearing pressure and wavelength generation. Contact pressure needed to be kept as low as possible while the source footprint needed to be small enough to generate short wavelength energy. The domed base incorporated in the final design creates a variable contact area depending on embedment depth as discussed previously. The shortest wavelengths capable of being generated are on the order of 3 times the source diameter. In the case where the embedment depth is maximized, the contact area is an 8-inch diameter circle limiting generated wavelengths to approximately 24-inch minimum. If the bearing capacity is such that only a minimum embedment depth is required the minimum expected wavelength is reduced, and the near-surface resolution is improved.

## **3.4 Receiving Instrumentation**

### **3.4.1 Geophones**

For most soil sites, the frequency range of interest will range from approximately 7 to 500 Hz. In this frequency range, particle velocity transducers (geophones) are effective receiving instrumentation. Geophones with a resonant frequency of 4.5 Hz

were used in all field experiments requiring velocity transducers. The 4.5-Hz geophones purchased from Geospace LP, shown in Figure 3.26, are constructed using a rotating dual coil design which is more durable in rough handling conditions than single coil designs. The model number GS-11D geophones are cased in model 902 marsh cases from Geospace. The marsh cases include a double o-ring seal and a rubber neck strain relief system making them water resistant. They can also be fitted with a spike for on-land testing applications or an aluminum disk for pavement and other hard surface applications.

Geophones were assembled from the case components seen in Figure 3.26. Pigtail wires were installed on the geophones for on-land use. An assembled geophone used in on-land testing is shown in Figure 3.27.



**Figure 3.26** Geospace LP 4.5 Hz geophone and marsh case assembly.



**Figure 3.27** Assembled geophone ready for field use.

Geophones used in underwater testing were potted in a two-part epoxy. Potting the marsh cases allowed improve water resistance as well as the ability to install mounting hardware and approximately 1 lb. of lead shot as ballast. Future designs may incorporate commercially available gimballed geophones for use in underwater testing which provide self-righting ability as well as factory waterproofing.

The epoxy form was constructed from a 3-in. diameter concrete cylinder mold cut into 1-in. tall disks, a 1-½-in. PVC pipe coupler, and a 1-¼-in. tall piece of 1-½-in. PVC. The mold was fitted with ¾-in. zinc plated eye bolts located ¾-in. from the base of the mold. Nuts were left on the threaded eye bolts to provide additional resistance against pullout. The base section was poured first and approximately 1 pound of lead shot was placed in the wet epoxy. The addition of the lead shot provided the geophones with a lower center of gravity intended to help stabilize the receivers and prevent overturning. Once the base section hardened, the additional sections of the mold were placed on top and held in place with a ring stand. All interior portions of the mold were coated with white lithium grease to ease de-molding. The upper section of PVC pipe was taped into the PVC coupler to maintain alignment during the pour. The PVC coupler was caulked to the hardened base to seal it during the pour. Both PVC sections were cut longitudinally with a reciprocating saw prior to pouring so that they could be split after the epoxy had hardened. Figure 3.28 shows a geophone with the base hardened and the upper mold ready to be poured. A finished potted geophone can be seen in Figure 3.29.



**Figure 3.28** Intermediate step in geophone potting.



**Figure 3.29** Finished de-molded potted geophone.

The potted geophones were tested against the standard spiked geophones to ensure that the characteristics of the receivers had not been changed. A comparison of the potted geophone to a standard spiked geophone can be seen in Figure 3.30. This comparison was made at the on-land test site described in Chapter 4, and a similar comparison is expected on softer materials. The comparison shows the potting has a negligible effect on the amplitude and phase of the signal received at the geophone. This system for underwater testing, although not ideal, provided an affordable underwater measurement system.

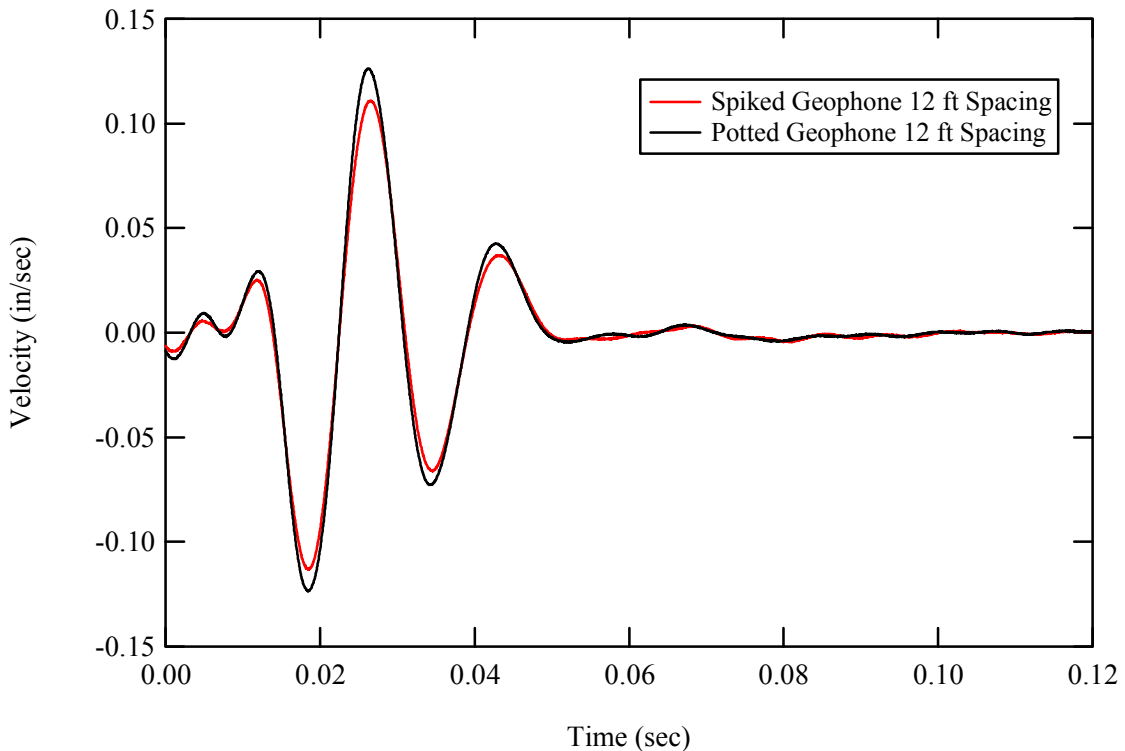


**Figure 3.30** Time record recorded from potted geophone and spiked geophone from same impact.

### **3.4.2 Hydrophones**

Hydrophones with a natural frequency of 6 Hz were purchased from Geospace LP (Model MP-24 L1). The hydrophones consist of 4 piezometric crystals used in the bender mode and arranged to cancel acceleration. The hydrophones are cased in a permanent plastic housing with a waterproof 2-conductor cable. The plastic case is molded to allow access to the crystal pot in order to check the polarity of the receiver. Hydrophones were used without modification as supplied from Geospace.

### **3.4.3 Deployment Frame**

In order to maintain receiver spacing and orientation with respect to the source, a mounting frame was needed. The main design criteria for the frame was that it be low weight for deployment and transportability. In addition, waterproof geophones and hydrophones were to be mounted to the frame out to a distance of 20 feet from the source. The frame also needed to be durable enough to retrieve receivers and the source in the case that it was restrained underwater.

The frame was constructed as a space truss using a triangular cross section that tapered in both directions from one end. The taper was intended to reduce cross member length and weight at the end furthest from the source. The material used for the frame was galvanized Electrical Metal Tubing (EMT) electrical conduit. The material is relatively lightweight at approximately 0.44 pounds per foot and durable. To address the transportability concern the frame was cut into several sections. The lengths of the sections were designed to allow for the most flexibility in receiver locations close to the source. The length and weight of each section can be found in Table 3.5.

**Table 3.5**      **Lengths and weights of frame sections.**

Section	Length (ft)	Weight (lb.)
1	4' -3"	7.67
2	7	11.18
3	5	7.58
4	4' -9"	6.67
Total	21	33.1

The conduit sections are connected using 3-in. and 3-<sup>1</sup>/<sub>4</sub>-in. long sections of black sprinkler pipe lathed down to the appropriate diameter for a snug fit. One long piece of sprinkler pipe was used at each connection to ease in the alignment of the frame pieces. A 5/16-in. hole was drilled in the sprinkler pipe <sup>3</sup>/<sub>4</sub>-in. from the end to allow for removable connecting bolts. The hole was aligned with a hole drilled in the frame and a bolt was installed in the hole. Once the connecting pipe sections were installed the frame was assembled and the connecting pipes were plug-welded in predrilled holes on the opposing side of the connection as the bolts.

Geophones were mounted using 1/4-in. twisted nylon rope tied through eye bolts installed on the receivers during the water proofing process as discussed in Section 3.4.1. The rope was tied to standoff clamps for the 3/4-in. EMT tubing. Rope was used as the connecting member to limit the transmission of energy directly through the frame to the receivers. The amount of slack in the connecting ropes and the location of the receivers was adjusted by sliding the EMT clamps longitudinally along the frame members. A geophone with the mounting hardware can be seen in Figure 3.31.



**Figure 3.31 Geophone mounted in frame with hardware.**

The hydrophones were mounted to the frame in a suspended orientation by looping the hydrophone wire and “zip tying” it to the upper member of the frame. The zip tie allowed a tight connection to the frame that could still be adjusted to maintain the suspension desired. The hydrophones could then be removed from the frame for transportation purposes.

### **3.5 Data Acquisition**

Data acquisition was an important part of evaluating source performance. The system used for data acquisition was required to have high dynamic resolution to allow for the collection of small signal amplitudes. The system was also required to have an adjustable frequency range to allow testing at stiff or soft sites. The system also needed to be portable to ease field data collection.

Existing 2-channel dynamic signal analyzers were used because a multi-channel system was not readily available. A dynamic signal analyzer is an instrument for

measuring the characteristics of dynamic signals in the time and frequency domains. The first is a PC card based two-channel analyzer from Data Physics paired with software written specifically for that analyzer. The second is a Hewlett Packard 3562A Dynamic Signal Analyzer used in conjunction with a laptop computer and a National Instruments NI-488.2 GPIB interface card. Originally data acquisition was performed by the Data Physics system designed for portability. It was concluded that this system was insufficient due to the lack of an external trigger-channel and lower dynamic resolution, so the Hewlett Packard system was adopted. Both systems are described below.

### **3.5.1 Data Physics**

The first system used was a two-channel dynamic signal analyzer from Data Physics Corporation with accompanying SignalCalc software package. The dynamic signal analyzer is a type 3 PC card (PCMCIA) based device which is used in a laptop computer. The Data Physics ACE system is capable of two input and two output channels and has an integrated signal conditioner powered by the laptop for use with accelerometers. Other specifications related to the Data Physics Ace system are; 100 dB dynamic range of signal acquisition and 20 kHz frequency span. A Pelican 1520 waterproof case was fitted for the computer, and a junction box was mounted to the bottom side of a custom mouse pad to allow cables from the receivers to be connected from the top and provide protection for the SignalCalc ACE card. The junction box has been labeled for input and output signals at both connections. The computer, case, and mouse pad can be seen in Figure 3.32.



**Figure 3.32** Field data acquisition system using the Signal Calc Card.

### **3.5.2 Hewlett Packard System**

The Hewlett Packard 3562A Dynamic Signal Analyzer is capable of recording two input channels, has the ability to utilize an external trigger, and has one output source channel. The Hewlett Packard instrument has a dynamic range of 80 dB, and an adjustable frequency range with a maximum span of 100 kHz. The analyzer was run from a small generator connected to a constant voltage transformer. Data collected with the Hewlett Packard Analyzer was transferred directly into plotting software and saved as general text files for additional processing.

## **CHAPTER 4. ON-LAND TESTING**

### **4.1 Introduction**

The system described in Chapter 3 was tested on land and compared to data collected using typical surface wave instrumentation for shallow surface wave testing. Data collected with a conventional surface wave testing source was used as a baseline to evaluate the remote source. This chapter presents comparisons of time and frequency data collected using both sources. Field testing procedures are discussed along with modifications to the source resulting from the field tests. The surface wave data collected using both sources is also analyzed and discussed.

### **4.2 On-Land Testing Procedure**

#### **4.2.1 Location**

On land comparison testing was performed at the University of Missouri Geotechnical Research Facility at Midway. The facility is a recent acquisition of the Civil Engineering department, and this testing was performed in the early stages of site characterization. The facility is located on US Highway 40 West, approximately 3 miles north of Interstate 70. Preliminary testing was performed in January and February, 2005, and final testing was performed from April through June, 2005. A photo of the general test area is shown in Figure 4.1.



**Figure 4.1 Photo of Geotechnical Research Facility at Midway**

#### **4.2.2 Instrumentation Used**

Standard 4.5-Hz geophones from Geospace LP were used as receivers for all on-land testing. The source energy used for the baseline testing was an 11.8-lb sledge hammer. The hammer was freely dropped from a height of approximately 6-in.

#### **4.2.3 Field Testing Procedure**

Two different field procedures were used to evaluate the solenoid source on land. First, time records were collected at 1-ft intervals out to a distance of 30 ft from the source using both the hammer source and the solenoid source that was developed in this research. The time records were compared in terms of signal amplitude and frequency content.

Secondly, data sets were collected for SASW and multi-channel data processing to assess the consistency of dispersion data generated from both sources. The set-up used for the SASW analysis was similar to the procedures described in Chapter 2 except the source was located at a fixed location to be consistent with the deployment geometry used underwater. Receiver pair spacing was varied from 2 feet to 25 feet in both comparison tests. Multi-channel analysis of the data was performed on the time records generated from each source. Details of the analysis are presented in Section 4.5.2.

### **4.3 Preliminary Testing of Source On Land**

After initial construction of the source had been completed, a troubleshooting program was used to evaluate and improve the source impact characteristics. The tuning program involved preliminary field tests and slight modifications to the source to improve the performance. No major changes in conceptual function were required during the tuning period.

#### **4.3.1 Results from Preliminary Testing**

Preliminary testing revealed the presence of pre-impact and post-impact energy that was not observed in the records from the hammer source. A “clean” impact is needed to prevent signal cancellation at some frequencies due to destructive interference. The pre-impact motion resulted in significant ground motion prior to the impact of the mass. A time record comparison between the instrumented hammer and the source as collected on a spiked geophone located 2 feet from the source is shown in Figure 4.2.

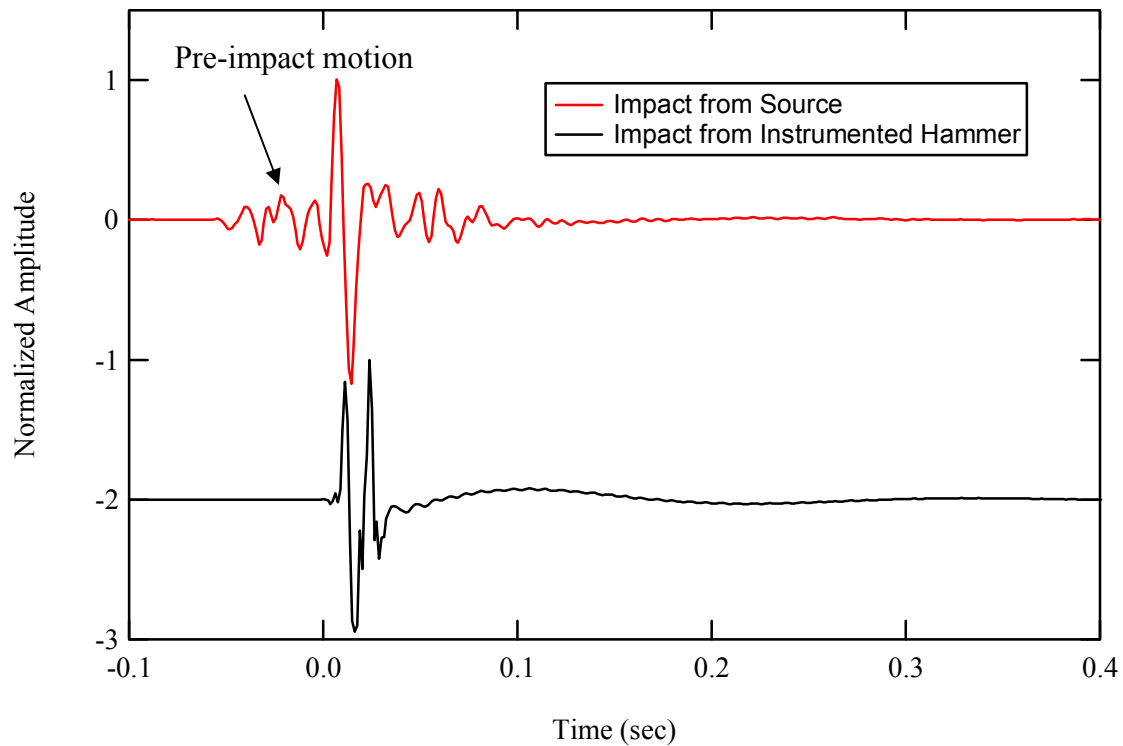


**Figure 4.2 Comparison between recorded motion from the instrumented hammer and source showing pre-impact motion.**

It was determined that the pre-impact motion was a result of a misaligned assembly hole in the bottom cap. The misalignment caused one of the guide rods to “toe in” slightly at the bottom cap resulting in unwanted friction in the guides for the moving mass near the bottom of the stroke. To alleviate this problem the assembly hole was elongated to allow the assembly rod to assume the correct location. Consideration was given to filling in the original hole with epoxy prior to relocating the hole to remove the gap behind the guide rod. Performance was substantially improved once the hole was elongated and it was decided that the epoxy was not required. Time records collected before and after the assembly hole relocation at a 2 foot receiver spacing are shown in Figure 4.3.

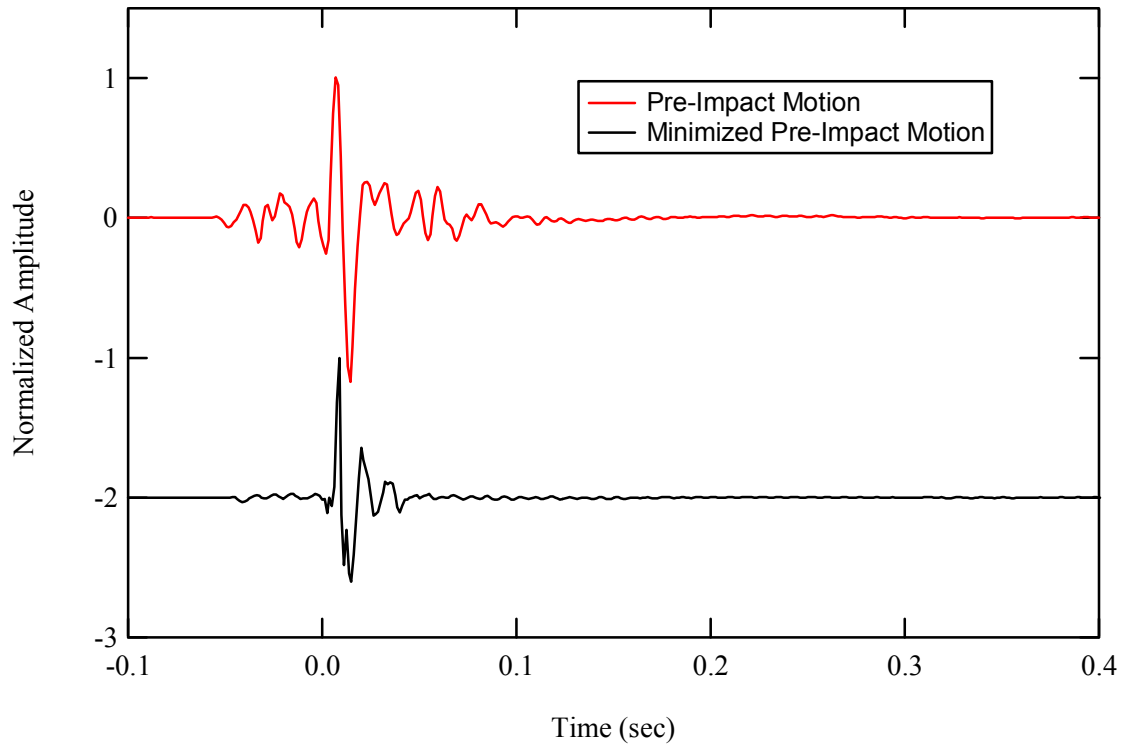


**Figure 4.3 Comparison of time records showing pre-impact motion before and after assembly hole relocation.**

Post-impact energy was also an issue with the source as it was originally constructed. The energy arrived as a second impact at approximately 0.5 seconds after the trigger. Because of the late arrival time, the post-impact energy was attributed to the mass being “reloaded” by the springs. The spring design was such that the mass is just held in the loaded position as to minimize the amount of impact loss. When the source is energized, the mass is pulled to the bottom of the containment cell by the solenoid and held against the bottom cap. When the capacitors have fully discharged, the spring pulls the mass back to the top of the stroke. The impact of the mass against the mounting plate when it reached its loaded position was the source of this energy.

Several solutions were tried to minimize the post impact energy. Installing small pieces of foam between the moving mass and mounting plate was the first solution. Several foam layouts were tried and it was determined that several pieces of 0.25-in. square foam approximately 1.25-in. long were required to meet the damping needs. The foam used had a fairly significant memory resulting in a decrease in cushioning with time if the mass was allowed to sit in a loaded position. The foam in this location also slightly reduced the stroke of the moving mass. Time records comparing performance before and after the foam installation are shown in Figure 4.4.

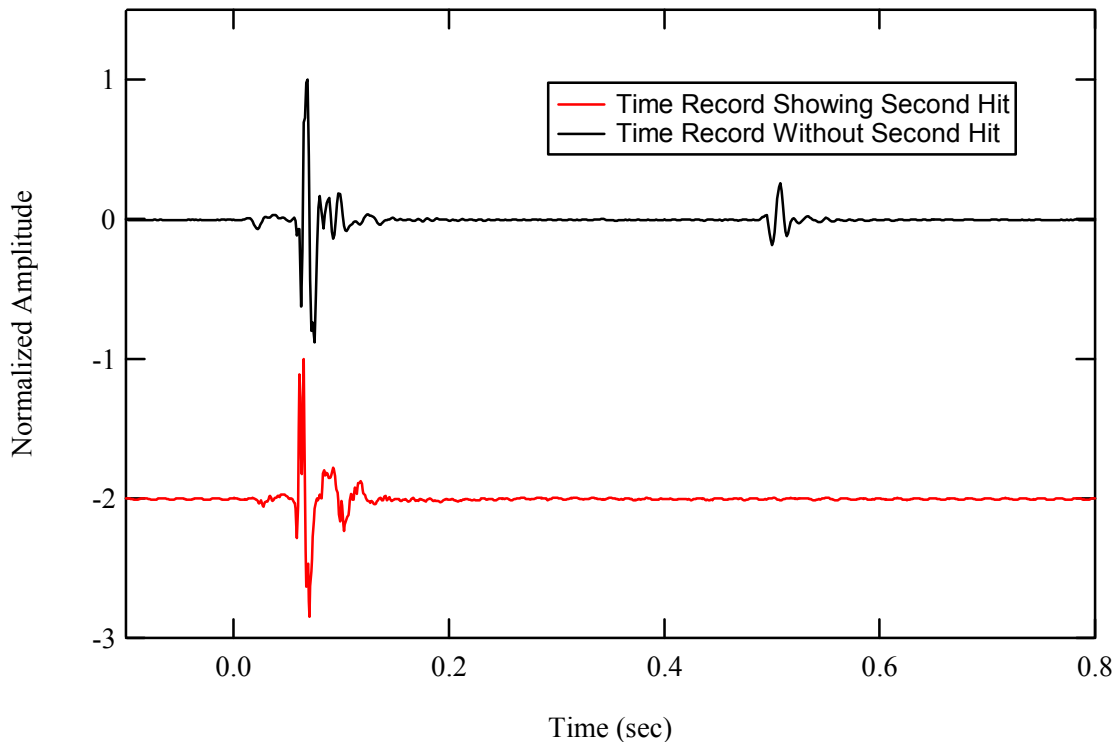


**Figure 4.4 Comparison of time records showing second hit before and after spring buffer installation.**

The second solution involved installing an additional spring on the top cap. This spring was intended to contact the plunger during the reloading stroke and slow it down, minimizing the contact with the mounting plate and reducing the second hit. The spring

was trimmed so the impact stroke would not be reduced. The spring selected has an outside diameter close to that of the plunger and was trimmed to approximately 0.75-in. The spring has a compressed length of 0.25-in. A longer spring could not be used due to space constraints in the containment cell. The spring did not perform as well at eliminating the post-impact energy. To improve the performance of the spring, a hollow foam core was used to improve damping over the limited stroke. The combined spring and foam core assembly performed well, although the foam in the core needs to be removed and expanded regularly to obtain maximum effect. The spring and foam core assembly are shown in Figure 4.5. After modification acceptable repeatability of the source was observed this would make averaging in the time domain possible.

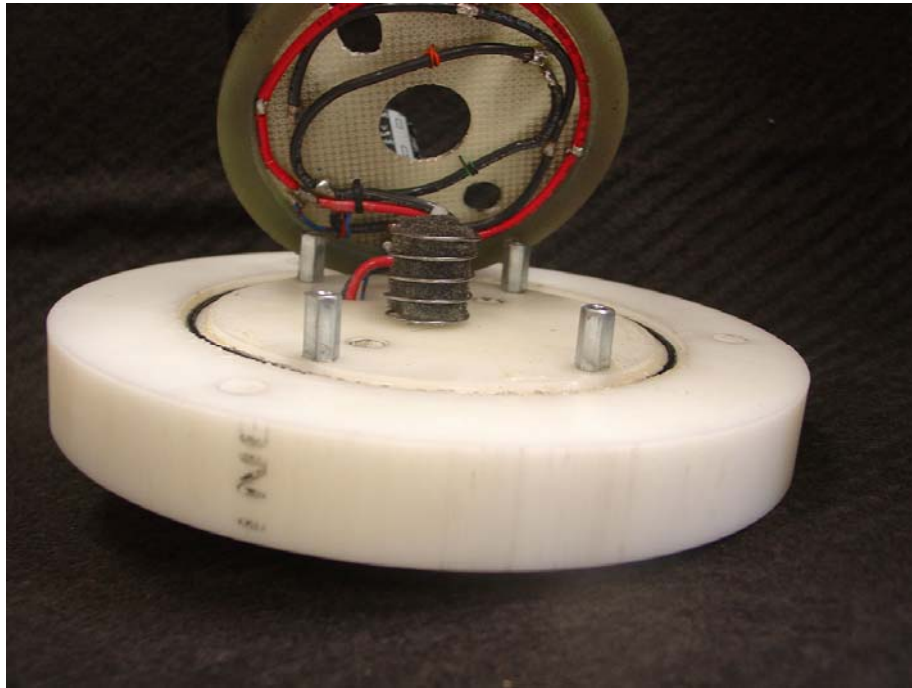


**Figure 4.5** Spring and foam core assembly installed on top cap.

## **4.4 Data Comparison**

### **4.4.1 Time Record Comparison**

Field testing with the source was performed on May 3, 2005 at the Geotechnical Test Facility. Time records were collected at 1-ft. increments out to a distance of 30-ft. from the source to compare the performance of the remote solenoid source to that of the sledge hammer. Comparisons were made in terms of the amplitude and frequency content of the measured waveforms generated from the two sources. Figures 4.6 and 4.7 present the normalized time records recorded at the 30 receiver locations from the hammer source and the solenoid source, respectively. The time delay observed in the data generated from the solenoid source is due to a different triggering system than was used with the hammer source. As discussed in Section 3.3.5 the solenoid source is equipped with an electronic trigger in the control circuit. The repeatability of the trigger signal was checked by placing an accelerometer on the source and measuring the consistency of the delay between the recorded trigger and the actual impact. The trigger was found to be consistent. The instrumented hammer records were triggered at the point of impact by means of an integrated force transducer. In the case of the source, the trigger occurs at the point of initiating the energizing circuit from the control circuit. Because the time record is triggered prior to the actual impact, the delay between when the time recording is initiated and the actual impact is longer.

Comparisons of the recorded time records at receiver locations of 5 ft, 10 ft, 20 ft and 30 ft. are shown in Figures 4.8 through Figure 4.11. The time record from the solenoid source is offset from the zero position in these plots to facilitate the comparison. The time records from the solenoid source and the hammer source shown in these figures

were recorded with the same geophone array and have not been altered or normalized. These comparisons indicate that the recorded amplitudes are generally similar for both sources. The hammer source dropped from a 6-in. height showed slightly higher amplitude levels than were generated with the solenoid source. However, in both cases the signal level was well above the background noise at the site. The records collected from the solenoid impact show additional motion after the surface wave, as compared to the hammer impact. This is likely due to an elastic rebound effect of the source causing a second impact. The affect of this feature on the dispersion data is discussed in Section 4.5.1 and pointed out in Figure 4.9. Comparisons in the frequency domain of the generated signal are presented below.

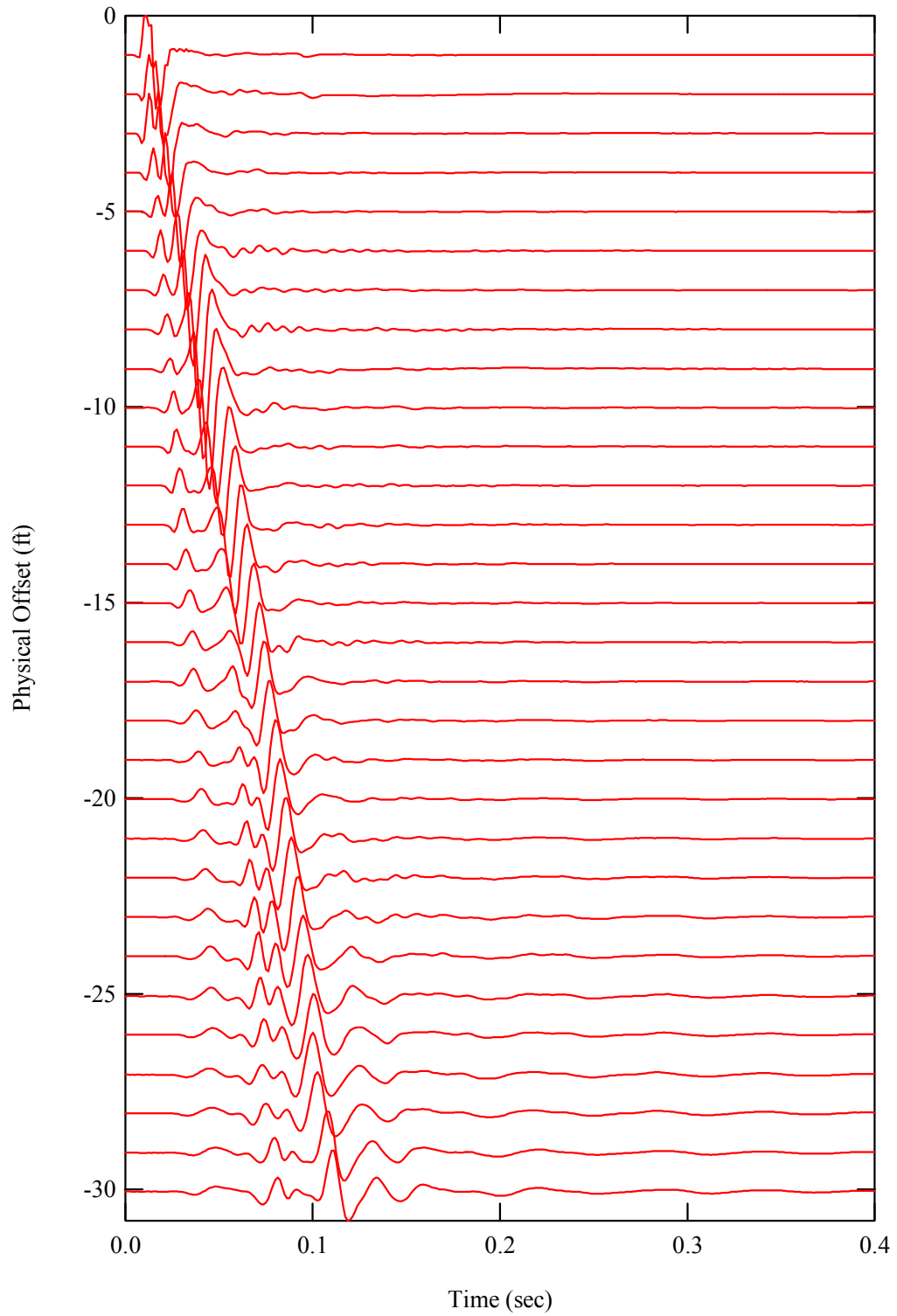


**Figure 4.6** Normalized time records collected at 30 receiver locations from an impact of the hammer source.

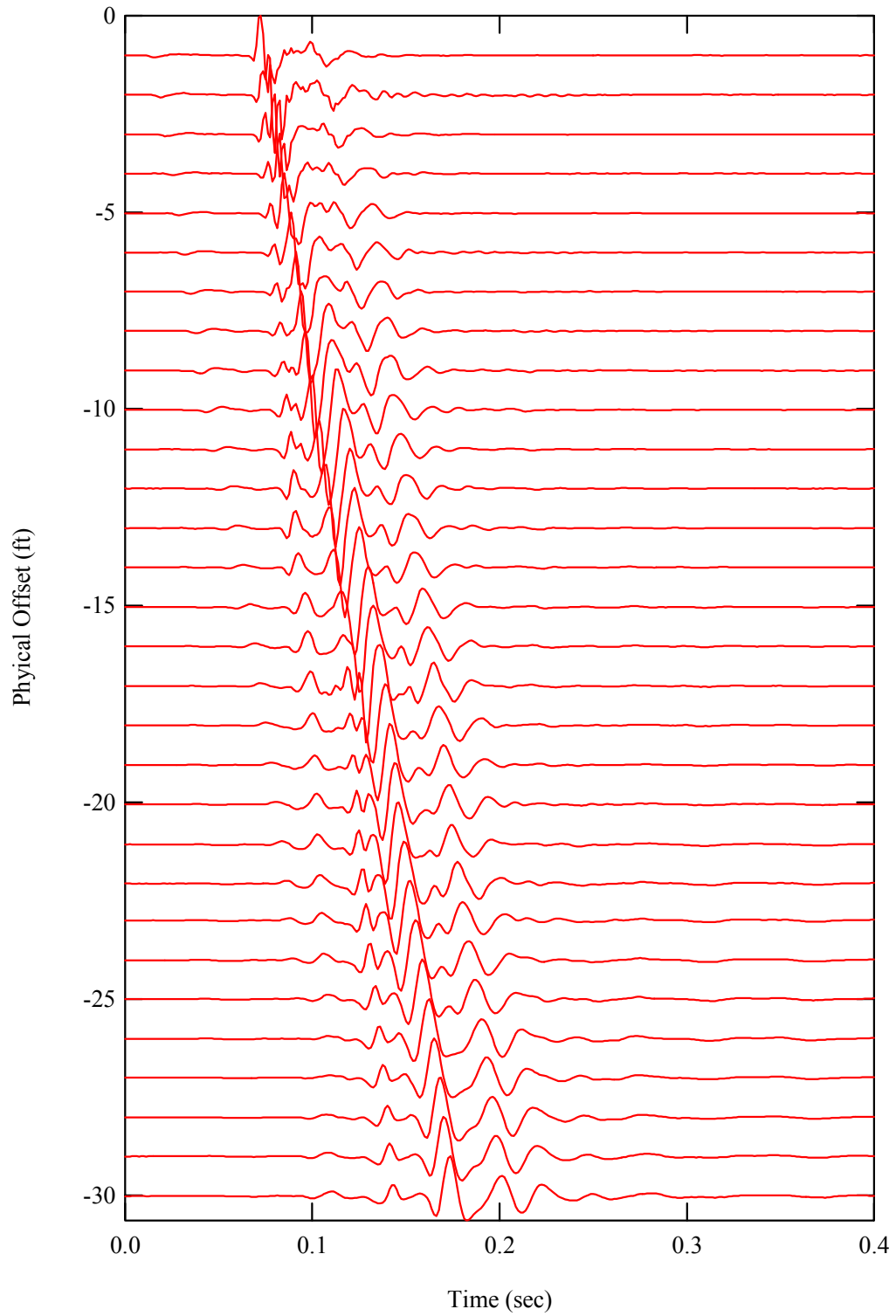


**Figure 4.7** Normalized time records collected at 30 receiver locations from an impact of the solenoid source.

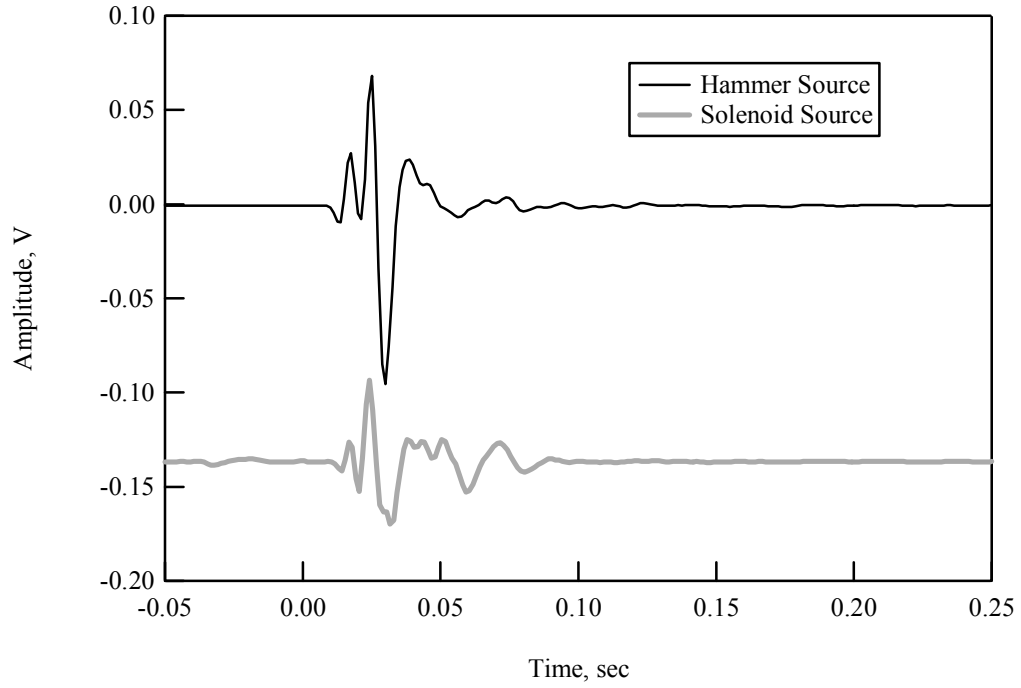


**Figure 4.8** Time record comparison for solenoid and hammer sources at 5 ft from the source location.

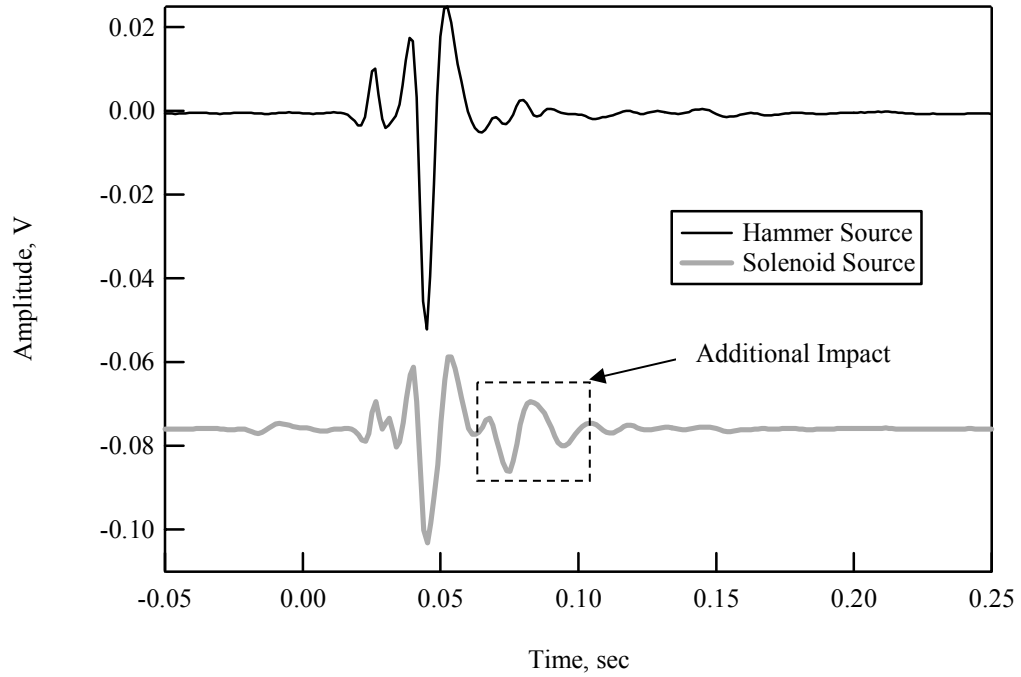


**Figure 4.9** Time record comparison for solenoid and hammer sources at 10 ft from the source location.

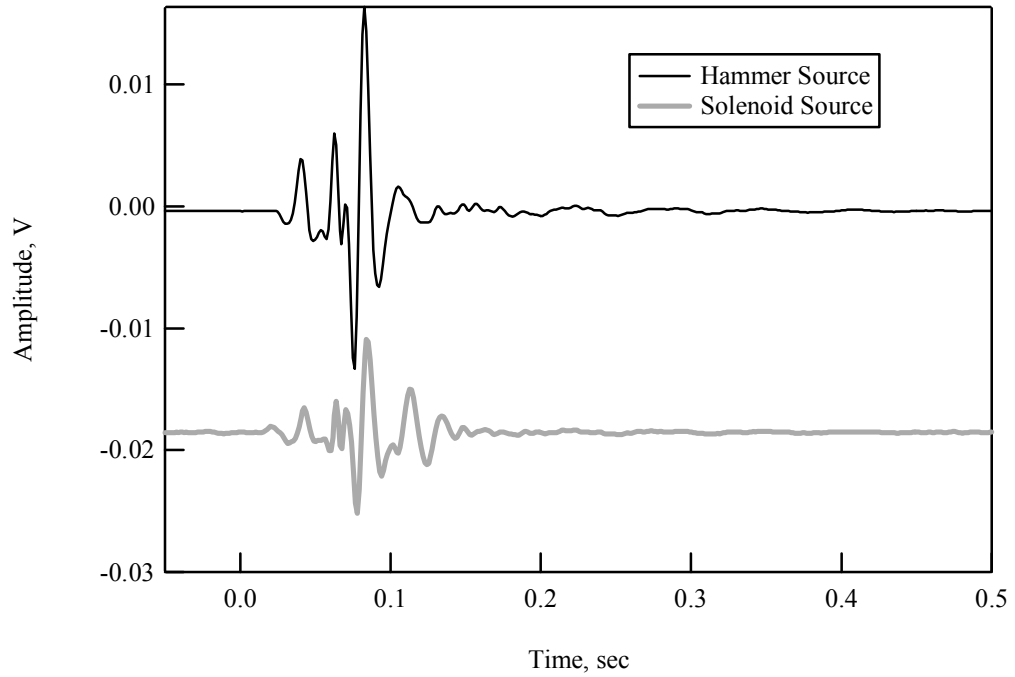


**Figure 4.10** Time record comparison for solenoid and hammer sources at 20 ft from the source location.

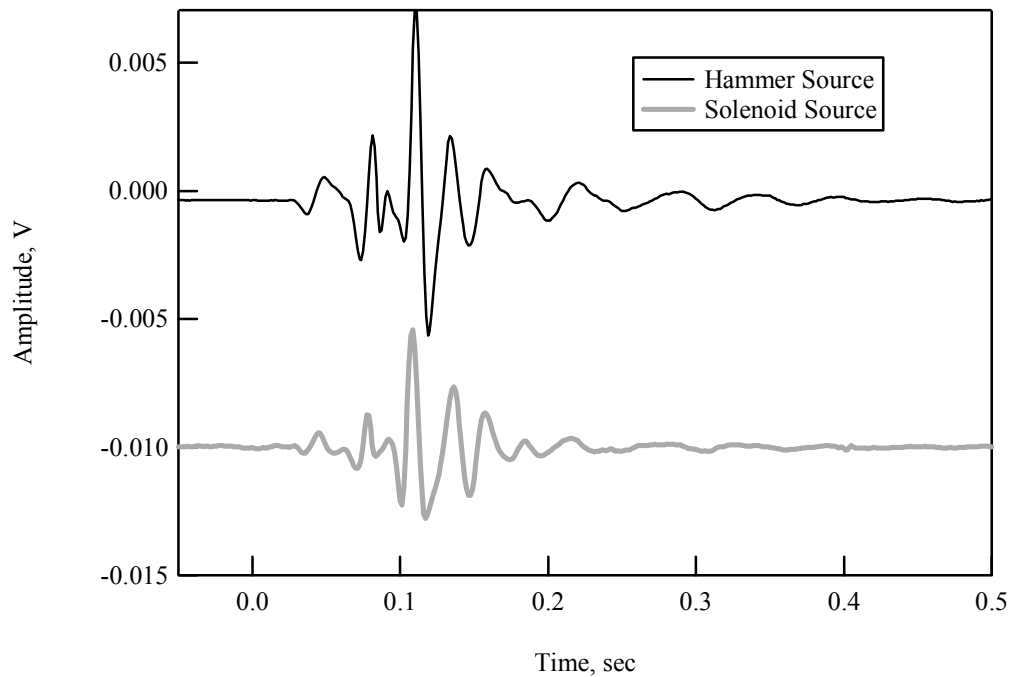


**Figure 4.11** Time record comparison for solenoid and hammer sources at 30 ft from the source location.

#### 4.4.2 Frequency Spectra

The frequency spectra corresponding to the time records at distances of 5, 10, 20, and 30 feet from the source are shown in Figures 4.12 through 4.15. The frequency spectra recorded at the receiver is a function of the source signal, transfer function between the source and receiver, and the receiver response. In this case the receiver locations remained constant so differences between the recorded frequency spectra can be attributed to different source functions. The frequency representation in Figure 4.12 through 4.15 is presented in terms of the power spectra of the received signals.

In general, the power spectra recorded from the impact of both sources compare well. At higher frequencies, the output is slightly greater from the hammer source, however, at low frequencies, the recorded output from both sources is very comparable. The shapes of the frequency spectra are again very consistent with two notable exceptions. First, there are closely spaced oscillations in the frequency spectra measured from the solenoid source that is not present in the hammer source. These oscillations can be attributed to the secondary impact due to the rebound of the mass occurring approximately 0.5 sec after the main impact. Although the magnitude of this effect was reduced, as previously discussed, a small influence remains. This oscillation should not have a negative impact on the surface wave data interpretation. The second issue is the decrease in output at approximately 50 Hz that is observed at each receiver location when the solenoid source is used. Two possible explanations for this decrease in energy in that range are (1) system resonances and (2) closely-spaced double impact. No system resonance was found to be in this frequency range. A more likely explanation is a “double impact” from elastic rebound of the source causing destructive interference in the

50 Hz range which was also observed in the time domain. Future work will need to be performed to identify a solution to this problem.

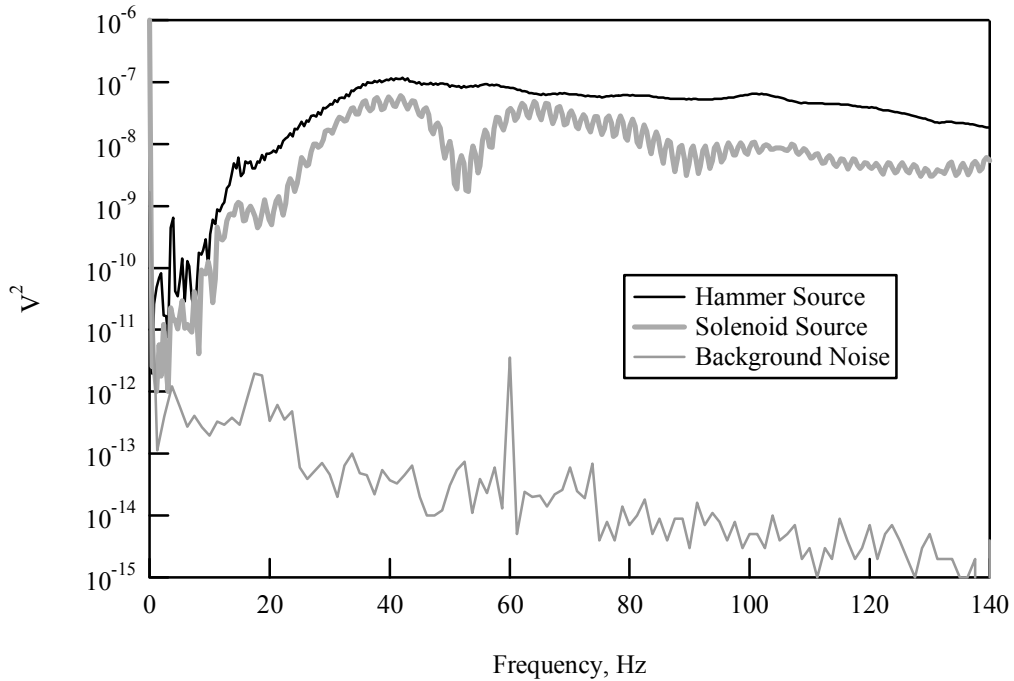


**Figure 4.12** Power spectra comparison for solenoid source and hammer source for 5 ft spacing.

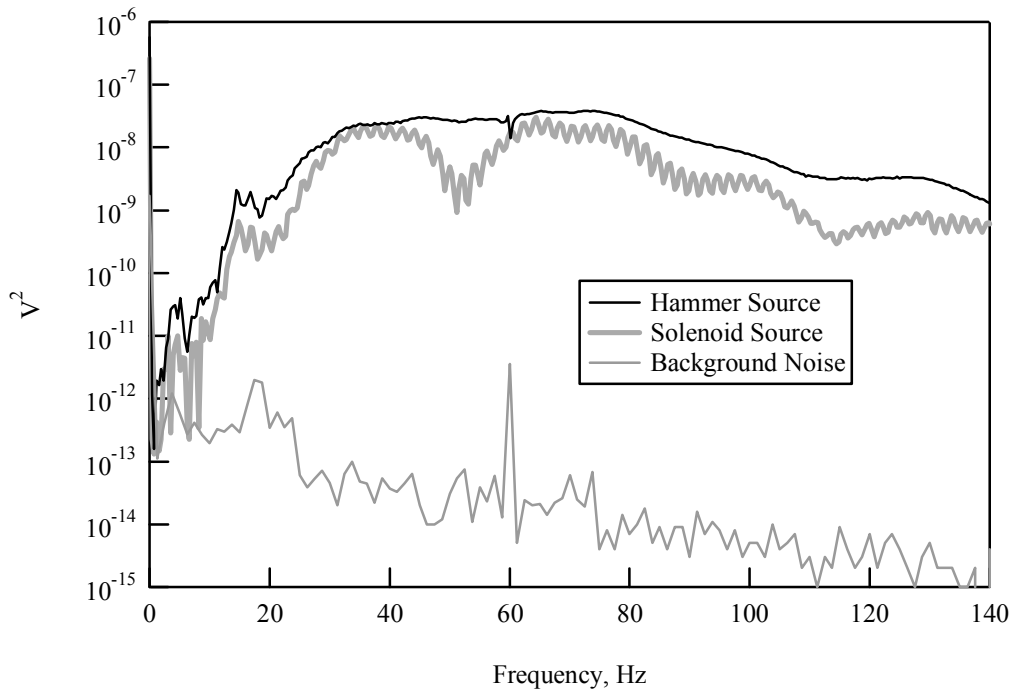


**Figure 4.13** Power spectra comparison for solenoid source and hammer source for 10 ft spacing.

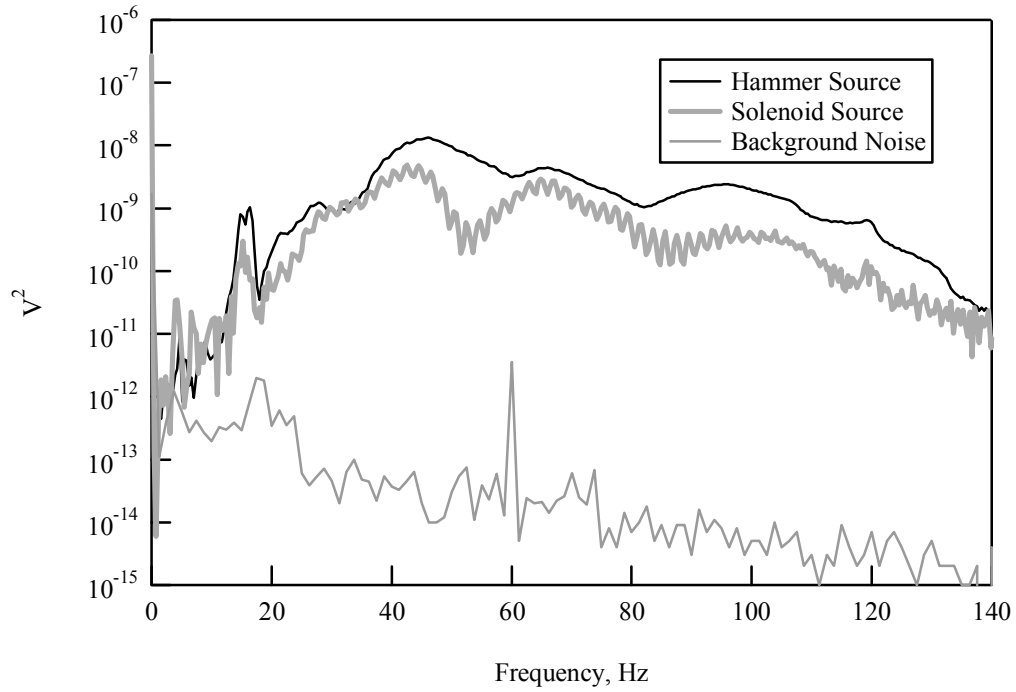


**Figure 4.14** Power spectra comparison for solenoid source and hammer source for 20 ft spacing.

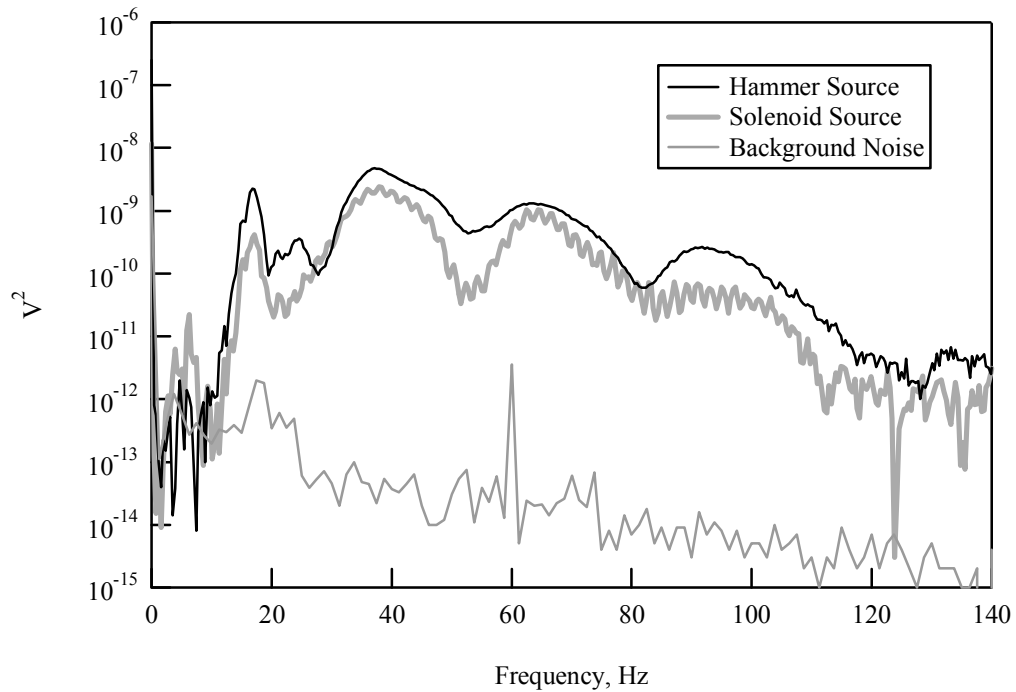


**Figure 4.15** Power spectra comparison for solenoid source and hammer source for 30 ft spacing.

## **4.5 Comparison of Processed Data**

The source was next evaluated by collecting and processing data using the two common methodologies used in geotechnical engineering, the Spectral-Analysis-of – Surface Waves (SASW) and multi-channel wavefield transformation. The processed data generated from the hammer source and the remote source are compared and discussed for both methodologies.

### **4.5.1 SASW Processing**

Spectral-Analysis-of-Surface-Wave processing was performed on data collected on May 3, 2005 at the Geotechnical Research Facility. The source and instrumented hammer were used to record SASW data at receiver spacings of 2, 4, 8, 16, and 25 feet. This resulted in a maximum receiver distance of 50 feet from the source. The SASW measurements with each source were not performed at the same time, so the receivers had to be reset. Although the same receivers were used, small differences in the phase plots may have occurred due to changes in receiver coupling associated with resetting the receivers. Wrapped phase plots calculated from the cross power spectrum between receiver pairs are shown for each of the receiver pair spacings in Figure 4.16. In general, the phase plots compared well with only minor differences. The solenoid source produced very good results for all receiver pair spacings with the exception of the longest receiver pair spacing of 25 ft, where the quality of the data was noticeable poorer.

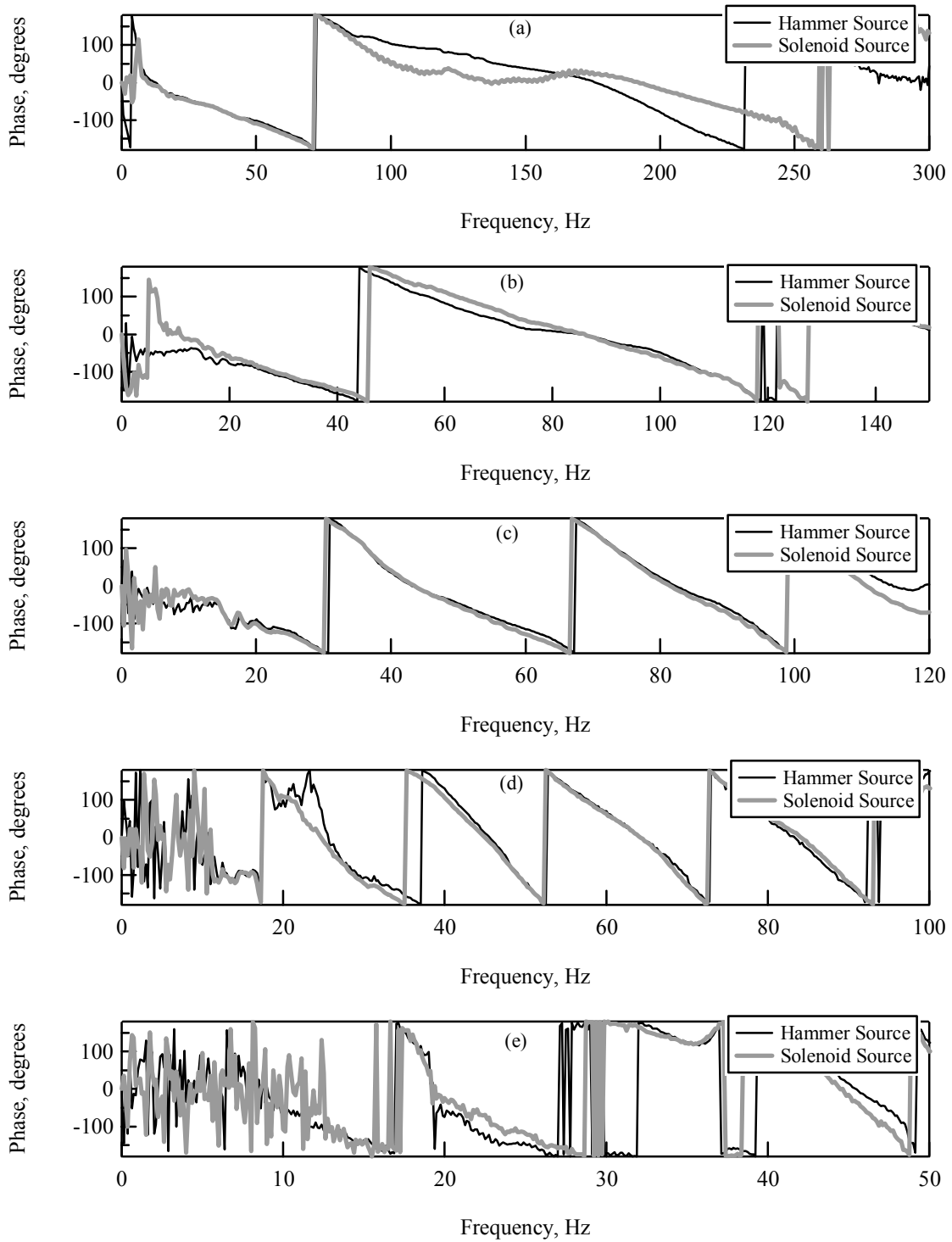
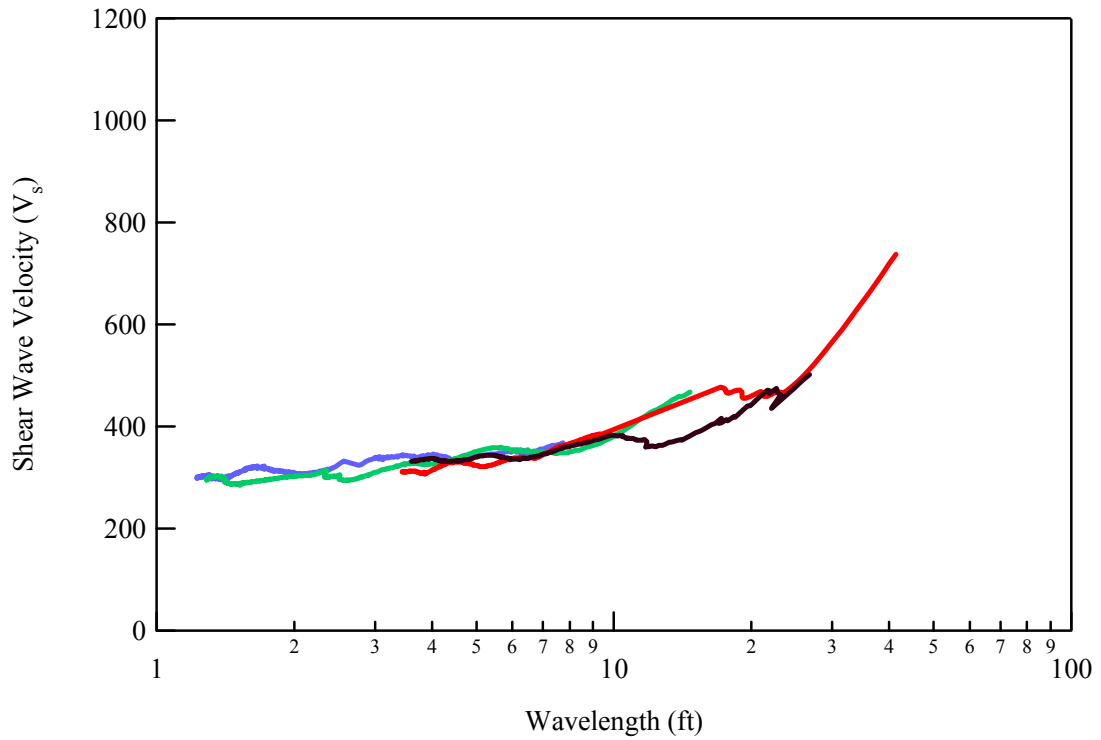


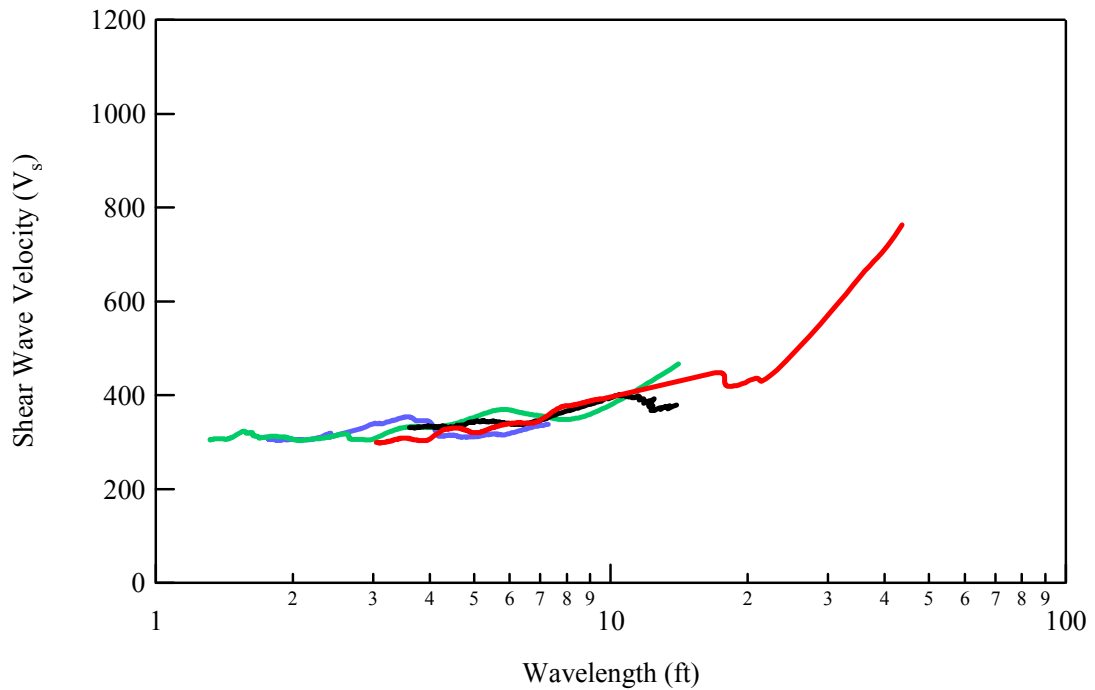
**Figure 4.16** Comparison of phase plots generated from different sources at five receiver pair locations of (a) 2ft-4ft (b) 4ft-8ft, (c) 8ft-16ft, (d) 16ft-32ft, and (e) 25ft-50ft.

Dispersion curves were generated from the phase information for both the solenoid source and hammer. All five of the receiver pair spacings used in the data collection were used to develop the experimental dispersion curves. The experimental dispersion curves generated from SASW testing using the solenoid source and sledge hammer source are compared in Figure 4.17. In general, the dispersion plots are very consistent. In both cases, dispersion data was generated over a wavelength range of approximately 1 ft to over 40 ft. Dispersion data in this wavelength range can be used to generate a shear wave velocity profile to a depth of approximately 15 to 20 ft.

Forward modeling analysis of the surface wave data was not performed as part of this study since the objective of this study was to compare the performance of the new solenoid source with a conventional on-land source. In addition, sufficient ground truth at the site is not yet available for comparison purposes. However, initial drilling at the site has indicated a complex stratigraphy with stiff layers overlying soft layers, as shown in Figure 4.18. This complex stratigraphy is consistent with the observed dispersion data in Figure 4.17 with non-overlapping segments from adjacent receiver spacings.



**(a) Experimental dispersion curve collected using the solenoid source.**



**(b) Experimental dispersion curve collected using the sledge hammer.**

**Figure 4.17 Comparison of experimental dispersion curves for the (a) solenoid source and (b) sledge hammer.**

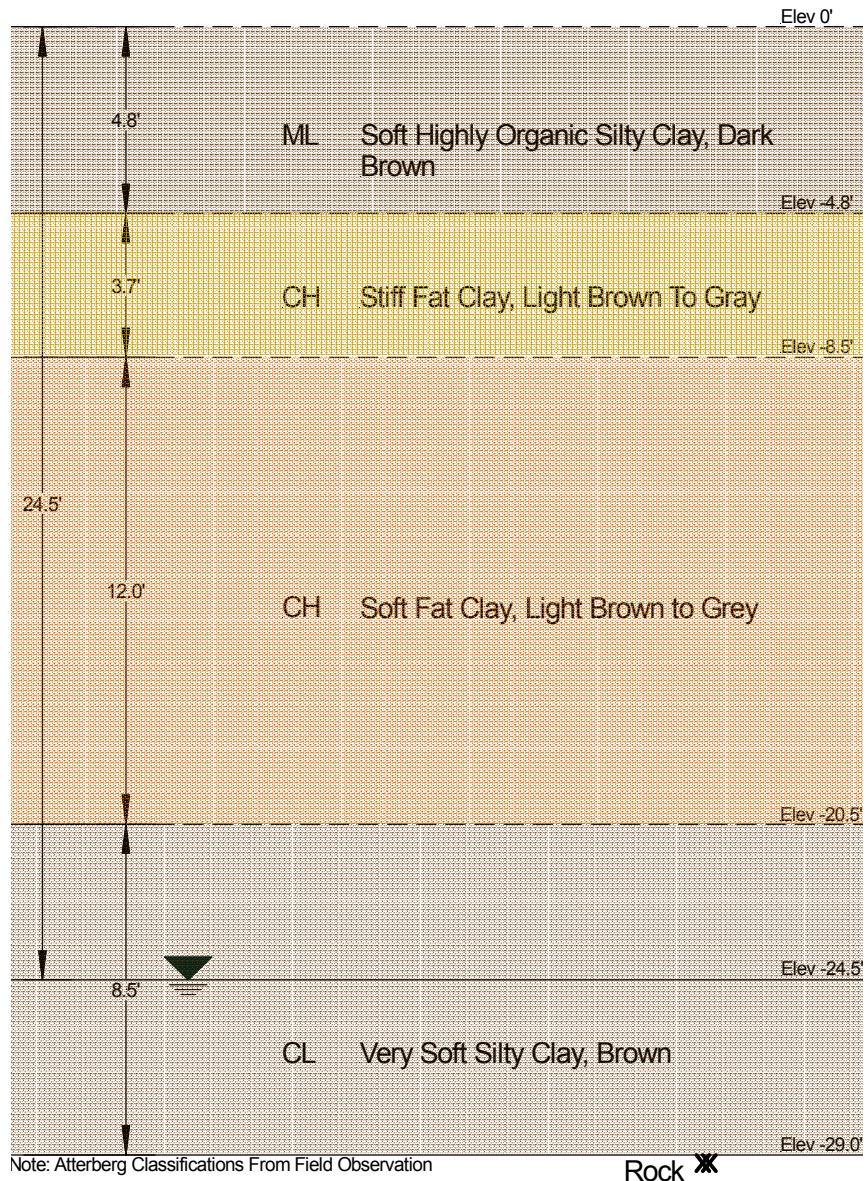


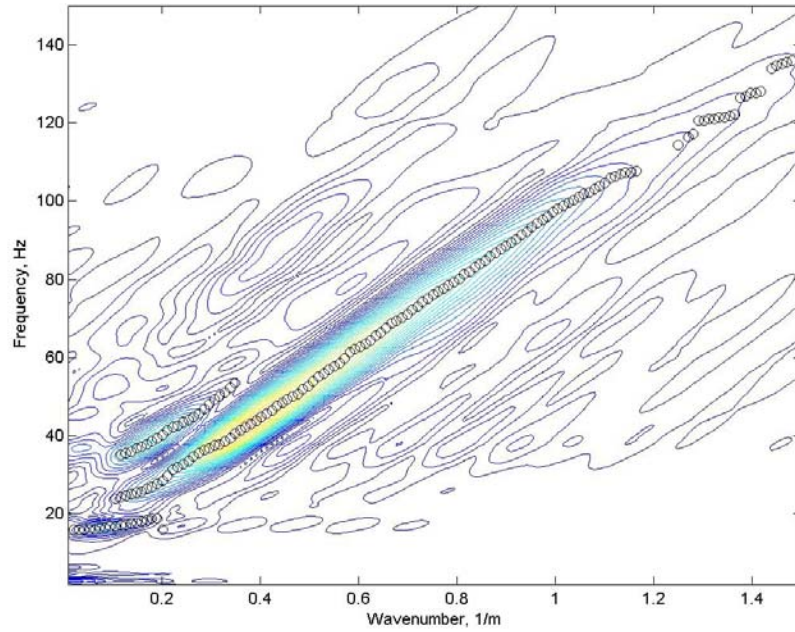
**Figure 4.18 Profile from drilling performed at the Geotechnical Research Facility at Midway on April 20, 2005.**

#### 4.5.2 Multi-Channel Processing

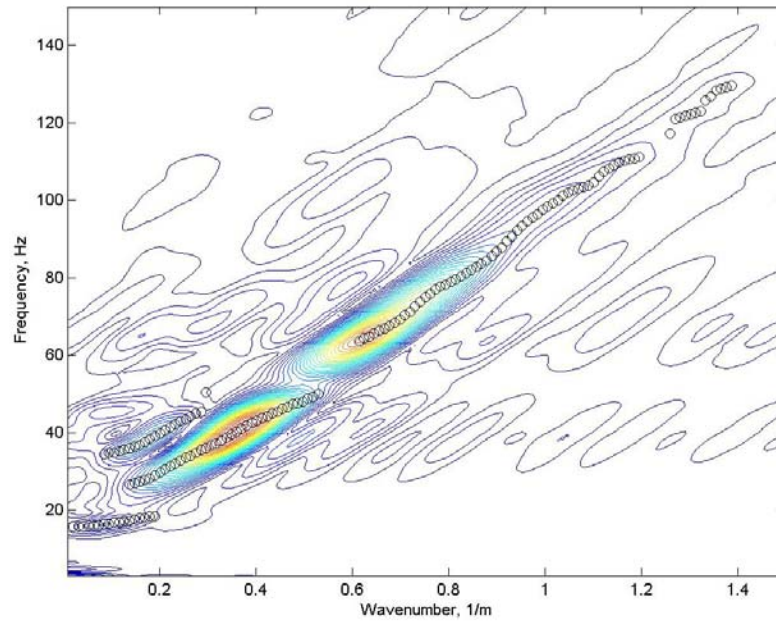
Processing of multi-channel data using a wavefield transformation method was also performed on the data collected at the Midway site. Multi-channel processing was performed by collecting thirty time records located at 1-ft intervals from the source. Figures 4.6 and 4.7 present the time records collected using the hammer source and the

solenoid source, respectively. The dispersive nature of the surface wave can be clearly seen as the receiver location offset distance from the source increases.

A two-dimensional Fourier transform was used to produce a frequency-wave number (f-k) map from data generated with each source. The advantage of this method is that the f-k map can be used to identify separate modes of wave propagation. Typically, only the fundamental mode is used in the inversion process. The f-k maps for the data generated using the hammer source and the solenoid source are shown in Figure 4.19a and 4.19b, respectively. The peak of the contours in the plots identifies the wave propagation modes. In general, the trends in the f-k plots are similar with multiple modes apparent in the f-k plots from both sources. However, the f-k map generated from the solenoid source data exhibits a distortion at a frequency of approximately 50 Hz. This distortion is consistent with the void in energy observed at approximately 50 Hz as discussed in Section 4.4.2. Figure 4.20 presents a comparison of the mode shapes generated from the f-k plots for each source. Apart from the deviation at 50 Hz, the same information is generated from both sources.



(a) Frequency-wave number map (f-k) generated with the hammer source.



(b) Frequency-wave number map (f-k) generated with the solenoid source.

**Figure 4.19** Comparison of frequency-wave number contour plots generated from multi-channel analysis of surface waves for the (a) hammer source and (b) solenoid source

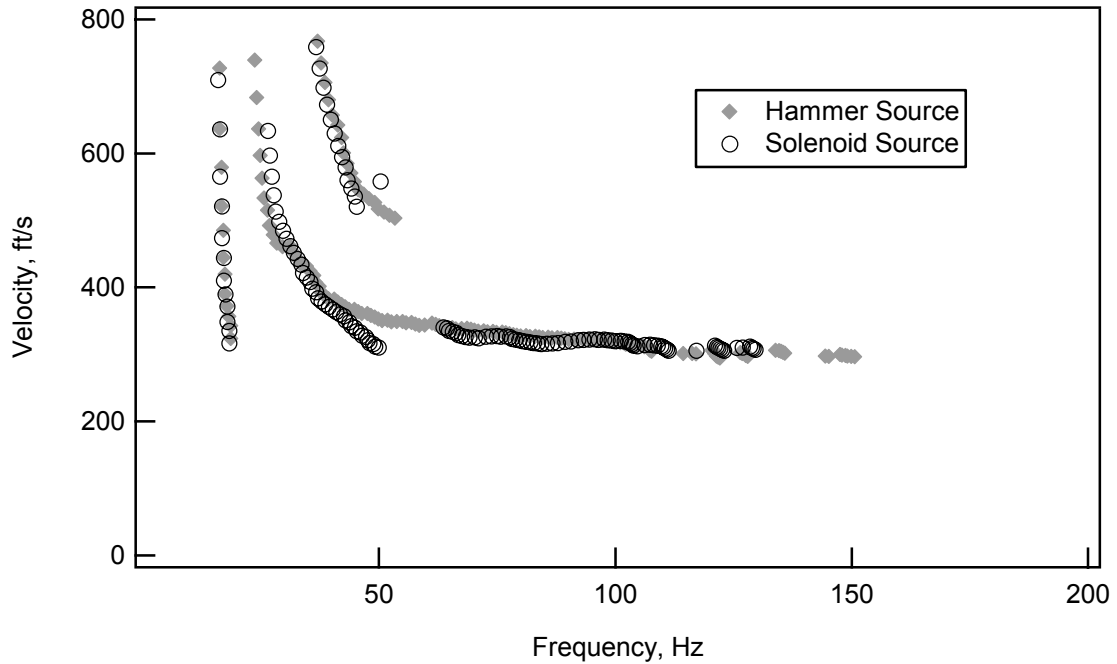


**Figure 4.20 Modes Identified from f-k plots shown in Figure 4.19**

## 4.6 Summary

The on land testing resulted in valuable information for evaluating the source performance with respect to the baseline of the sledge hammer source. The solenoid source performed similarly to the sledge hammer in most facets examined with a few differences. The major differences identified were (1) the solenoid source generated less overall energy than the target source and (2) the solenoid source exhibited a substantial decrease in energy at approximately 50 Hz.

Despite this differences, measurements made with the solenoid source produced dispersion curves generated using the SASW methodology that were consistent with the dispersion curves generated with the hammer source. In addition, 2-D Fourier transforms of the multi-channel data produced similar f-k plots with the exception of the previously noted distortion at approximately 50 Hz. Dispersion modes calculated from the f-k plots were also consistent between the two sources.

## **CHAPTER 5. UNDERWATER TESTING**

### **5.1 Introduction**

The primary objective of the underwater testing was to evaluate the performance of the solenoid source at a submerged, soft soil site. This was done by collecting time records excited by the solenoid source and measured with geophones placed directly on the soft soil at a shallow underwater site. The resulting data was processed using conventional surface wave methods used in geotechnical engineering. A secondary objective was to perform a preliminary study to assess the feasibility of performing the surface wave measurements using non-contacting instrumentation. Surface wave data measured using directly coupled geophone receivers are compared to data measured using non-contacting hydrophone receivers in the water column.

### **5.2 Underwater Testing Procedure**

#### **5.2.1 Location**

Underwater testing was performed at the Bradford Farms Research Facility operated by the College of Agriculture at the University of Missouri-Columbia. The facility is located on Rangeline Road approximately 5 miles south of Interstate 70 in Boone County Missouri. The pond is a man-made impoundment created for crop irrigation purposes. Underwater testing was performed in April and May of 2005 in approximately 3-ft deep water. A photograph of the pond used for the underwater testing is shown in Figure 5.1.



**Figure 5.1** Photograph of pond at Bradford Farms Research Facility.

### **5.2.2 Instrumentation Used**

The instrumentation required for underwater testing included 4.5-Hz geophones encased in a waterproof epoxy (as discussed in Section 3.4.1) for measuring particle velocity at the soil surface as well as 6-Hz hydrophones for measuring hydro-dynamic pressures generated in the water column. Both sets of instrumentation were manufactured by Geospace LP. The solenoid source developed for this study was used for all underwater testing. Data collection was performed with a Hewlett Packard 3562A dynamic signal analyzer and recorded on a laptop computer.

### **5.2.3 Field Testing Procedure**

The testing procedure employed at the underwater site was similar to the procedures used on land, as discussed in Chapter 4. The source location was maintained and a “walk away” receiver array was used. Time records were collected at 2-ft intervals out to an offset of 30 ft. from the source. For SASW testing the spacing between receiver pairs ranged from 2 ft. to 20 ft., meaning the maximum receiver offset was 40 ft from the

source. The use of a two-channel data acquisition system necessitated collected time records by attaching a geophone pair and a suspended hydrophone pair to the deployment frame at a fixed 2 ft. interval and moving the frame 4 ft. per impact. Underwater time records were collected with both geophones located directly on the sediment and hydrophones suspended in the water column approximately 1 in. above the surface at the same location as the geophones. The source was set in a vertical orientation and checked periodically to insure that the orientation had not changed.

### **5.3 Underwater Testing with Contacting Receivers**

#### **5.3.1 Time Records**

The normalized time records collected at 2 ft. intervals using the geophone receivers directly coupled to the sediment are shown in Figure 5.2. The time records were collected at 2 ft. intervals instead of 1 ft. intervals (as was done on land) due to the difficulty in placing the receivers underwater. The quality of the time records is generally good, although 60-Hz electrical noise was evident on some of the records. It should be noted that attempts to minimize the noise were made through the use of differential inputs on the recording equipment and the use of twisted and shielded pairs geophone cable.

One of the main differences observed in these records compared to the on-land data is the early acoustic wave arrival traveling through the water. The Scholte-type surface wave arrives later and is clearly separated from the acoustic wave as the receiver spacing increases. The dispersive nature of the Scholte wave is also evident in these time records as indicated by the spreading of the energy at larger receiver offsets.

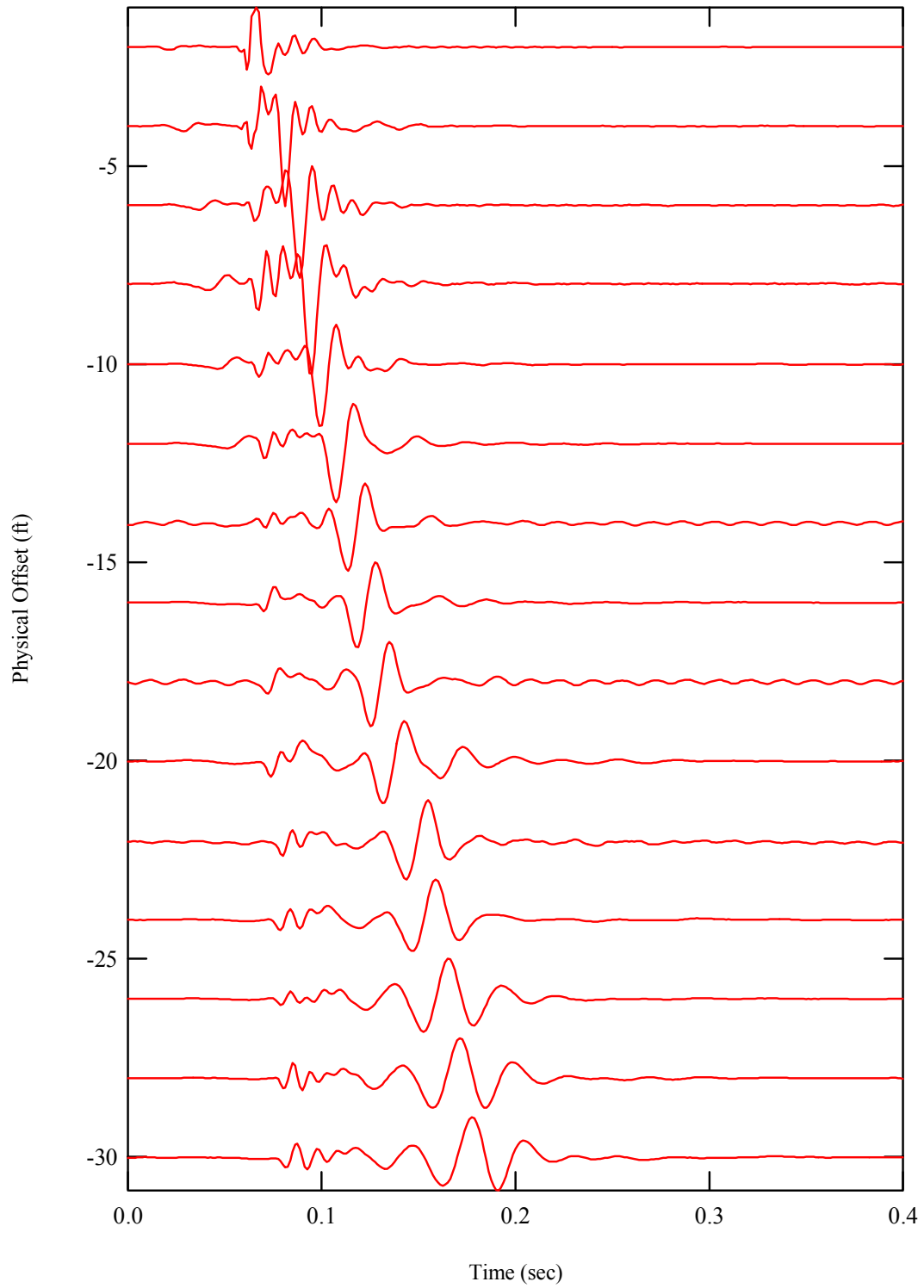


**Figure 5.2** Offset time records collected with the solenoid source and underwater geophones.

### 5.3.2 SASW Data Processing

Surface wave data collected at the Bradford Farms Research Facility on May 19, 2005 were used to generate a phase velocity dispersion curve using the SASW method. The solenoid source and geophone receivers were used to measure ground motions at receiver pair spacings of 2, 4, 8, 12, and 20-ft. (The longest spacing was reduced for the underwater testing based on the poor data collected at the 25 ft spacing on land). This resulted in a maximum receiver offset from the source of 40 ft. The wrapped phase plots calculated from the cross-power spectrum between the receiver pairs are shown in Figure 5.3 a through e.

The measured phase plots were used to develop a phase velocity dispersion curve for the site, as described in Chapter 2. Portions of the phase plots that were not used in the analyses are indicated by the shaded regions in Figure 5.3. The dispersion curve for this site is shown in Figure 5.4. The shortest usable wavelength recorded using the solenoid source and geophones was approximately 1.5 ft. This is slightly longer than the on-land case, possibly due to the source footprint being larger in the softer sediment. The longest usable wavelength generated by the source was 35 ft. Dispersion data in this wavelength range can typically be used to generate shear wave velocity profiles with resolution from the top foot down to approximately 15 ft. As in the on-land case, the dispersion curve showed several regions where the dispersion data did not overlap between adjacent receiver pairs. This is indicative of a complex stiffness profile where multiple surface wave modes are propagating.

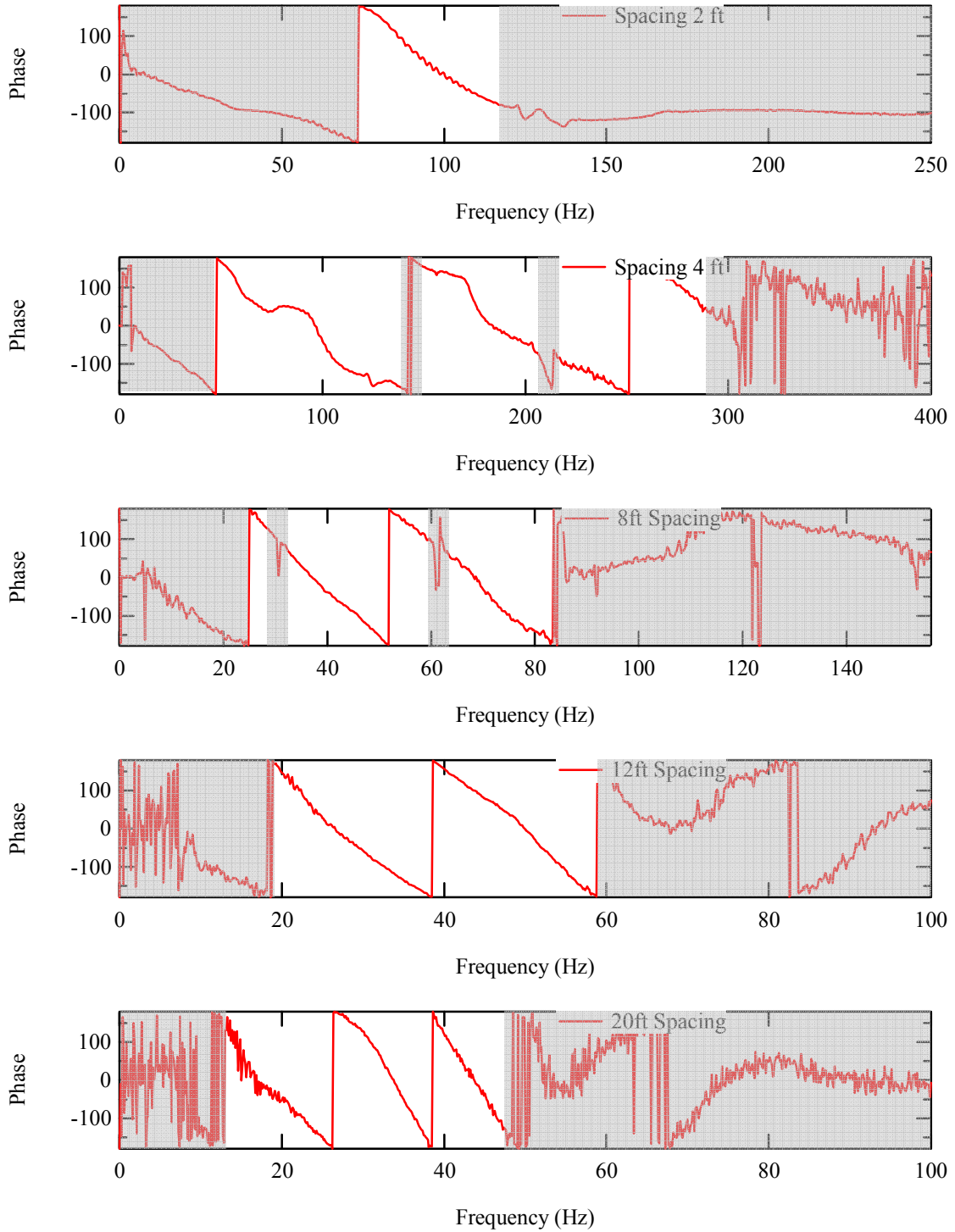


**Figure 5.3** Wrapped phase plots measured from SASW testing performed with the solenoid source and geophones.

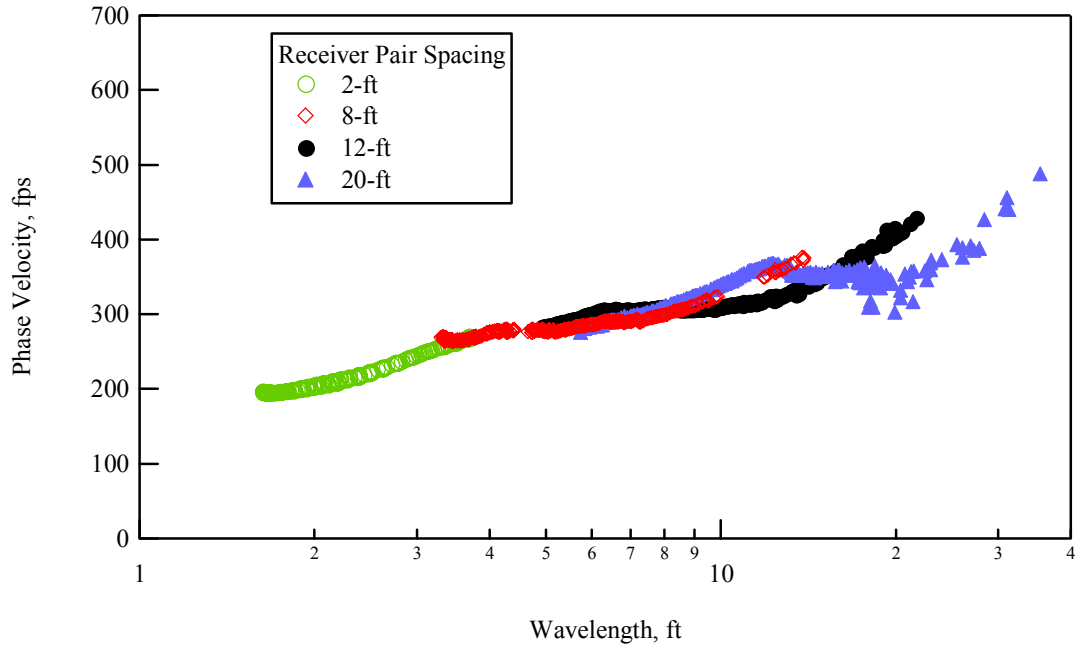


**Figure 5.4 Dispersion curve generated from underwater SASW testing with the solenoid source and geophones.**

### 5.3.3 Multi-Channel Processed Data

The offset time records shown in Figure 5.2 were used to perform multi-channel analysis of the site using a 2-D Fourier transform, as was performed with the on-land data. The frequency-wave number map for the solenoid/geophone measurements at the Bradford Farms site is shown in Figure 5.5. The energy void at 50 Hz that was evident in the on-land case is not as apparent in this f-k plot. There are at least two clear propagation modes shown in Figure 5.5 for the underwater data. The two modal dispersion curves generated from the f-k plot are shown in Figure 5.6. The highest frequency resolved in the underwater case was 80 Hz, compared with approximately 140 Hz for the on-land case. This is possible due to higher damping levels in the softer underwater sediments. Better near surface resolution would require closer spaced receiver intervals.

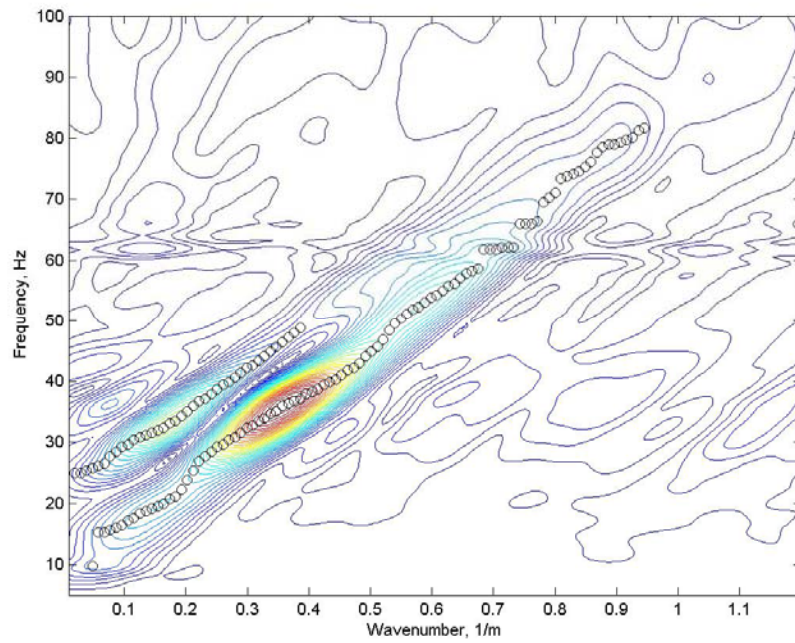


**Figure 5.5** Frequency-wave number plot for underwater data collected with the source and geophones.

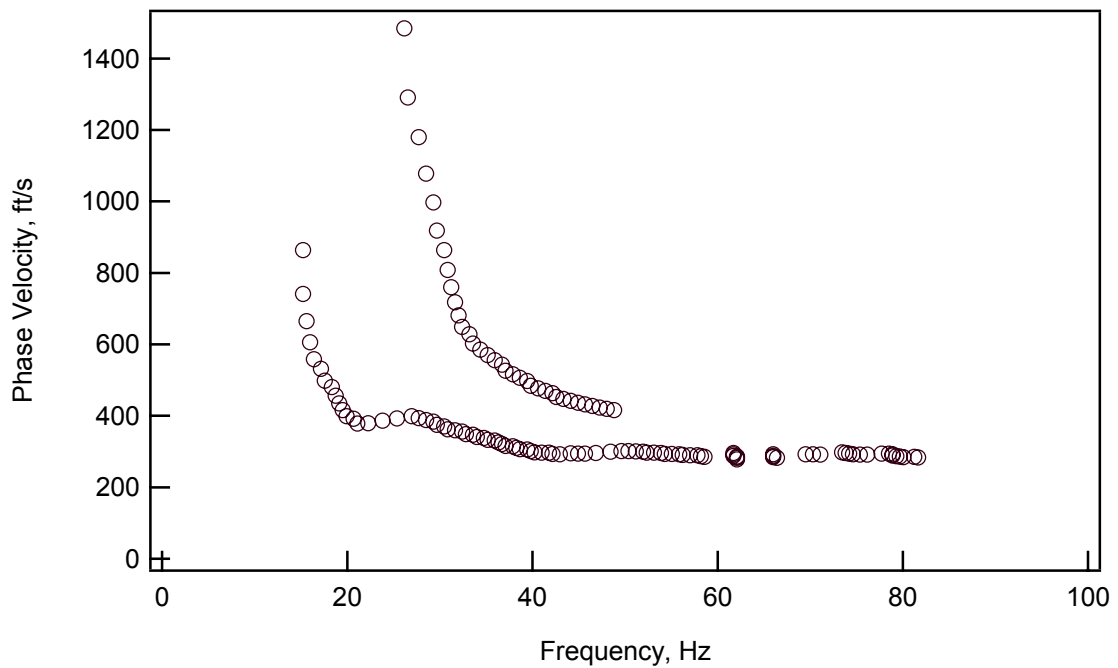


**Figure 5.6** Dispersion modes calculated from the f-k plot shown in Figure 5.5.

## **5.4 Underwater Testing with Non-Contacting Receivers**

Measurements were next performed using the same experimental set-up described above except the data was recorded using non-contacting hydrophone receivers. The objective of these measurements was to assess the feasibility of performing surface wave velocity measurements underwater using non-contacting instrumentation.

### **5.4.1 Time Records**

Figure 5.7 presents the time records recorded using the non-contacting hydrophone receivers and the solenoid source. As with the data collected using the geophones, both an acoustic wave arrival and the Scholte wave arrival are clearly evident at large receiver offsets. In the case of the hydrophone data, however, the acoustic arrival has a larger relative amplitude than the Scholte wave arrival. Unfortunately, 60 Hz electrical noise is evident in all of the measurements due to poor shielding on the hydrophone cables. Even with the electrical noise, the Scholte wave arrival is clearly recorded using the non-contacting instrumentation. Figure 5.8 presents a comparison between the geophone measurement and the hydrophone measurement recorded at 30 ft from the solenoid source. The phase difference between the time records is expected due to the nature of the instrumentation. The hydrophone transducers produce an output proportional to the pressure generated in the water and geophones produce an output proportional to particle velocity phase shift.

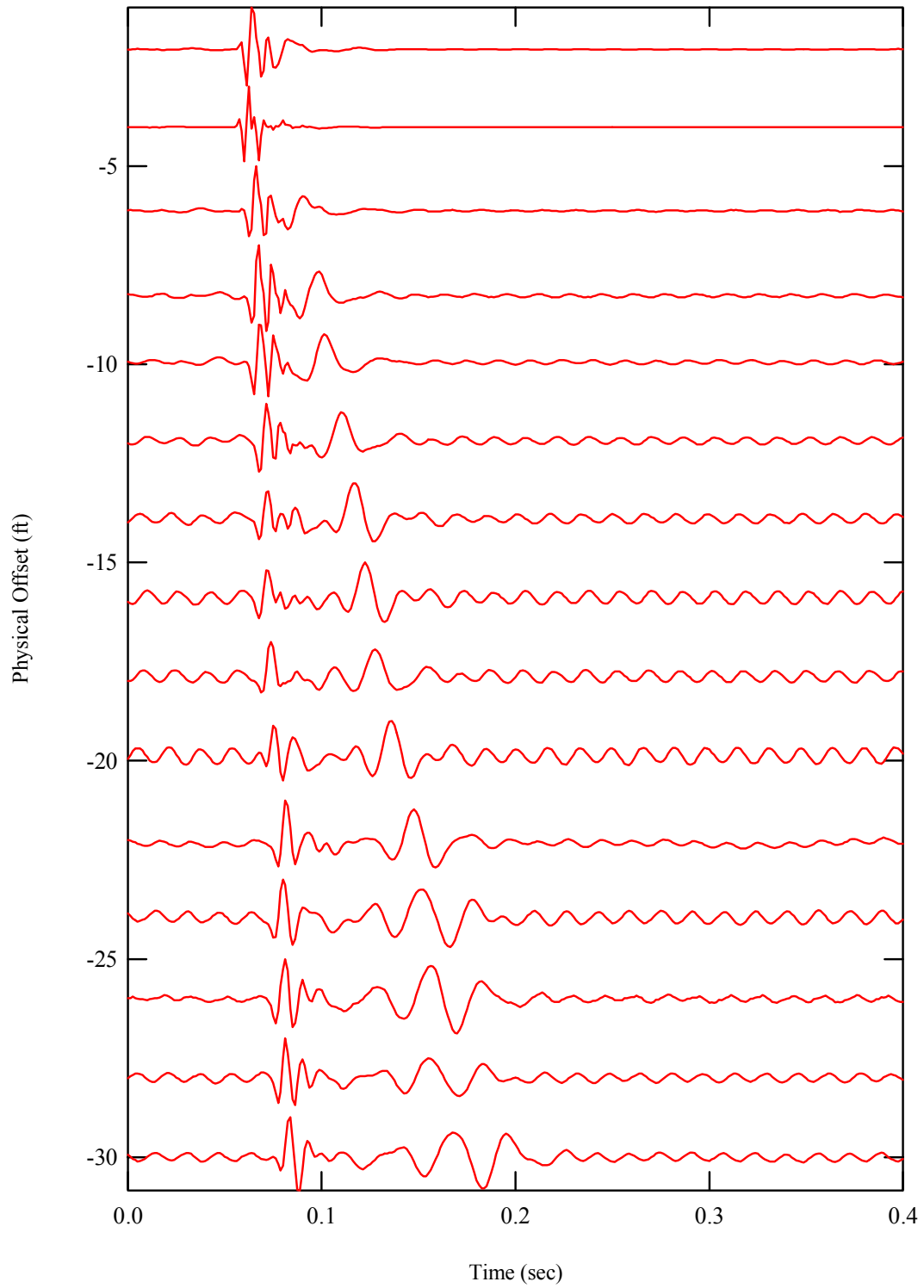


**Figure 5.7** Offset time records collected with the solenoid source and suspended hydrophones.

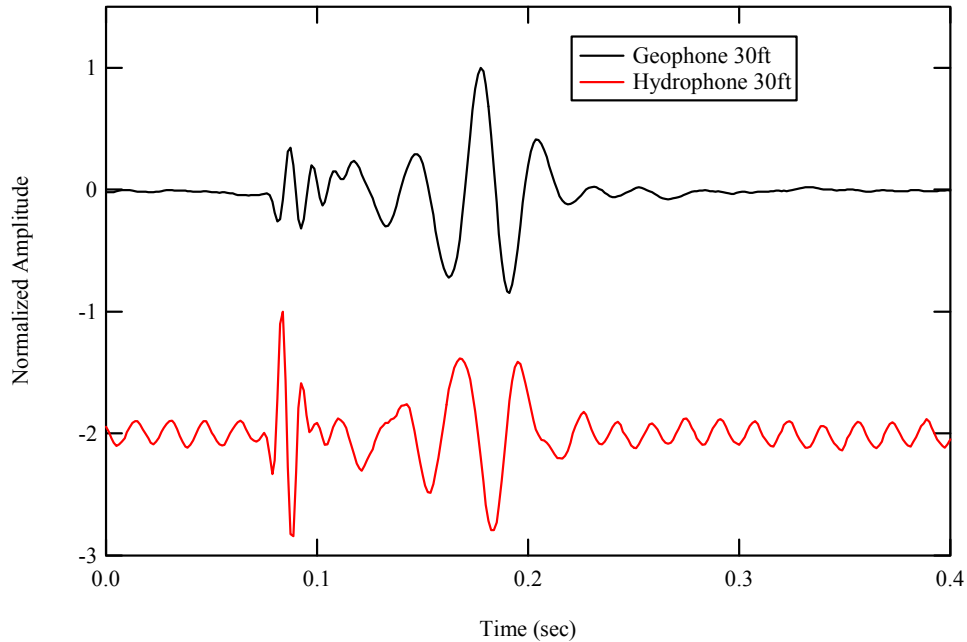


**Figure 5.8** Time record comparison for geophone and suspended hydrophone using the solenoid source at a 30 ft spacing.

#### 5.4.3 SASW Processed Data

SASW testing was performed with hydrophone receivers at the same locations as the measurements made with the geophone receivers. The wrapped phase plots calculated between hydrophone receiver pairs are compared to the phase measured with the geophone receivers in Figure 5.9. At short receiver spacings (close to the source) the phase plots do not compare well with the geophone data. One reason for this is the phase velocity of the acoustic wave is superimposed with the Scholte wave in these plots resulting in a distorted phase plot. Near the source where the acoustic arrival is larger relative to the Scholte wave the effect is greater. At the receiver pair spacings of 8 and 12 ft the hydrophone and geophone phase plots compare well over portions of the recorded frequency range. At the longest spacing of 20 ft, the phase plots from the hydrophone were not interpretable.

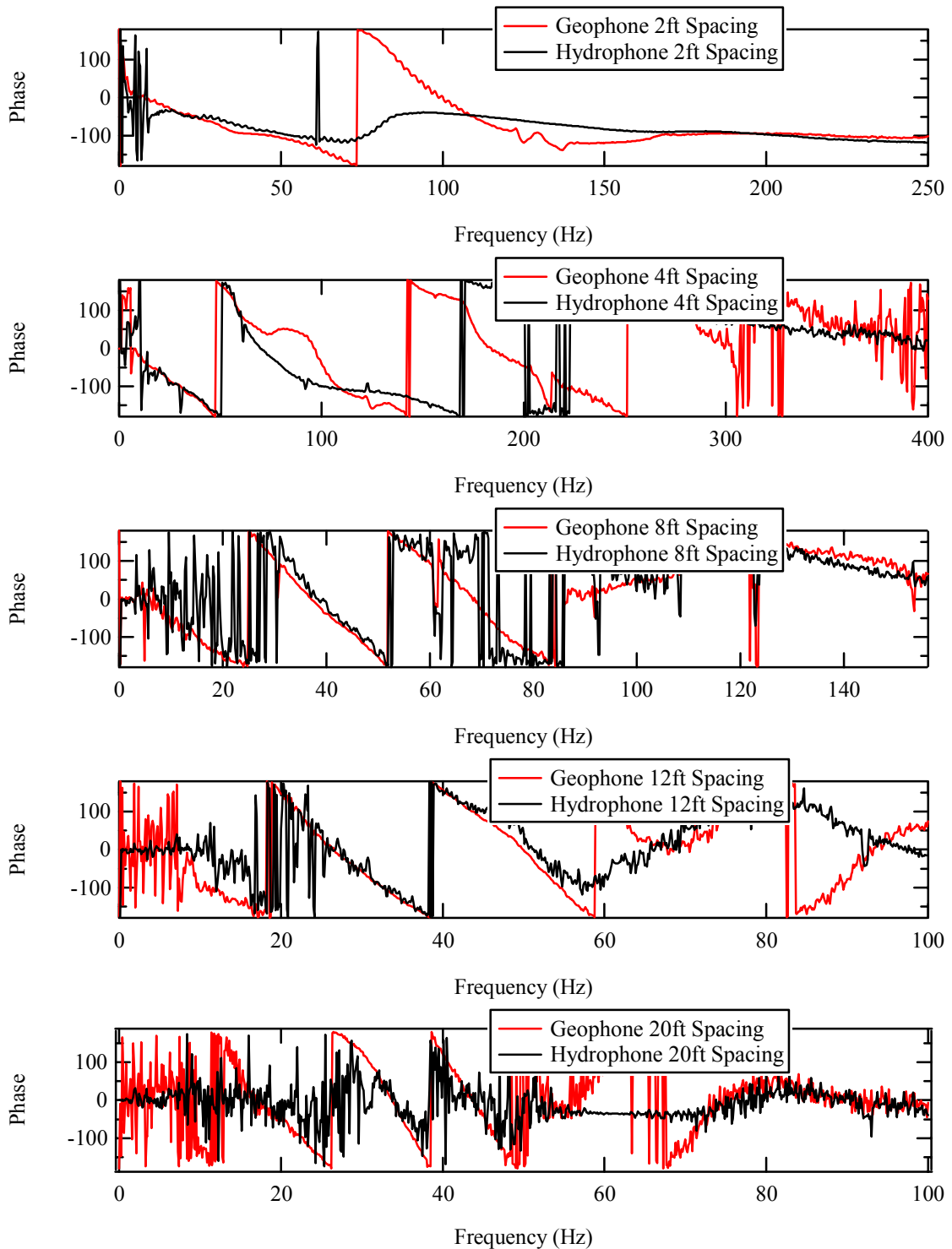


**Figure 5.9** Frequency response comparison between surface wave measurements collected with the geophones and hydrophones.

The phase plots shown in Figure 5.9 were generated from unfiltered data. There are many possible processing methods that could be used to better extract the surface wave velocity. One method used was applying a time domain cosine-taper window to the impulse response function calculated between receiver pairs to isolate the surface wave energy. For the data at the 8 and 12 ft spacings this improved the phase plots considerably. Figure 5.10 shows a comparison of the dispersion curves generated from the geophone data and the filtered hydrophone data for the 12 ft receiver pair.

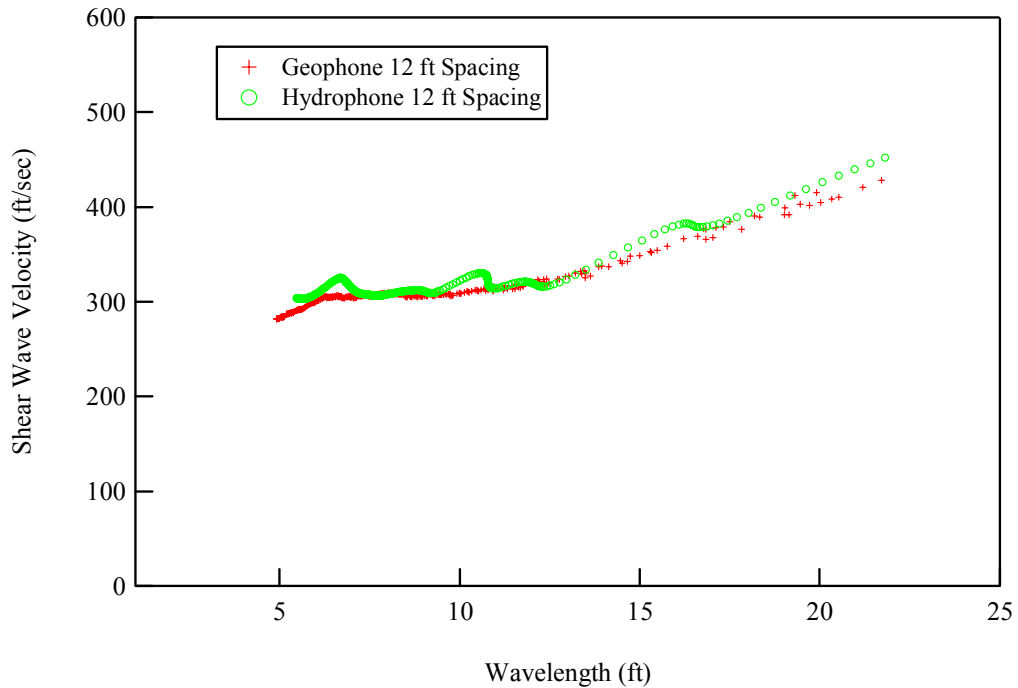


**Figure 5.10** Dispersion curve comparing the geophone and hydrophone at a 12 ft spacing.

#### 5.4.4 Multi-channel Processed Data

The offset time records collected with the suspended hydrophones shown in Figure 5.11 were used to perform a multi-channel analysis, as was done with the geophone data. Due to the high levels of noise in the records, time domain windows

were applied to the recorded time records to take out much of the recorded noise before the transform was applied. The cosine taper window that was used is shown in Figure 5.11. The frequency-wave number ( $f$ - $k$ ) map calculated from the non-contacting hydrophones records is shown in Figure 5.12.

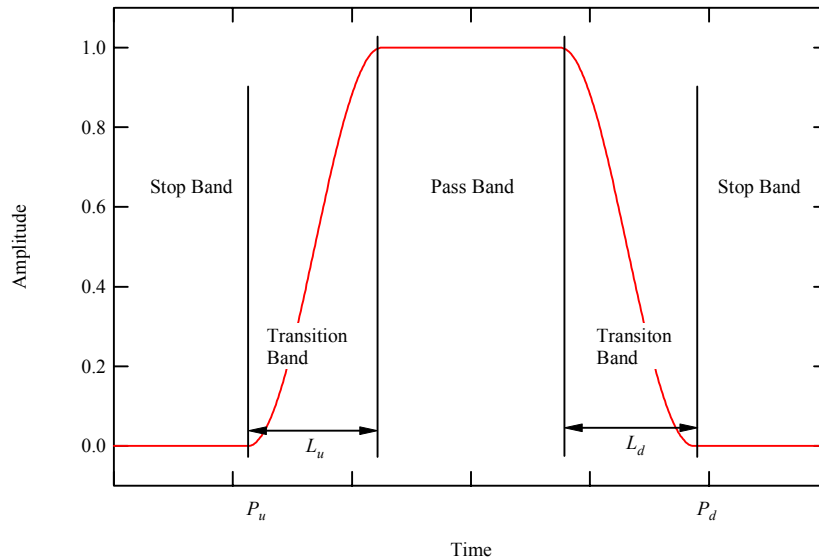


**Figure 5.11** Example of cosine taper window applied to the hydrophone time records.

When compared with the  $f$ - $k$  plot developed from the geophone data, shown in Figure 5.5, it is observed that the same Scholte wave propagation modes can be observed from the non-contacting measurements. Figure 5.13 compares the model dispersion curves generated from both the contacting and non-contacting measurements. The range of frequencies interpreted from the hydrophone data is substantially lower than recorded from the geophone data. Improved measurements of the high-frequency velocities using the multichannel approach requires either a higher energy source to propagate the high frequencies farther or closer spaced receiver array near the source.

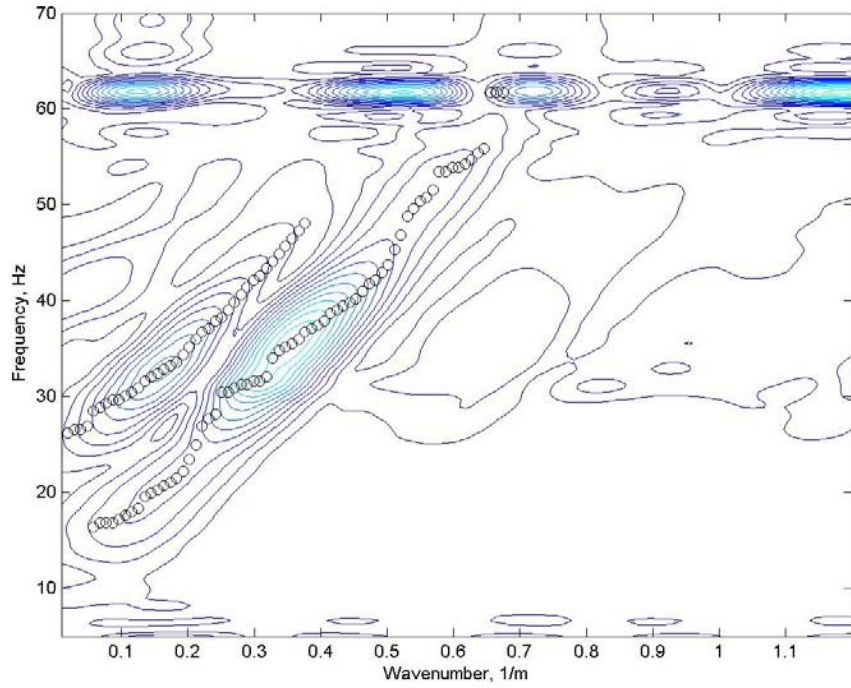


**Figure 5.12** Frequency-wave number map for underwater data collected with the solenoid source and non-contacting hydrophone receivers.

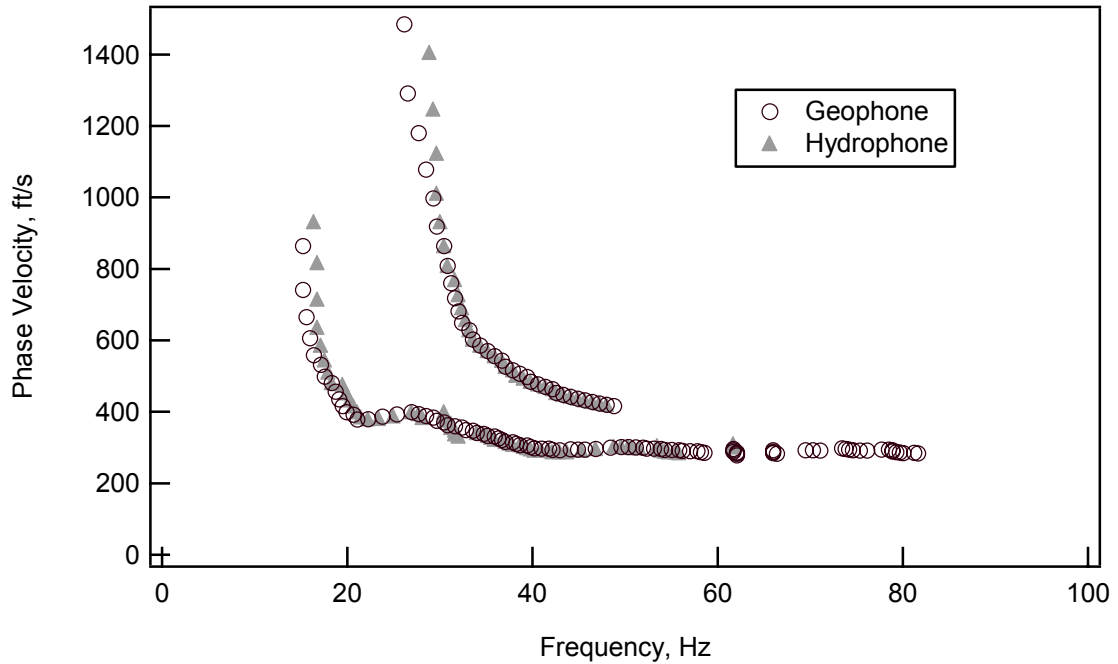


**Figure 5.13** Comparison of dispersion modes calculated from data measured with geophone receivers and data measured with non-contacting hydrophone receivers.

## 5.5 Summary

Underwater testing at the Bradford Farms Research Facility provided valuable information as to the submerged performance of the source. The source performed well in terms of water tightness and reliability in this shallow water environment. Using the solenoid source, dispersion curves were generated from the SASW methodology with usable wavelengths from approximately 1.5 ft to 35 ft long. Data collection in this wavelength range should be sufficient to meet the goal of determining shear wave velocity profiles to depths to 15 to 20 ft with good resolution in the top 1 ft. The data was also successfully processed using a waveform transformation approach. Multiple wave propagation modes were identified from this analysis. The frequency range of interpretation, however, was limited compared to the SASW method.

Data was also collected using non-contacting hydrophone receivers. These measurements clearly showed the arrival of the Scholte wave energy. Conventional data processing methods were employed in analyzing the data. SASW processing of unfiltered data showed very limited usefulness for determining a phase velocity dispersion curve. However, when the data were filtered it was possible to produce dispersion data that were consistent with the dispersion curves generated from the geophone array. Likewise, processing of windowed multi-channel data produced the same propagation modes as were measured with the contacting geophone array. Future work will focus on applying data processing methods for extracting the Scholte wave velocities from the non-contacting hydrophone data. This preliminary study is the first step towards development of a non-contacting underwater system for shear wave velocity profiling underwater.

## CHAPTER 6. SUMMARY, CONCLUSIONS, AND RECOMMENDATIONS

### 6.1 Summary

This thesis presented the design, development and field testing of a system for interface wave measurements to determine shallow  $V_S$  profiles in an underwater environment. The focus of this work was the development of a device capable of measuring  $V_S$  profiles in the top 15 ft to 20 ft with resolution in the top 1 ft of sediment. An underwater source was designed and constructed with the goal of exciting energy with similar amplitude and frequency content as a conventional hammer source used on land.

The impact source that was developed consisted of an impact mass accelerated with a long-stroke electromagnetic solenoid. The source was enclosed in a water-tight and pressure resistant housing. The solenoid was driven using a capacitor bank located in the housing that was charged from a battery at the surface. The source was designed to be remotely triggered from the surface. The source was tested at a terrestrial site and compared to a low-velocity impact of a conventional sledge hammer source. Based on the results from the terrestrial testing, modifications and improvements were made to the source to optimize the performance of the source.

The second phase of the field testing involved underwater testing of the remote source in a shallow, soft bottom lake. Data was collected using both contacting geophone receivers and non-contacting hydrophone receivers suspended in the water column near the sediment.

## 6.2 Conclusions

Results from the field testing program showed that the underwater remote source developed for near-surface  $V_S$  profiling met the design requirements. Although the energy levels excited were slightly lower than the lightly impacted sledge hammer source, the frequency content generated from both sources were comparable and provided a sufficient range in wavelengths for generated  $V_S$  profiles in the top 15 ft to 20 ft of soft underwater sediments while still providing good resolution in the top 1 ft.

The on-land testing revealed improvements to the source to provide a cleaner impact signal. Modifications were made and later tests confirmed the effectiveness of the modifications. Dispersion curves developed using the SASW method and multi-channel analysis were consistent with dispersion data generated using the sledge hammer source.

Results from the underwater tests demonstrated the effectiveness of the underwater source and contacting geophone receivers for making interface wave measurements underwater. Both SASW and multi-channel processing were effectively used to develop dispersion data for the underwater site. Preliminary tests using hydrophone receivers demonstrated the ability to measure the Scholte wave in a non-contacting fashion. Conventional SASW data processing general proved ineffective in extracting dispersion data from hydrophone records. Multi-channel analysis identified the same modes as were found with the contacting receivers although over a limited frequency range.

### **6.3 Recommendations**

The underwater testing source was developed with the intention of future use in feasibility studies associated with non-contacting measurements. The source performed favorably mechanically and electronically in these initial tests, however, improvements to the mechanical systems are needed to improve energy losses identified in the 50 Hz range. In addition, increasing the amplitude at the receivers is important for improved underwater performance, especially at noisy sites. This may be accomplished with mechanical or electrical changes to the solenoid source.

Deep water testing needs to be performed with the solenoid source to evaluate the water and pressure resistance of the containment cell. Effective deployment means of the source and receiver assembly in deep water conditions also needs to be investigated.

Lastly, the results from the non-contacting measurements were limited and preliminary. Based on this brief study with hydrophone receivers, the potential for non-contacting underwater measurements appears promising. Future work will focus on the study of effective data processing methods for extracting interface wave dispersion curves from non-contacting measurements. Also, differences in amplitude and frequency content detected with the hydrophones in shallow and deep water conditions needs to be investigated. Further work with respect to the development of non-contacting sources in conjunction with non-contacting receivers needs to be done to evaluate the feasibility of a non-contacting, “on-the-fly” testing system.

## **APPENDIX A**

### **ASSEMBLY AND OPERATION MANUAL**

# Assembly and Operation Manual For Underwater Surface Wave Testing Source

## Table of Contents

1. General
2. Assembly Instructions
3. Operation Instructions
4. Trouble Shooting

### 1. General

The surface wave testing source is a remote fired electronically controlled source. The source is vertically oriented and is capable of generating surface waves up to 20 feet in length. Several aspects of its assembly and operation are discussed herein.

A general overview and description of components can be found in Figure 1.1. The part numbers and names listed in Table 1.1 will be used throughout to simplify descriptions. The sub-assemblies shown in Figure 1.1 will be exploded and explained in more detail in Section 2.

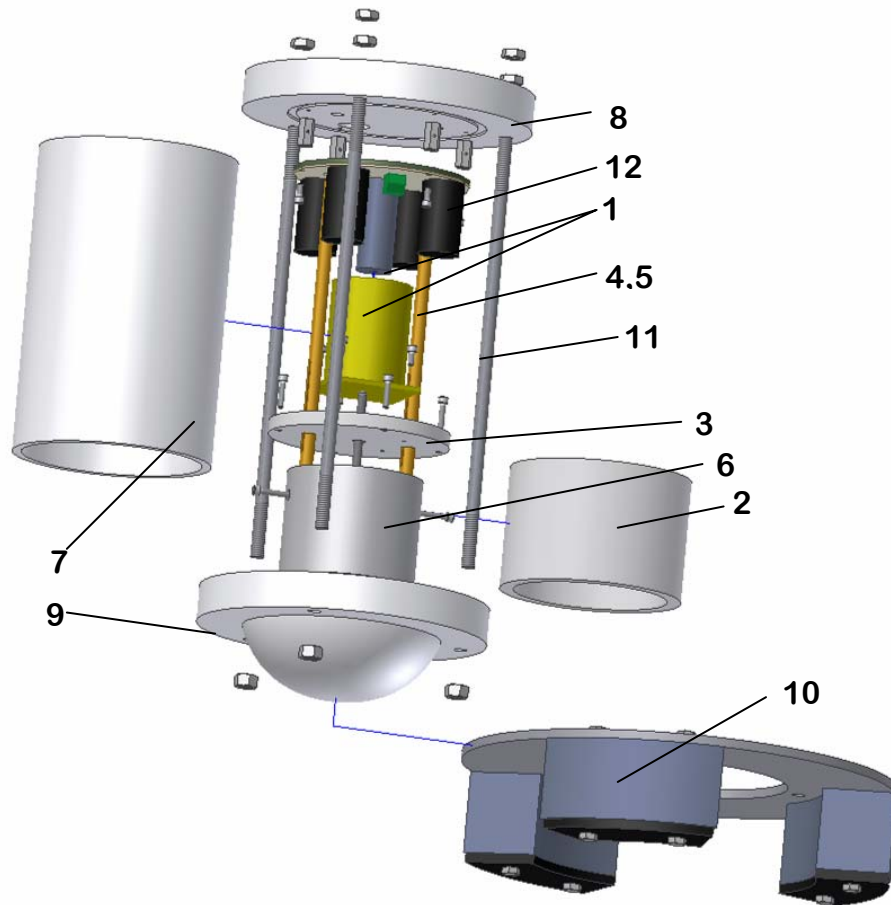


Figure 1.1. Exploded View of Surface Wave Source

**Table 1.1. Component Part Names**

Part Number	Name
1	Solenoid (and Plunger)
2	Sleeve
3	Mounting Plate
4	Guide Rod
5	Return Spring
6	Moving Mass
7	Cell Wall
8	Top Cap
9	Bottom Cap
10	Reaction Mass Sub-Assembly
11	Clamp Rods

**2. Assembly Instructions:**

A parts list including all hardware and fasteners for the Surface Wave Source is shown in Table 2.1. The part numbers listed in Table 2.1 will be used in the assembly instructions section to explain part interaction. All parts listed in Table 2.1 are necessary for complete assembly.

**Table 2.1. Complete Parts List**

Part Number	Description	Quantity
1	Solenoid	1
2	Plunger	1
3	Plunger Connecting Rod	1
4	Sleeve	1
5	Mounting Plate	1
6	Guide Rod	2
7	2 1/4" Extension Spring	2
8	Moving Mass	1
9	Cell Wall	1
10	Top Cap	1
11	Bottom Cap	1
12	Clamp Rod	3
13	Power Circuit Sub-Assembly	1
14	3/4" #8-32 Socket Head Cap Screw	4
15	1/2" #8-32 Socket Head Cap Screw	4
16	1" #8-32 Socket Head Cap Screw	2
17	4" Compression Spring	3
18	1/8" Roll Pin	2
19	1/2" #8-32 Coupling Nut	4
20	1/2" #8-32 Threaded Stud	4
21	3/8" #8-32 Socket Head Cap Screw	4
22	3/8" #4-40 Stainless Socket Head Cap Screw	4
23	3" 1/4"-20 Stainless Steel Bolt	6
24	1/4"-20 Stainless Nylon Lock Nut	6
25	Lead Weight	3
26	Reaction Mass Mounting Plate	1
27	Reaction Mass Washers	3
28	#3/8-16 Stainless Jam Nut	6
29	3/8"-16 Stainless Nylon Lock Nut	3
30	Rubber O-Ring	2

Assembly procedure:

1. Ensure that all of the parts listed in Table XX are present.
2. Install a 1/8" Roll Pin (part #18) into the hole in the top of the Guide Rod (part #6) and through the loop on one end of the 2.25" Extension Spring (part #7). The pin can be pushed through the hole with a pair of pliers bearing on the Guide Rod. Repeat this step for the other

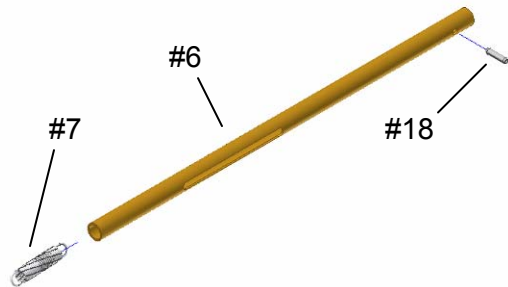


**Fig 2-1**

*Guide Rod and Extension Spring. Fig 2-1*

3. Slide the *Guide Rod* (part #6) through the *Mounting Plate* (part #5) using the hole indicated in **Fig 3-1**. Then slide the *Guide Rod* through hole in the *Moving Mass* (part #8) indicated in **Fig 3-1**. The *Guide Rods* need to be oriented so that slot is perpendicular with the hole on the outside of the *Moving Mass*, see **Fig 3-2**.

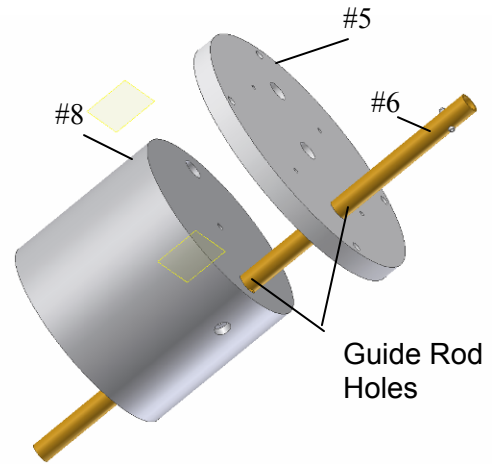


**Fig 3-1**

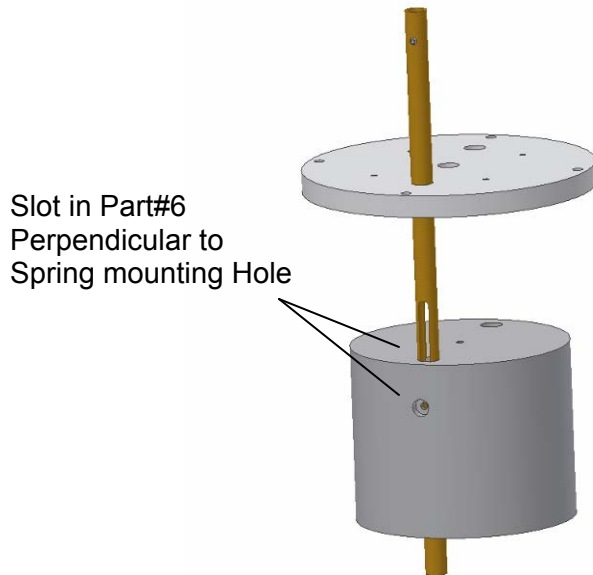


**Fig 3-2**

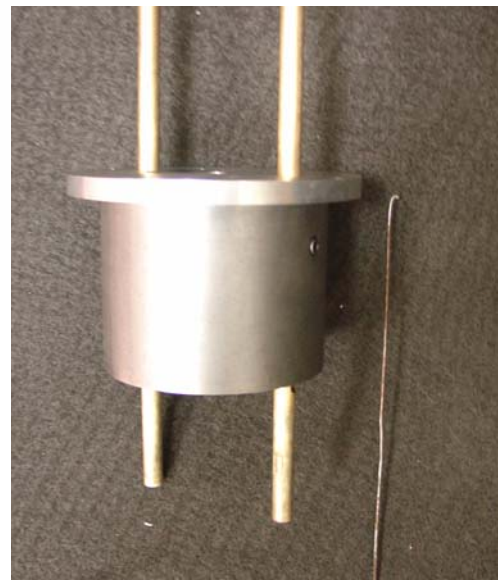


**Fig 4-1**

4. With the *Moving Mass* (part #8) stabilized, use a thin wire with a hook on the end as seen in **Fig 4-1** to “fish” the bottom loop on the *Extension Spring* in line with the screw hole on the side of the *Moving Mass*, see **Fig 4-2**. Once the loop is aligned with the hole insert the 1” #8-32 *Hex Cap Screw* (part #16). Repeat for the other guide rod assembled in Step 1.

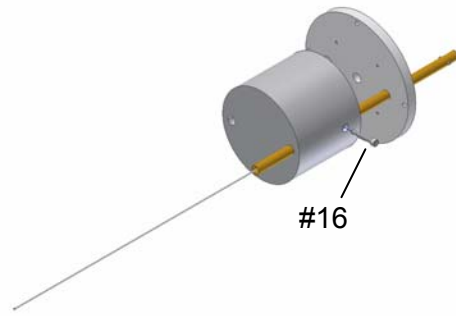


**Fig 4-2**

5. Slide the *Sleeve* (part #4) over the *Moving Mass* (part #8) and attached using the (4) 3/4” #8-32 *Socket Head Cap Screws* (part #14), see **Fig 5-1**.

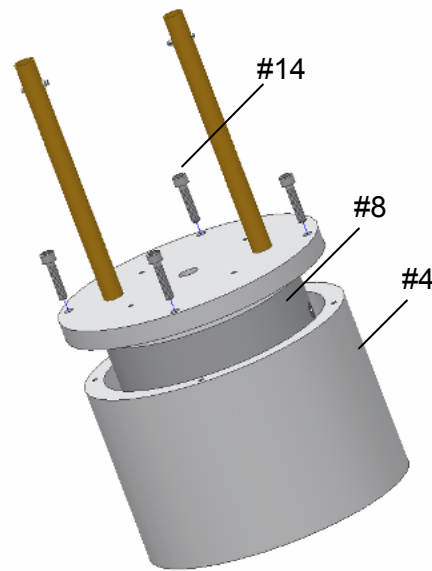


**Fig 5-1**

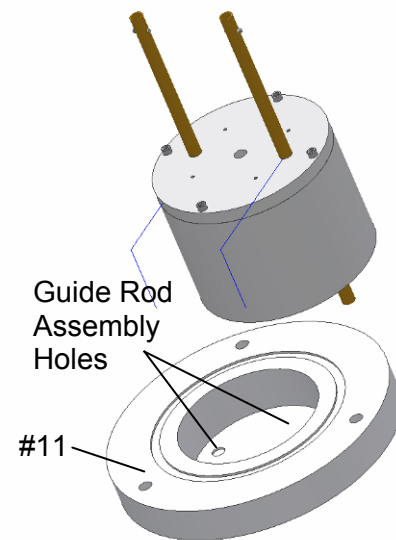


**Fig 6-1**

6. Install the assembly in the *Bottom Cap* (part #11) so that the *Guide Rods* (part #6) fall into the assembly holes indicated in **Fig 6-1**.
7. Connect the *Solenoid* (part #1) to the *Mounting Plate* (part #5) using the (4) *3/8" Socket Head Cap Screws* (part #15). Make sure the *Solenoid* base is not pressing on either guide rod. **Fig 7-1**

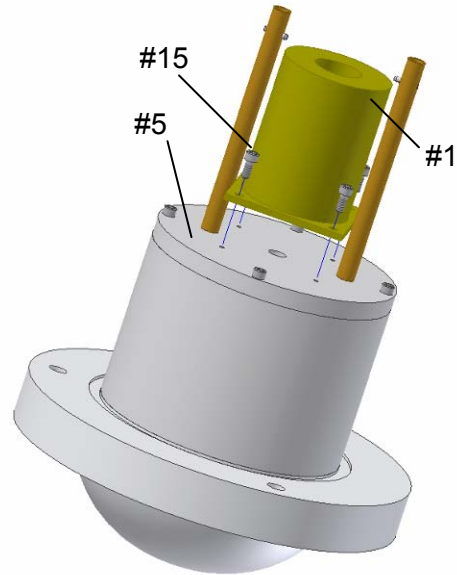


**Fig 7-1**

8. Screw the *Plunger Connecting Rod* (part #3) into the *Plunger* (part #2) until snug.
9. Connect the *Plunger Connecting Rod* (part #3) to the *Moving Mass* (part #8) through the hole in the *Solenoid* base. Measure the distance between the top of the *Solenoid* and the top of the *Plunger* and adjust to 1.5". This is the stroke of the system and can be adjusted if needed. **Fig 9-1**.

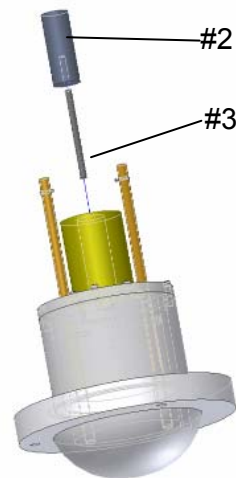


**Fig 9-1**

10. Clean and grease the *Rubber O-ring* (part #30) using vacuum grease. Ensure the O-ring is seated in the O-ring groove in the *Bottom Cap* (part #11) and

apply additional vacuum grease to the top of the O-ring.

11. Clean and inspect the end of the *Cell Wall* (part #9). The ends of the *Cell Wall* should be smooth and free of dings or dents. If this is not the case the cell has the potential to leak.
12. Insert the *Cell Wall* (part #9) into the seating groove on the *Bottom Cap* (part #11) as shown in **Fig 12-1**.

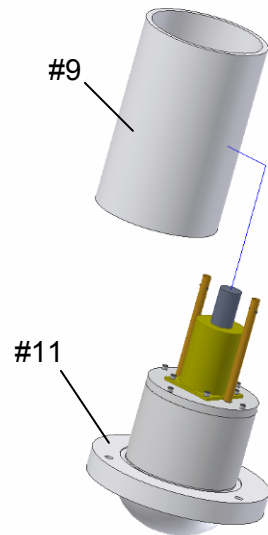


**Fig 12-1**

13. If not already assembled, the *Power Circuit Sub-Assembly* (part #13) needs to be attached to the *Top Cap* (part #10). This can be done by installing the (4) 1/2" #8-32 *Threaded Studs* (part #20) into holes on the underside of the *Top Cap*. Once the *Threaded Studs* are installed, the (4) 1/2" #8-32 *Coupling Nuts* (part #19) can be installed on the *Threaded Studs*. The *Power Circuit Sub-Assembly* is then attached to the *Coupling Nuts* by (4) 3/8" #8-32 *Socket Head Cap Screws* (part #21). **Fig 13-1** (NOTE: The *Power Circuit Sub-Assembly* cannot be separated from the *Top Cap* without disconnecting soldered connections either at the *Sub-Assembly* or the waterproof electrical connection. The *Sub-Assembly* can be loosened for observation or maintenance using the inverse of step #13)

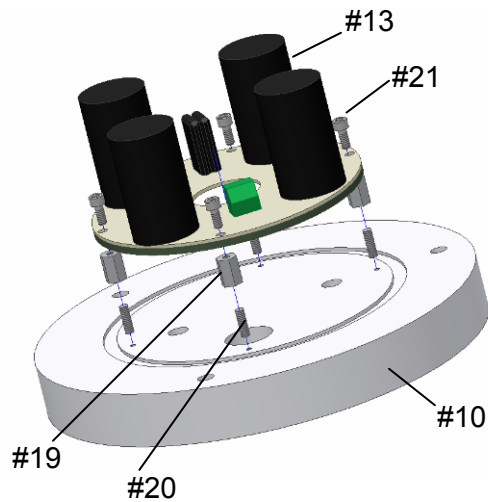


**Fig 13-1**

14. Insert the (3) *Clamp Rods* (part #12), with the (3) *3/8"-16 Nylon Lock Nuts* (part #29) already attached, through the clamp rod holes in the *Bottom Cap* (part #11). **Fig 14-1**

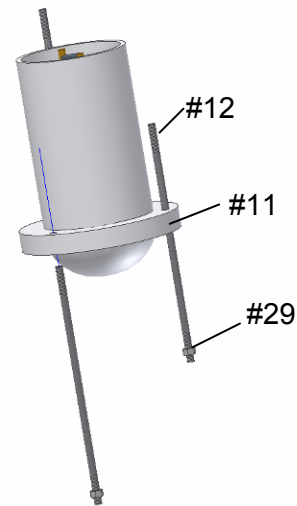


**Fig 14-1**

15. The (3) *4" Compression Springs* (part #17) can be installed over the *Clamp Rods* (part #12) and allowed to rest on the *Bottom Cap* (part #11). **Fig 15-1**

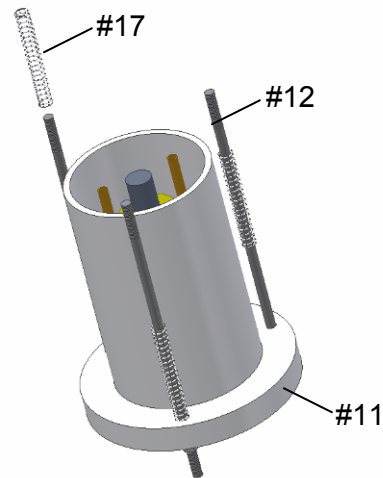


**Fig 15-1**

16. The *Reaction Mass Sub-Assembly*:  
(Note: If the *Reaction Mass Sub-Assembly* is already assembled skip to step #17). Using the *3" 1/4"-20 Stainless Steel Bolt* (part #24) and *1/4"-20 Stainless Steel Nylon Lock Nut* (part #24) attach the *Reaction Mass Washer* (part #27) and *Lead Weight* (part #25) to the *Reaction Mass Mounting Plate* (part #26) as shown in **Fig 16-1**

17. Install the *Reaction Mass Mounting Plate* (part #26) on the *Clamp Rods* (part #12) on top of the *Compression Springs* (part #17) **Fig 17-1**

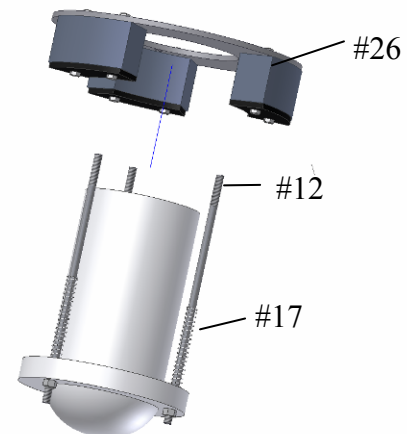


**Fig 17-1**

18. Clean and grease the *Rubber O-ring* (part #30) using vacuum grease. Ensure the O-ring is seated in the O-ring groove in the *Top Cap* (part #10) and apply additional vacuum grease to the top of the o-ring.

19. Clean and inspect the end of the *Cell Wall* (part #9). The ends of the *Cell Wall* should be smooth and free of dings and dents. If this is not the case the cell has the potential to leak.
20. Connect the wire leads from the *Solenoid* (part #1) to the green screw terminal block on the *Power Circuit Sub-Assembly* (part #13). (NOTE: Polarity of the connection does not matter.)
21. Install the *Top Cap* (part #10) so that the clamp rod holes align with those in the *Bottom Cap* (part #11). Holes in the *Power Circuit Sub-Assembly* (part #13) must be aligned with the *Guide Rods* (part #6) before the *Top Cap* will rest firmly on the *Cell Wall* (part #9). Ensure the *Top Cap* is firmly seated on the *Cell Wall*. **Fig 20-1**

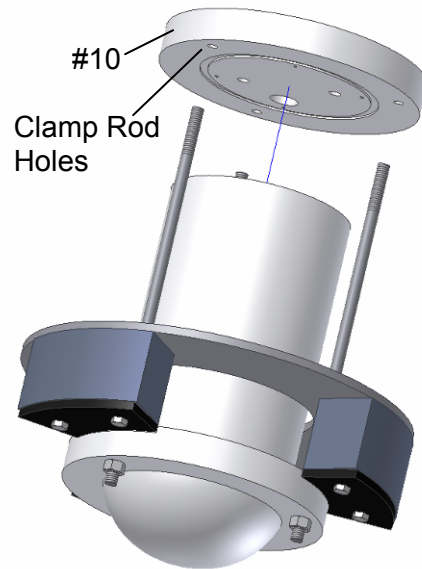


**Fig 20-1**

22. With the *Top Cap* (part #10) seated on the *Cell Wall* (part #9), push the *Clamp Rods* (part #12) through the clamp rod holes in the *Top Cap* and install the (3)  $3/8''$ -16 *Stainless Jam Nuts* (part #28). Once the first 3 nuts are installed check to ensure the *Cell Wall* (part #9) is seated in both caps and install the remaining (3)  $3/8''$ -16 *Stainless Jam Nuts* (part #28). **Fig 21-1**

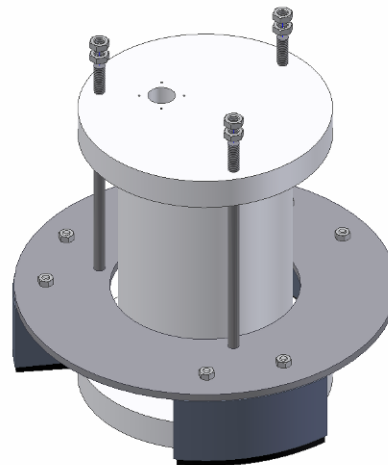


**Fig 21-1**

### 3. Operation Instructions:

The surface wave testing source is simple to operate. Components needed for operation include the assembled *Surface Wave Source*, the *Wire*, and the *Power/Control Box*.

Connecting the *Wire*:

The *Wire* can be connected to the *Source* at the Ampenol waterproof plug located on the *Top Cap*. The plug connects with a pushing while threading motion. Push the plug together and tread until tight. Not tightening the plug completely could result in a leak at the connection. The *Wire* is connected to the *Power/Control Box* under the cover plate.

*Power/Control Box*:

The *Power/Control Box* contains (2) 12 volt lawn tractor batteries wired in series. The batteries need to be checked and charged occasionally. The operation of the system occurs at the control box.

To charge the capacitors and prepare the *Source* for energizing, the rocker switch on the top of the *Power/Control Box* labeled ON/OFF must be turned to **ON**. The indicator light should illuminate at this time. If this does not occur see the **Troubleshooting** section. The light indicates the charging circuit is complete through the fuse and the capacitors should be charging.

*Triggering the Source*:

The *Source* can be remotely energized by either manually pressing the red button or using an electronic output of 10 volts at the BNC connector. The BNC output needs to be a discrete step function with a maximum of 10 volts DC. The time frame associated with the step is not critical as the *Source* will behave similarly at any time interval. When energizing the source in the laboratory, a second much smaller impact should be heard after the large firing impact. This second impact is a result of the *Extension Springs* reloading the source for the next energizing. If this second impact is not heard, consult the **Troubleshooting** section.

### 4. Troubleshooting

Troubleshooting the *Source* is sometimes necessary. Table 4.1 shows some potential problems and solutions. The electrical system is also discussed in greater detail.

The control circuit operates on 10 volts. The resistor and diode at the beginning of the control section of the circuit shown in Figure 4.1 ensure this. The control circuit should have no current flowing through it unless the manual switch or BNC are engaged. The control circuit can be tested by testing using a multi-tester at the plug location on the *Power/Control Box*. If the multi-tester leads are placed between the control and common female plug connections and the circuit is energized the multi-tester should read approximately 10 volts (typically 9.8 volts). If the control circuit is not triggered, there should be no voltage difference at this point.

The charging circuit should show a voltage difference at the Power/Control Box connection of 24 volts at any time if the master switch is engaged.

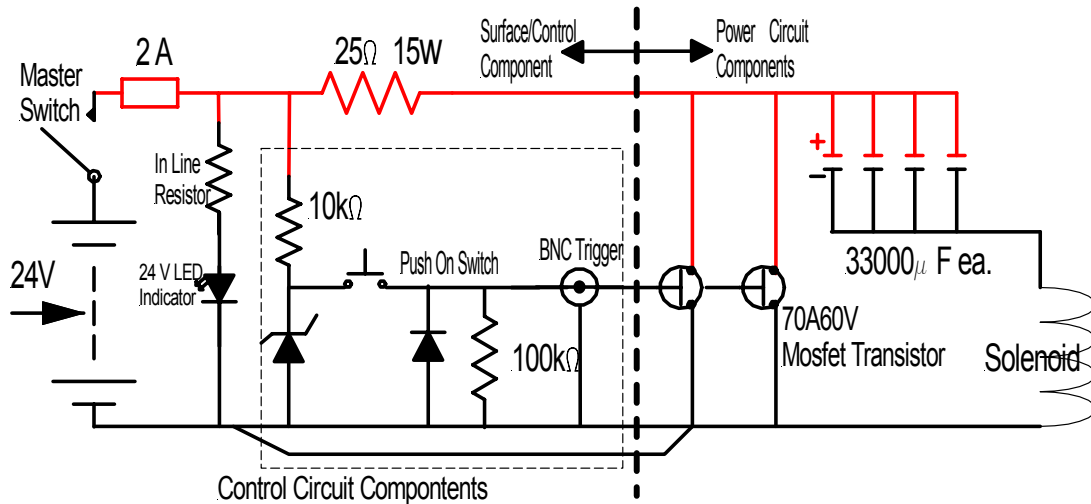


**Figure 4.1. Circuit Diagram**

If the control circuit and charging circuit both appear to be working at the Power/Control Box connection, the wire must be checked for continuity. This can be done using the plug wiring diagram in Figure 4.2.

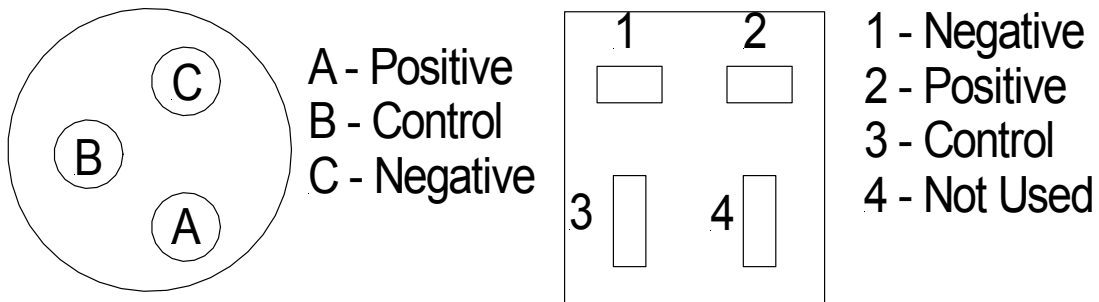


**Figure 4.2. Plug Wiring Diagram**

If no problem has been located to this point, check all connections in the Power Circuit Sub-Assembly. If energized (wire connected and master switch ON). The capacitors should be holding a voltage of approximately 24 volts. The transistors and control circuit can be checked by placing a multi-tester on the 2 poles of the screw terminal block and energizing. The peak voltage should be approximately 24 volts when triggered.

**Table 4.1. Troubleshooting**

<i>Problem</i>	<i>Cause</i>	<i>Solution</i>
Source Leaking	<ul style="list-style-type: none"> <li>• Displaced O-Ring</li> <li>• Faulty O-Ring</li> <li>• Plug Leak</li> </ul>	<ul style="list-style-type: none"> <li>• Disassemble cell to a point where o-rings can be inspected, if o-ring is out of o-ring groove, replace, apply vacuum grease and reassemble.</li> <li>• Inspect o-ring for splits, cracks, or breaks. If any of these are the case replace o-ring.</li> <li>• Remove the 4 socket cap screws holding the waterproof plug. Ensure the o-ring located in the plug hole is intact. Relubricate and replace as necessary. The plug is sealed and will not leak through the connection pins. If it is leaking, the leak is the plug o-ring.</li> </ul>
Source Not Energizing	<ul style="list-style-type: none"> <li>• Reloading Malfunction</li> <li>• Charging Time</li> <li>• Electrical Malfunction</li> </ul>	<ul style="list-style-type: none"> <li>• Shake source until the reloading sound is heard. If underwater, shake gently with electrical wire and attempt to energize.</li> <li>• Wait for 1 minute and attempt to fire again. The capacitor bank should charge completely in 20-30 seconds.</li> <li>• Check all visible electrical connections at the Power/Control Box. If no connections are loose, continue checking connections throughout the power circuit. If the power circuit appears intact, move to the control circuit. Circuit diagrams can be found in Figure 4.1.</li> </ul>
Weak Impact	<ul style="list-style-type: none"> <li>• Indicator Light is OFF</li> <li>• Charging Time</li> <li>• Reloading Malfunction</li> <li>• Clamp Slippage</li> </ul>	<ul style="list-style-type: none"> <li>• Remove the fuse by turning the fuse cap 1/2 turn. The fuse should be intact. If it is not, replace with a AGC 2A fuse, available at a local hardware store.</li> <li>• Wait for 1 minute and attempt to fire again. The capacitor bank should charge completely in 20-30 seconds. If the capacitor bank is not completely charged, the impact strength will be affected.</li> <li>• Shake source until the reloading sound is heard. If underwater, shake gently with electrical wire and attempt to energize. If the source has partially reloaded the impact is affected.</li> <li>• Disassemble cell to a point where Shaft Clamps can be inspected and insure that they are both contacting the Mounting Plate so that the top of the Guide Rod is 5" from the top of the Mounting Plate. If this is not the case, loosen clamps, adjust until 5" spacing is achieved and tighten clamps.</li> </ul>

## References

- Achenbach, J.D., (1973), *Wave Propagation in Elastic Solids*, North Holland Publishing Company
- ASTM (1991), "Standard Test Methods for Crosshole Seismic Testing." ASTM Designation: D4428/D 4428M-91, July.
- Campanella, R.G., and P.K. Robertson, (1984), "A Seismic Cone Penetrometer to Measure Engineering Properties of Soil," *Proceedings of the Fifty-Fourth Annual Meeting of the Society of Exploration Geophysicists*, Atlanta, Georgia
- Bedford, A., and Crumheller, D.S., (1994), *Introduction to Elastic Wave Propagation*, J. Wiley and Sons Ltd, Chichester, England
- Hardin, B.O., (1978), "The Nature of Stress-Strain behaviour for soils. State-of-the-art Report," *Proceedings of the Specialty Conference on Earthquake Engineering and Soil Dynamics*, Pasadena, June, ASCE, pp. 3-90
- Haskell, N.A., (1953), "The Distribution of Surface Waves on Multilayered Media," *Bulletin of the Seismological Society of America*, Vol. 43, pp. 17-34
- Kaufmann, R.D., Xia, J., Benson, R.C., Yuhr, L.B., Castro, D.W., and C.B. Park, (2005) "Evaluation of MASW Data Acquired with a Hydrophone Streamer in a Shallow Marine Environment," *Journal of Environmental and Engineering Geophysics*, Vol. 10, Issue 2, June, pp. 87-98
- Kausel, E., and Peek, R., (1982), "Dynamic Loads in the Interior of a Layered Stratum: An Explicit Solution," *Bulletin of the Seismological Society of America*, Vol. 72 pp. 1459-1481
- Kausel, E., and Roesset, J., (1981), "Stiffness Matrices for Layered Soils," *Bulletin of the Seismological Society of America*, Vol. 70, pp. 1743-1761
- Kearey, P., M. Brooks, I. Hill, (2002) *An Introduction to Geophysical Exploration*, Blackwell Science, Williston, Vermont, 262 pp.
- Kitsunezaki, C. (1980), "A new Method for Shear Wave Logging," *Geophysics*, Vol. 45, pp.1489-1506
- Lee, Byung-Sik, (1996), *Analytical Studies of Surface Wave Propagation Along the Seafloor for Application to Spectral-Analysis-of-Surface-Waves (SASW) Testing*, Ph.D. Dissertation, the University of Texas at Austin, 333 pp.

- Luke, B.A., K.H. Stokoe, S.G. Wright, J.M. Roesset, and B. Lee, (1994) "Experimental Investigation of Surface Wave Velocities in Simulated Ocean Bottoms," *Proceedings of the 25<sup>th</sup> Offshore Technology Conference*, OTC Paper 7112, Houston, May.
- McMechan, G.A., and Yedlin, M.J., (1981), "Analysis of Dispersive Waves by Wave Field Transformation," *Geophysics*, Vol. 46, pp. 869-874
- Miller, G.F., and H. Pursey (1955), "On the Partition of Energy Between Elastic Waves in a Semi-Infinite Solid," *Proceedings Royal Society, London, A*, v.233, pp.55-69
- Nigbor, R. L., and T. Imai (1994), "The suspension P-S velocity logging method, in geophysical Characterization of Sites," *Technical committee for XIII ICSMFE*, A. A. Balkema, Rotterdam, The Netherlands, 57-61
- Park, C.B., R.D. Miller, Xia, J. (1999) "Multichannel Analysis of Surface Waves," *Geophysics*, Vol 64, No. 3, May-June, pp. 800-808
- Park, C.B., Miller, R.D., Xia, J., Ivanov, J., Hunter, J.A., Good, R.L. and R.A. Burns, (2000) "Multi-channel Analysis of Underwater Surface Waves Near Vancouver B.C., Canada, Technical Program with Biographies", SEG, 70<sup>th</sup> Annual Meeting, Calgary, Canada, pp. 1303-1306
- Richart, J.E., Jr., (1962), "Foundation Vibrations", *Transcripts ASCE*, Vol. 127, Part 1, pp. 863-898
- Richart, J.E., Jr., J.R.Hall Jr., and R.O. Woods, (1970), *Vibrations in Soils and Foundations*, Englewood Cliffs, New Jersey Prentice-Hall Inc.
- Rosenblad, B.L, (2000) *Experimental and Theoretical Studies in Support of Implementing the Spectral-Analysis-of-Surface-Waves (SASW) Method Offshore*, Ph.D. Dissertation, the University of Texas at Austin, 298 p.
- Roesset, J.M., Kausel, E., Cuellar, V., Monte, J.L. and Valerio, J. (1994). "Impact of Weight Falling onto the Ground," *Journal of Geotechnical Engineering*, Vol. 120, No. 8, August, pp. 1394-1412.
- Sanchez-Salinerio, I. (1987), *Analytical Investigation of Seismic Methods Used for Engineering Applications*, Ph.D. Dissertation, The University of Texas at Austin, 401 pp.
- Sedighi Manesh, M. (1991), *Theoretical Investigation of the Spectral-Analysis-of-Surface-Waves (SASW) Technique for Application Offshore*, Ph.D. Dissertation, the University of Texas at Austin, 186 pp.

- Sharma, P.V., (1997) *Environmental and Engineering Geophysics*, Cambridge, England, Cambridge University Press, 475 pp.
- Stokoe, K.H., J. Lee, and S. Lee, (1991) "Characterization of Soil in Calibration Chambers with Seismic Waves," *Proceedings of the 1<sup>st</sup> International Symposium on Calibration Chamber Testing*, June.
- Stokoe, K.H., S.W. Wright, J.A. Bay, and J.M. Roesset, (1994), "Characterization of Geotechnical Sites by SASW Method," *Geophysical Characteristics of Sites*, ISSMFE Technical Committee #10 for XII ICMFE, A.A. Balkema Publishers, Rotterdam & Brookfield, Netherlands pp.785-816
- Stokoe, K.H. M.B. Darendeli, R.D. Andrus, L.T. Brown, (1999), "Dynamic Soil Properties: Laboratory, Field and Correlation Studies," *Proceedings of the 2<sup>nd</sup> International Conference on Earthquake Geotechnical Engineering*, P. Secoe Pito editor, Vol. 3, Lisbon, Portugal, June, pp.811-845
- Stokoe, K.H. II, Rathje, E.M., Wilson, C.R. and Rosenblad, B.L. (2004), "Development of Large-Scale Mobile Shakers and Associated Instrumentation for In Situ Evaluation of Nonlinear Characteristics and Liquefaction Resistance of Soils," *13<sup>th</sup> World Conference on Earthquake Engineering*, August 1-6
- Thompson, W.T., (1950), "Transmission of Elastic Waves through a Stratified Solid Medium," *Journal of Applied Physics*, Vol. 21, pp. 89-93
- Woods, R.D. (1968), "Screening of Surface Waves in Soils," *Journal of Soil Mechanics and Foundations Division*, Proc. ASCE, Vol. 94, No. SM 4, July, pp.951-979